

3-21-2018

Novel Strongly Coupled Magnetic Resonant Systems

Daerhan Liu

Florida International University, ddaer001@fiu.edu

DOI: 10.25148/etd.FIDC004083

Follow this and additional works at: <https://digitalcommons.fiu.edu/etd>

 Part of the [Electrical and Electronics Commons](#), [Electromagnetics and Photonics Commons](#), and the [Power and Energy Commons](#)

Recommended Citation

Liu, Daerhan, "Novel Strongly Coupled Magnetic Resonant Systems" (2018). *FIU Electronic Theses and Dissertations*. 3717.
<https://digitalcommons.fiu.edu/etd/3717>

This work is brought to you for free and open access by the University Graduate School at FIU Digital Commons. It has been accepted for inclusion in FIU Electronic Theses and Dissertations by an authorized administrator of FIU Digital Commons. For more information, please contact dcc@fiu.edu.

FLORIDA INTERNATIONAL UNIVERSITY

Miami, Florida

NOVEL STRONGLY COUPLED MAGNETIC RESONANT SYSTEMS

A dissertation submitted in partial fulfillment of

the requirements for the degree of

DOCTOR OF PHILOSOPHY

in

ELECTRICAL ENGINEERING

by

Daerhan Liu

2018

To: Dean John L. Volakis
College of Engineering and Computing

This dissertation, written by Daerhan Liu, and entitled Novel Strongly Coupled Magnetic Resonant Systems, having been approved in respect to style and intellectual content, is referred to you for judgment.

We have read this dissertation and recommend that it be approved.

Jean Andrian

Nezih Pala

Berrin Tansel

Kang Yen

Stavros Georgakopoulos, Major Professor

Date of Defense: March 21, 2018.

The dissertation of Daerhan Liu is approved.

Dean John L. Volakis
College of Engineering and Computing

Andres G. Gil
Vice President for Research and Economic Development
and Dean of the University Graduate School

Florida International University, 2018

© Copyright 2018 by Daerhan Liu

All rights reserved.

DEDICATION

To my parents, wife and son, your unconditional love and support has always been the strength to keep me going forward. This is for you.

ACKNOWLEDGMENTS

I would like to use this opportunity to express my sincerest gratitude towards my major professor, Dr. Stavros Georgakopoulos, for his great guidance and support through my Ph.D. program at FIU. He provided an excellent research environment with the latest simulation software and state of the art testing and manufacturing equipment. He has truly given me the opportunity to expand my knowledge and broaden my horizons for the next chapter of my career. I would also like to thank Dr. Nezhil Pala, Dr. Jean Andrian, Dr. Berrin Tansel, and Dr. Kang Yen for serving on my dissertation defense committee and for their illuminating comments.

I also want to express my gratitude to all the members of FIU Electrical and Computing Engineering Department and special thanks to Dr. Hao Hu, Dr. Shun Yao, Dr. Xueli Liu, Dr. John Gibson, Dr. Yipeng Qu, Kun Bao, Yousuf Shafiq, Dieff Vital, Nicholas Russo, Dimitrios Siafarikas, Xiang Li, and Oscar Silveira for their help and friendship.

ABSTRACT OF THE DISSERTATION
NOVEL STRONGLY COUPLED MAGNETIC RESONANT SYSTEMS

by

Daerhan Liu

Florida International University, 2018

Miami, Florida

Professor Stavros Georgakopoulos, Major Professor

Wireless power transfer (WPT) technologies have become important for our everyday life. The most commonly used near-field WPT method is inductive coupling, which suffers from low efficiency and small range. The Strongly Coupled Magnetic Resonance (SCMR) method was developed recently, and it can be used to wirelessly transfer power with higher efficiency over a longer distance than the inductive coupling method.

This dissertation develops new SCMR systems that have better performance compared to standard SCMR systems. Specifically, two new 3-D SCMR systems are designed to improve the angular misalignment sensitivity of WPT systems. Their power transfer efficiency for different angular misalignment positions are studied and analyzed. Prototypes are built for both systems and their performance is validated through measurement. Furthermore, new planar broadband conformal SCMR (CSCMR) systems are developed that maintain high efficiency while providing significantly larger bandwidth than standard CSCMR systems. Such broadband CSCMR systems are used here for the first time to simultaneously accomplish highly efficient wireless power transfer and high data rate communication through the same wireless link. These systems

that combine wireless power and communication are expected to enable next-generation applications with battery-less and “power-hungry” sensors. Example applications include implantable and wearable sensors as well as embedded sensors for structural health monitoring.

TABLE OF CONTENTS

CHAPTER	PAGE
1. INTRODUCTION.....	1
1.1 Problem Statement.....	1
1.2 Research Objectives and Contributions.....	2
1.3 Methodology.....	3
1.4 Dissertation Outline.....	4
2. BACKGROUND AND RELATED WORK.....	5
2.1 Wireless Power Transmission (WPT) Techniques.....	5
2.2 Strongly Coupled Magnetic Resonance (SCMR).....	6
2.2.1 Basic Principle of SCMR System.....	6
2.2.2 Power Transfer Efficiency of SCMR System.....	9
2.2.2 Misalignment Analysis.....	13
3. MISALIGNMENT SENSITIVITY OF STRONGLY COUPLED WIRELESS POWER TRANSFER SYSTEMS.....	15
3.1 Misalignment Analysis of Standard and Conformal SCMR Systems.....	15
3.1.1 Standard SCMR.....	22
3.1.2 Conformal SCMR (CSCMR).....	25
3.2 Misalignment Analysis of Proposed Misalignment Insensitive SCMR System.....	31
3.2.1 3-D SCMR.....	31
3.2.2 Hybrid SCMR (HSCMR).....	39
3.3 Comparison Discussion.....	44
4. CYLINDRICAL MISALIGNMENT INSENSITIVE WIRELESS POWER TRANSFER SYSTEMS.....	47
4.1 Misalignment Sensitivity Background Study.....	47
4.2 Cylindrical Misalignment Insensitive SCMR system.....	54
4.2.1 Cylindrical SCMR based on Wire Elements.....	54
4.2.2 Cylindrical SCMR with Flexible PCB.....	62
4.2.3 Lateral Misalignment Comparison of CSCMR and Proposed Cylindrical SCMR.....	69
4.3 Wearable Applications for Cylindrical SCMR systems.....	71
4.4 Optimizing Cylindrical SCMR.....	77
5. SIMULTANEOUS POWER AND DATA TRANSFER WITH BROADBAND STRONGLY COUPLED MAGNETIC RESONANT SYSTEM.....	81
5.1 Design of Planar Broadband CSCMR system.....	81
5.2 System Description.....	90
5.2.1 Backscattering modulation.....	91
5.2.2 Data rate.....	92

5.2.3	Power transmitter/data receiver	94
5.2.4	Power Receiver/data transmitter	95
5.3	Simulation and Measurement and Results	96
5.3.1	Comparison between standard and broadband SCMR	97
5.3.2	Power efficiency	99
5.3.3	Data communication	100
6.	CONCLUSION AND FUTURE WORK	102
6.1	Conclusions	102
6.2	Future Work	103
	REFERENCES	105
	VITA	113

LIST OF TABLES

TABLE	PAGE
Table 2.1. Conversion of S-Parameters to Z-Parameters.....	12
Table 2.2. Conversion of Z-Parameters to S-Parameters.....	13
Table 3.1. Comparison of Different SCMR Systems.....	46
Table 4.1. Material Properties of Human Body in Simulation.....	75
Table 5.1. Bandwidth Range with Different Capacitors.....	89
Table 5.2. Data Rate Required for Different Applications.....	94

LIST OF FIGURES

FIGURE	PAGE
Figure 2.1. Schematic of standard SCMR system.	7
Figure 2.2. Equivalent circuit of an SCMR system.	7
Figure 2.3. A two-port network for SCMR system with source and load impedance. ...	10
Figure 3.1. Schematic of standard SCMR system.	16
Figure 3.2. Equivalent circuit of an SCMR system.	16
Figure 3.3. SCMR system illustrating azimuth and elevation misalignment angles, ϕ and θ , respectively.	19
Figure 3.4. SCMR system with lateral misalignment.	20
Figure 3.5. Different SCMR systems. (a) Standard SCMR with parallel loops elements. (b) Conformal SCMR. (c) 3-D SCMR. (d) Hybrid SCMR.	21
Figure 3.6. Prototype of standard SCMR system.	23
Figure 3.7. G_T of the standard SCMR system of Fig. 5(a) under different misalignment conditions. (a) Angular azimuth misalignment. (b) Angular elevation misalignment. (c) Lateral misalignment.	24
Figure 3.8. G_T of standard SCMR vs. distance.	25
Figure 3.9. Schematic of conformal SCMR system.	27
Figure 3.10. Prototype of conformal SCMR system.	27
Figure 3.11. G_T of CSCMR system of Fig. 5(b) under different misalignment conditions. (a) Angular azimuth misalignment. (b) Angular elevation misalignment. (c) Lateral misalignment.	29
Figure 3.12. G_T of CSCMR vs. distance.	30
Figure 3.13. 3-D SCMR TX or RX system.	32
Figure 3.14. Prototype of 3-D SCMR system.	33
Figure 3.15. G_T of 3-D SCMR system of Fig. 3.5(c) under different misalignment conditions. (a) Angular azimuth misalignment. (b) Angular elevation misalignment. (c) Lateral misalignment.	35

Figure 3.16. G_T of 3-D SCMR vs. distance.	36
Figure 3.17. A two-port network for SCMR system with source and load impedances..	38
Figure 3.18. Operating power gain of 3-D SCMR.	39
Figure 3.19. Schematic of HSCMR system.	40
Figure 3.20. G_T of hybrid SCMR system of Fig. 5(d) under different misalignment conditions. (a) Angular azimuth misalignment. (b) Angular elevation misalignment. (c) Lateral misalignment.	43
Figure 3.21. G_T of HSCMR vs. distance.	43
Figure 4.1. SCMR system illustrating azimuth angular misalignment.	49
Figure 4.2. A two-port network for SCMR system with source and load impedance. ...	49
Figure 4.3. Measurement setup of conventional conformal SCMR for 180° of misalignment.	52
Figure 4.4. Simulated Q-factor of elements of conventional CSCMR system.....	53
Figure 4.5. Misalignment results of conventional conformal SCMR.....	54
Figure 4.6. Schematic of proposed cylindrical SCMR based on wire elements.....	55
Figure 4.7. Simulated Q-factor of elements of proposed cylindrical SCMR system based on wire elements.....	56
Figure 4.8. Measurement setup of proposed cylindrical SCMR based on wire elements for 180° of misalignment.	57
Figure 4.9. Misalignment results of proposed cylindrical SCMR based on wire elements.	58
Figure 4.10. Magnetic field generated by (a) conventional CSCMR, and (b) proposed cylindrical SCMR.	60
Figure 4.11. Simulated results of three proposed cylindrical SCMR systems based on wire elements with different cross-sectional radii.	61
Figure 4.12. Schematic of proposed cylindrical SCMR based on flexible PCB.	63
Figure 4.13. Simulated Q-factor of elements of proposed cylindrical SCMR system with flexible PCB.....	63

Figure 4.14. Measurement setup of proposed cylindrical SCMR with flexible PCB for 180° of misalignment.	64
Figure 4.15. Misalignment results of proposed flexible PCB cylindrical SCMR.....	65
Figure 4.16. Simulation model of flexible PCB cylindrical SCMR with cylindrical TX and RX elements.	67
Figure 4.17. Simulated misalignment result of flexible PCB cylindrical SCMR with cylindrical structures for both TX and RX elements.	68
Figure 4.18. Measured x-axis lateral misalignment results of conventional CSCMR and proposed cylindrical SCMR with flexible PCB.....	70
Figure 4.19. Measured z-axis lateral misalignment results of conventional CSCMR and proposed cylindrical SCMR with flexible PCB.....	71
Figure 4.20. Demonstration of wearable cylindrical SCMR in simulation.....	72
Figure 4.21. Wearable cylindrical SCMR in measurement setup.	74
Figure 4.22. Misalignment results of wearable cylindrical SCMR system from 0° to 180° (this angle range corresponds to angles 90° to 270° per the setup of Fig. 4.15).....	76
Figure 4.23. Optimized cylindrical SCMR system based on wire elements.	78
Figure 4.24. Simulated Q-factor of elements of optimized cylindrical SCMR system based on wire elements.	78
Figure 4.25. Comparison of simulated misalignment results of proposed and optimized cylindrical SCMR systems based on wire elements.	79
Figure 5.1. Geometry of a broadband CSCMR TX or RX element (a) wire-based, (b) PCB-based.....	82
Figure 5.2. Electrical equivalent radius from circular cylindrical wire.	83
Figure 5.3. Simulated efficiency results of different trace width.....	84
Figure 5.4. Simulated efficiency results of different r_2/r_1 ratio.....	85
Figure 5.5. Simulated efficiency results of different r_3/r_2 ratio	86
Figure 5.6. Simulated efficiency results of different d/r_3 ratio.....	86
Figure 5.7. Q-factors of the two resonators.....	87

Figure 5.8. Simulated efficiency results of different capacitor values	88
Figure 5.9. Simulated and measured efficiency results of the broadband planar CSCMR system.....	90
Figure 5.10. Block diagram of the system description	91
Figure 5.11. Lossless terminated transmission line.....	91
Figure 5.12. Simulation schematic of the backscattering modulation.....	92
Figure 5.13. Schematic of the power transmitter/data receiver.....	95
Figure 5.14. Schematic of the power receiver/data transmitter.....	96
Figure 5.15. Simulation schematic of the system.....	97
Figure 5.16. Measurement setup.....	97
Figure 5.17. Simulated efficiency results for broadband and standard CSCMR systems.....	98
Figure 5.18. Simulated received data comparison between broadband and standard CSCMR systems.....	99
Figure 5.19. Measured RF-to-DC power conversion efficiency.....	100
Figure 5.20. Input and received data signal.....	101

CHAPTER 1

INTRODUCTION

1.1 Problem Statement

Advances in wireless communication and semiconductor technology have enabled a wide variety of portable consumer electronic, medical and industrial devices, such as electric vehicles [1], RFID [2] [3], implanted medical devices (IMD) [4], and mobile devices [5]. However, users are still required to manually plug in these mobile devices to charge, thereby limiting their mobility and disrupting use when charging is required. Furthermore, as portable devices reduce in size, connectors occupy a larger fraction of the system size. Wireless power offers the possibility of connector-free electronic devices, which could improve both size and reliability. Also, it is essential for embedded (i.e., concrete sensors), implantable (i.e., pacemakers) and wearable sensors (i.e., pulse monitor) to be powered wirelessly to extend their lifetime as well as enhance mobility and functionality.

Previously, the main technology for near-field wireless power transfer was inductive coupling. However, this method can only achieve high efficiency when the transmitting distance is very small, which limits its applications significantly. Recently, the Strongly Coupled Magnetic Resonance (SCMR) method was introduced, which can transmit power with high efficiency at relatively larger distance [6-8]. An important advantage of SCMR method is that it is a non-radiative field method, which means that most of the power that is not harvested by the receiving coil remains bound to the vicinity of the transmitting unit and it is not radiated into the environment. Another advantage of

SCMR is that it is safer for humans, as it relies on magnetic near-fields which interact very weakly with biological tissues [9]. This makes SCMR a superior technology over inductive coupling methods and opens up a lot more possibilities for various applications.

However, since SCMR is a relatively new technology, studies are still being done on how to optimize the configurations and performance of SCMR systems. Most SCMR systems are designed with loops or coils, which result in high angular misalignment sensitivity. Therefore, novel SCMR topologies are needed to address this problem. Specifically, two new 3-D SCMR systems will be developed in order to achieve angular misalignment insensitivity and their performance will be compared to the one of standard SCMR systems.

In the last few decades, wireless sensors have been widely adopted in numerous applications [10-13]. However, wireless sensors are still mostly powered by batteries which impose strict limitations on the lifetime of the sensors. WPT systems that can wirelessly power embedded and implantable sensors will be beneficial for a variety of applications, eliminating the need for batteries. Moreover, combining wireless power transfer and data communication is a unique and efficient way to accomplish near-field power and communication through the same wireless link. That is achieved by developing planar broadband CSCMR systems that can support high data rate communication.

1.2 Research Objectives and Contributions

Previous work has been performed on improving various aspects of SCMR systems. However, there is limited research on improving the angular misalignment

sensitivity of SCMR systems. Therefore, the first goal of this research is to develop new SCMR systems that are misalignment insensitive. Misalignment insensitive WPT systems provide better mobility to the user as they can constantly transfer power to a moving receiver. Most WPT systems use planar structures and cannot transmit power when the transmitter and receiver are perpendicular to each other (i.e., in this case their efficiency drops to zero). Ideally, a misalignment insensitive system should provide a constant power across all 360° of angular misalignment.

The second part of this dissertation is to develop a broadband planar conformal SCMR system and transfer power and data simultaneously. This system is not only broadband but also easy to manufacture. Broadband SCMR systems can be used to wirelessly send power and data through the same link. Backscattering modulation is used here to achieve high-data rate communication and enable the development of the first battery-less sensors that simultaneously receive their power and transmit their data through the same wireless link.

1.3 Methodology

For all our designs, analytical methods are used to design the optimal models. Then the performance of the SCMR systems is optimized by simulation tools, such as, ANSYS HFSS and Designer. Furthermore, prototypes are built to validate the performance of our designs. All measurements are performed using a Vector Network Analyzer (VNA). First, in order to have a design that is misalignment insensitive, 3-D designs are developed, since planar structures have zero efficiency when the transmitter and receiver are perpendicular to each other. By using a 3-D structure, e.g., a spherical

structure formed by continuous orthogonal loops, or a cylindrical structure, the system can achieve misalignment insensitivity. Specifically, angular misalignment sensitivity is improved with two spherical structures serving as transmitter and receiver, while a cylindrical structure is able to accomplish misalignment insensitivity with a conformal structure serving as a transmitter or receiver. Comparison between the proposed designs and conventional SCMR systems will be also made.

Second, planar broadband CSCMR systems are developed. These CSCMR systems are used to wirelessly send power and data simultaneously. An RF-to-DC circuit utilizing a bridge rectifier is used to harvest the RF power. Backscattering modulation is used as the modulation scheme and an envelope detector is used as demodulator. The system performance is simulated in Advanced Design System (ADS) and validated through measurements.

1.4 Dissertation Outline

The dissertation is organized as follows: Chapter 2 reviews the existing literature of Wireless Power Transfer and Strongly Coupled Magnetic Resonant Systems. In Chapter 3, the design and performance of the first misalignment insensitive WPT systems are presented, which are based on two orthogonally connected copper wire structures. In Chapter 4, the second misalignment insensitive system is presented, which is based on a cylindrical structure. In Chapter 5, broadband CSCMR systems are developed based and it is integrated with a backscattering modulator. With these systems, wireless and battery-less sensors are possible. Finally, Chapter 6 provides the conclusions of this dissertation. Suggestions for future research are also discussed in this chapter.

CHAPTER 2

BACKGROUND AND RELATED WORK

In this chapter, we review existing literature related to the issues involved in Wireless Power Transmission (WPT) and Strongly Coupled Magnetic Resonance (SCMR). Several WPT methods are presented and compared in Section 2.1. The recent methods that used SCMR technology are described in detail in Section 2.2.

2.1 Wireless Power Transmission (WPT) Techniques

The advances of wireless power technology have been applied across a broad spectrum of applications nowadays [14-16]. The portable electronic devices (e.g., mobile phones, laptops), electric vehicles, embedded sensors and biomedical implant devices need instantaneous or continuous energy [17-18]. The traditional powering wires or bulky batteries are heavy and expensive to operate.

Wireless powering was first proposed by Nikola Tesla, whose goal was to distribute power wirelessly to the entire earth from his Wardencllyffe Tower [1-3] via an electric field in 1901. Due to a lack of funds and techniques, his experiment was not finished. In 1964, William C. Brown proposed the first wireless power transfer scheme via microwave beams [14]. In 1970, Peter Glaser conceived that space solar energy could be converted into electrical energy, which would be transferred via microwaves [19-20]. In the late 1970s, the WPT technique via radiative EM wave for long-distance attracted interest in industrial, telecommunication, and medical applications [21-23]. Later, in the early 21st century, non-radiative wireless power techniques via EM inductive coupling were developed greatly [24-28]. In 2007, the Strongly Coupled Magnetic Resonance

(SCMR) method was discovered by a team of MIT scientists [6] who in their original experiment transferred 60 watts of power at a distance of 200 cm to illuminate a light bulb [4]. Later, this technique was extended to power multiple devices simultaneously in air, and 60% efficiency was reported for a distance of 200 cm [24].

2.2 Strongly Coupled Magnetic Resonance (SCMR)

Recently, the Strongly Coupled Magnetic Resonance (SCMR) method was introduced, which is based on resonant inductive coupling. SCMR can achieve highly efficient wireless power transfer to larger distances [2-7]. The SCMR method works in mid-range, i.e., 10-300 cm. Compared to traditional WPT methods based on inductive coupling, the SCMR method is based on high resonant coupling, which is more efficient and reliable over distance, flexible in orientations and easy to simultaneously power multiple devices [6], [45].

2.2.1 Basic Principle of SCMR System

A standard SCMR system is shown in Fig. 2.1 and it consists of the following: (a) a transmitter with one source loop, where the excitation is connected, and a TX resonator coil or loop, and (b) a receiver with one load loop, where the load is connected, and an RX resonator coil or loop. In order for SCMR to achieve high WPT efficiency, the TX and RX resonators must resonate at the same frequency, which is also the frequency where the resonators naturally exhibit the highest Q-factor. It is this condition indeed that enables SCMR to achieve WPT efficiencies that are significantly greater than inductively coupled or resonant inductively coupled systems. This has been confirmed in [22] where three types of WPT systems of the same size and operating frequency were compared,

namely: (a) a non-resonant inductively coupled system, (b) a resonant inductively coupled system, and (c) an SCMR system. The equivalent circuit of an SCMR system is shown in Fig. 2.2.

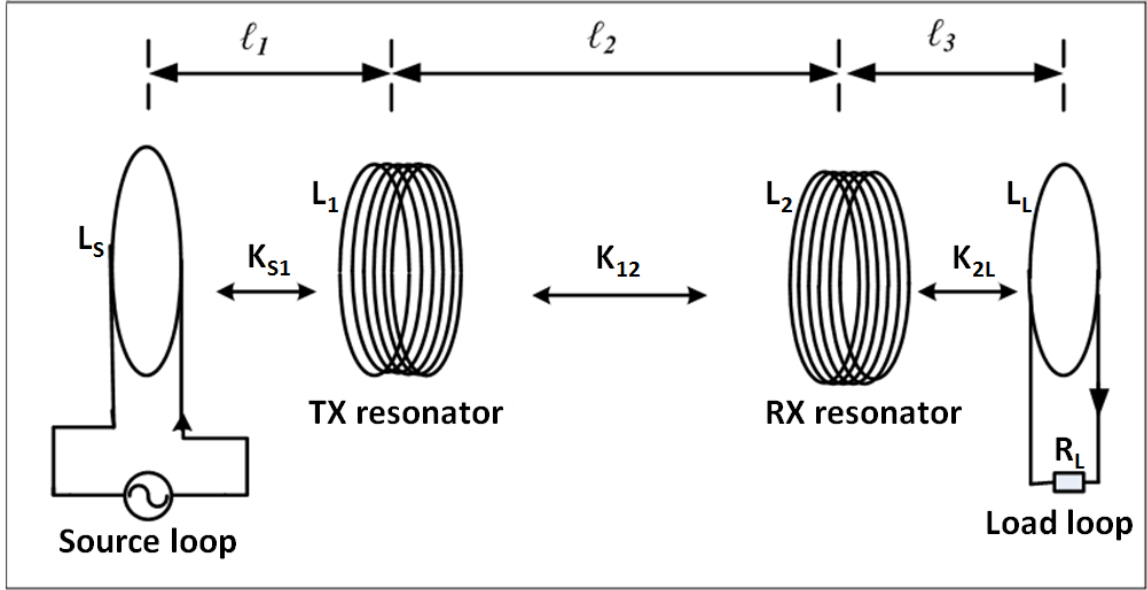


Figure 2.1. Schematic of standard SCMR system.

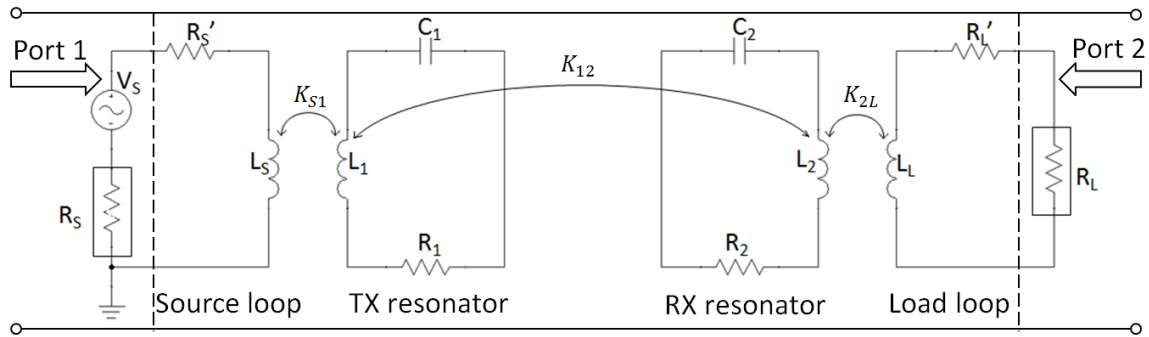


Figure 2.2. Equivalent circuit of an SCMR system.

In Fig. 2.2, R_S and R_L are the internal resistances of the input and output ports, respectively; $R_{S'}$, R_1 , R_2 and $R_{L'}$ are the total resistances of the source loop, TX resonator, RX resonator, and load loop, respectively; L_S , L_1 , L_2 and L_L are the corresponding inductances of these loops; C_1 and C_2 are the external capacitors connected to the TX and

RX resonator loops; K_{SJ} , K_{J2} and K_{2L} are the coupling coefficients between the loops. The input and output ports are shown in Fig. 2.2 as port 1 and port 2, respectively. The source loop delivers power to the TX resonator through inductive coupling, and the RX resonator delivers power to the load loop through inductive coupling. Then, the TX resonator efficiently transfers power to the RX resonator over large distances by satisfying the SCMR condition (i.e., both TX and RX resonators resonate at the same frequency, where their Q-factor is naturally maximum). The size of the resonators of an SCMR system is determined by the frequency where the Q-factor is maximum. The frequency where the Q-factor of a loop is maximum can be written as [34]:

$$f_{\max} = \frac{c^{8/7} \mu_0^{1/7} \rho^{1/7}}{4 \cdot 15^{2/7} \pi^{11/7} r_c^{2/7} r^{6/7}} \quad (2.1)$$

where μ_0 is the permeability of free space, ρ is the loop's material resistivity, r_c is the cross-sectional radius of the loop, and r is the radius of the loop. In order to design a proper SCMR system that operates at a certain frequency, f_0 , with high efficiency, the following equation must be satisfied:

$$f_0 = f_{\max} \quad (2.2)$$

Based on (2.1) and (2.2), the radii of the TX and RX resonator loops are equal to:

$$r = \frac{c^{4/3} \mu_0^{1/6} \rho^{1/6}}{4^{7/6} 15^{1/3} \pi^{11/6} r_c^{1/3} f_0^{7/6}} \quad (2.3)$$

In order to form resonant TX and RX loops, a lumped capacitor must be connected on each of these loops. This capacitor can be calculated using the following formula:

$$L = \mu_0 r \left[\ln \left(\frac{8r}{r_c} \right) - 2 \right] \quad (2.4)$$

$$C = \frac{1}{(2\pi f_{\max})^2 L} \quad (2.5)$$

where L is the equivalent inductance of each TX and RX loop. Therefore, the TX/RX resonators can be designed using (2.2)-(2.5). The source and load coils in all of our designs are scaled versions (i.e., have same geometrical shape) of the TX and RX resonator coils. Therefore, the scaling factor that scales the TX (or RX) resonator coil to the source (or load) resonator coil is the only parameter that needs to be determined once the TX and RX resonators are designed. ANSYS HFSS is used to optimize this scaling factor in order to achieve optimal power transfer efficiency. Based on our design experience and simulation results, the size of the source and load coils is typically 1/2 to 3/5 of the resonator size. It has been shown by several papers [41], [51] that the typical distance at which an SCMR system exhibits maximum efficiency is approximately equal to the diameter of the TX and RX resonators.

2.2.2 Power Transfer Efficiency of SCMR System

In order to quantify SCMR system power transfer efficiency, the transducer power gain is used since it accounts for both source and load mismatches. The transducer power gain is defined as the ratio of power delivered to the load to the power available from the source. The entire SCMR WPT system is considered as a two-port network. In order to better understand the power gain definition, this two-port network with source and load impedance is shown in Fig. 2.3.

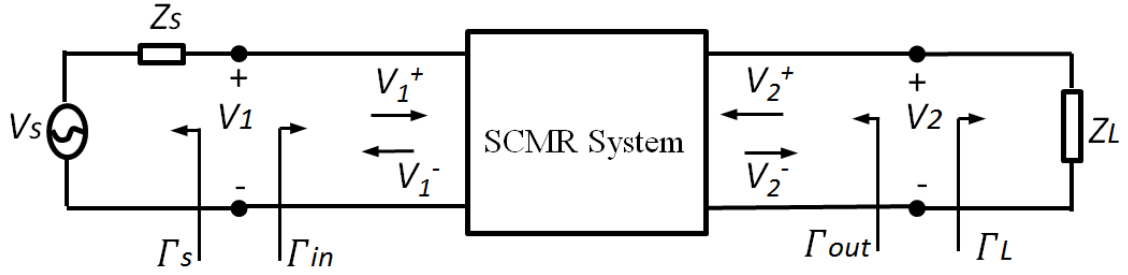


Figure 2.3. A two-port network for SCMR system with source and load impedance.

The transducer power gain can be defined in terms of S-parameters per [31] as follows:

$$G_T = \frac{P_L}{P_{avs}} = \frac{|S_{21}|^2 (1 - |\Gamma_s|^2)(1 - |\Gamma_L|^2)}{|1 - \Gamma_s \Gamma_{in}|^2 |1 - S_{22} \Gamma_L|^2} \quad (2.6)$$

where P_L is the power delivered to the load, and P_{avs} is the power available from the source. With reference to Fig. 4, the reflection coefficient seen looking toward the source is:

$$\Gamma_s = \frac{Z_s - Z_0}{Z_s + Z_0} \quad (2.7)$$

while the reflection coefficient seen looking toward the load is:

$$\Gamma_L = \frac{Z_L - Z_0}{Z_L + Z_0} \quad (2.8)$$

where Z_0 is the characteristic impedance reference for the scattering parameters of the two-port network. The mismatch corresponding to the input impedance of the terminated two-port network is given by the reflection coefficient Γ_{in} , and it is defined as

$$\Gamma_{in} = S_{11} + \frac{S_{12} S_{21} \Gamma_L}{1 - S_{22} \Gamma_L} \quad (2.9)$$

We assume in all our designs that the source and load impedances are 50Ω , which, according to (2.7) and (2.8), makes $\Gamma_s = \Gamma_L = 0$, and reduces (6) to $G_T = |S_{21}|^2$. Therefore, in this paper, the power transfer efficiency, η , of all our designs is equal to G_T and it is defined as

$$\eta = |S_{21}|^2 \quad (2.10)$$

The efficiency of our prototypes is measured using a vector network analyzer and it is based on the S-parameters. Specifically, ports 1 and 2 of the network analyzer are connected to the transmitter and receiver, respectively, and the S-parameters are measured. Then, the data of the measured efficiency is calculated by directly programming the equation $|S_{21}|^2$ on the network analyzer.

We assume the input and output impedances are matched to 50Ω . However, in certain cases, the input and output impedances may not be 50Ω . Some recent studies have provided insight on optimizing the total system efficiency that includes the effects of the power amplifier and rectifier [55] [56]. This paper concentrates on examining the misalignment performance of the proposed cylindrical systems. The optimization flow described in our paper including equations (2.1)-(2.5) is still consistent for imbalanced impedance situations since this flow derives designs that satisfy the fundamental condition for SCMR systems to exhibit maximum efficiency, i.e., the TX and RX resonators must resonate at the same frequency, which is also the frequency where the resonators naturally exhibit the highest Q-factor. In the case of imbalanced impedance, different approaches, which improve the performance of the entire system, can be followed. For example, a matching network can be used between the WPT elements and

the amplifier and/or rectifier. Also, in cases where the designer chooses a reference impedance that is different than 50Ω , the following process can be used to convert the measured and/or simulated S-parameters based on 50Ω reference to another impedance. First, convert the S-parameters based on 50Ω reference ($Z_0 = 50\Omega$) to Z-parameters using the equations shown in Table 2.1. Second, set Z_0 to the new reference impedance and convert the Z-parameters to the new S-parameters for the new reference impedance using the equations shown in Table 2.2 [57].

Table 2.1. Conversion of S-Parameters to Z-Parameters

Z_{11}	$Z_0 \frac{(1+S_{11})(1-S_{22})+S_{12}S_{21}}{(1-S_{11})(1-S_{22})-S_{12}S_{21}}$
Z_{12}	$Z_0 \frac{2S_{12}}{(1-S_{11})(1-S_{22})-S_{12}S_{21}}$
Z_{21}	$Z_0 \frac{2S_{21}}{(1-S_{11})(1-S_{22})-S_{12}S_{21}}$
Z_{22}	$Z_0 \frac{(1-S_{11})(1+S_{22})+S_{12}S_{21}}{(1-S_{11})(1-S_{22})-S_{12}S_{21}}$
Z_0 is the reference impedance	

Table 2.2. Conversion of Z-Parameters to S-Parameters

S_{11}	$\frac{(Z_{11}-Z_0)(Z_{22}+Z_0)-Z_{12}Z_{21}}{\Delta Z}$
S_{12}	$\frac{2Z_{12}Z_0}{\Delta Z}$
S_{21}	$\frac{2Z_{21}Z_0}{\Delta Z}$
S_{22}	$\frac{(Z_{11}+Z_0)(Z_{22}-Z_0)-Z_{12}Z_{21}}{\Delta Z}$

$$\Delta Z = (Z_{11}+Z_0)(Z_{22}+Z_0)-Z_{12}Z_{21}$$

Z_0 is the reference impedance

2.2.2 Misalignment Analysis

Even though SCMR exhibits higher efficiency than inductive coupling, its performance is highly sensitive to the alignment between the transmitter and receiver elements. An optimization technique for improving the efficiency of SCMR systems under lateral misalignment was presented in [33]. Specifically, 48.4% efficiency was achieved by using an adaptive matching network. However, no solution for angular misalignment was proposed in [33]. Also, the effects of few misalignment angles on SCMR's efficiency were examined in [34] and [35]. However, the main focus of [34] and [35] was to study multiple transmitter/receiver WPT systems and their misalignment analysis was very limited. Analytical formulations for the power transfer efficiency of inductive links under lateral and angular coil misalignment were presented in [36]. Two novel SCMR topologies were proposed in [37] but their efficiency was only studied for a maximum angular misalignment of 90°. Furthermore, analytical models for SCMR that

incorporate misalignment effects were presented in [38]. SCMR's radial and angular misalignment sensitivity were examined by [39] and [40], respectively. SCMR's angular misalignment sensitivity was decreased through the use of tuning circuits but high efficiency was not achieved above 60° of misalignment rotation. An omnidirectional wireless power transfer method that utilizes current phase shifting between power inputs was studied in [41]. However, the requirement of different current control in three separated source loops can be difficult to implement in practice. Further investigation of this method can also be found in [42]. Angular misalignment was also examined in [43] that reconfigured the WPT system using switching between different-size source loops and load loops thereby increasing the complexity of the WPT system and making its practical implementation difficult. A new misalignment insensitive SCMR system, which exhibits no nulls in power transfer efficiency in the azimuth plane, was presented in [44]. However, such a system requires three-dimensional elements for both transmitter and receiver, which in some applications cannot be easily implemented. Researches have been done on misalignment insensitive wireless power transfer systems [65-70]. Most common method they use is utilizing two orthogonal separated loops as transmitter and two separated power input is needed. Voltage controlled phase shifter is used to control the two power inputs to make sure they are 180° phase different. Even though this method is valid, the requirement of two separated power input is not ideal. Also, the addition of voltage controlled phase shifter adds to the complexity of the system.

CHAPTER 3

MISALIGNMENT SENSITIVITY OF STRONGLY COUPLED WIRELESS POWER TRANSFER SYSTEMS

In this chapter, the design of 3-D misalignment insensitive Strongly Coupled Magnetic Resonant Systems are studied. Its misalignment performances in azimuth and elevation plane as well as in lateral are studied and compared to previous SCMR designs. The misalignment analysis of standard and conformal SCMR is described in Section 3.1. The proposed 3-D misalignment insensitive SCMR system is presented in Section 3.2, which achieves misalignment insensitivity throughout the 360° angular azimuth rotation. The comparison among all the designs presented previously is discussed in Section 3.3. This novel structured SCMR system offers no null performance for the entire angular azimuth misalignment, which is hugely improved upon previous wireless power system designs. However, due to the fact that both the transmitter and receiver have to be 3-D in this case, there is room for improvement in the future.

3.1 Misalignment Analysis of Standard and Conformal SCMR Systems

The WPT systems proposed in this paper are based on the Strongly Coupled Magnetic Resonance (SCMR) method [6]. A typical SCMR system is shown in Fig. 3.1 and it consists of the following: (a) a transmitter with one source loop where the excitation is connected and a TX resonator coil or loop, and (b) a receiver with one load loop where the load is connected and an RX resonator coil or loop. In order for SCMR to achieve high WPT efficiency the TX and RX resonators must resonate at the same frequency, which also is the frequency where the resonators naturally exhibit the highest

Q-factor. It is this condition indeed that enables SCMR to achieve WPT efficiencies that are significantly larger than standard two loops or coils inductively coupled or resonant inductively coupled systems. This has been confirmed in [24] where three types of WPT systems of the same size and operating frequency were compared, namely: (a) a non-resonant inductively coupled system, (b) a resonant inductively coupled system, and (c) an SCMR system. The equivalent circuit of an SCMR system is shown in Fig. 3.2.

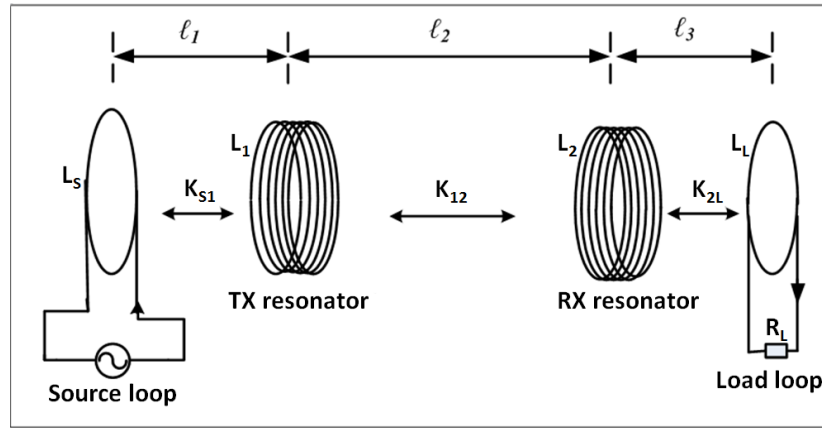


Figure 3.1. Schematic of standard SCMR system.

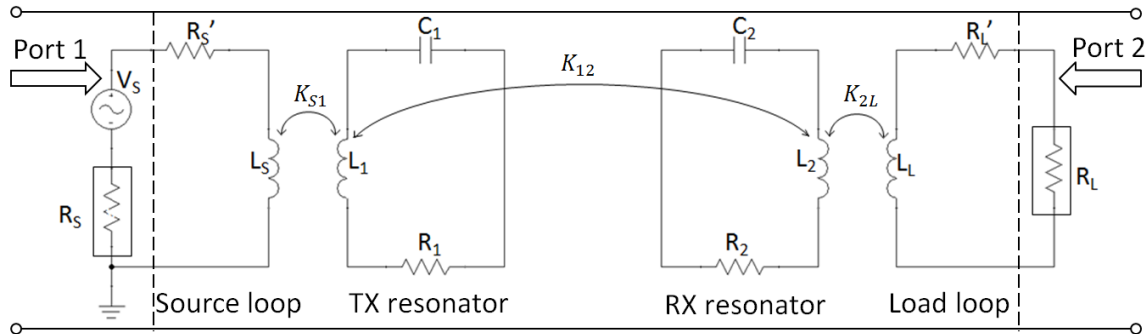


Figure 3.2. Equivalent circuit of an SCMR system.

In Fig. 3.2, R_S and R_L are respectively the internal resistances of the input and output ports; R_S' , R_1 , R_2 and R_L' are the total resistances of the source loop, TX resonator, RX resonator, and load loop, respectively; L_S , L_1 , L_2 and L_L are the corresponding inductances of these loops; C_1 and C_2 are the external capacitors connected to the TX and

RX resonator loops; K_{S1} , K_{12} and K_{2L} are the coupling coefficients between the loops. Also, the input and output ports are shown in Fig. 3.2. The source loop delivers power to the TX resonator through inductive coupling, and similarly the RX resonator delivers power to the load loop through inductive coupling. The TX resonator efficiently transfers power to the RX resonator over large distances by satisfying the SCMR condition (i.e., both TX and RX resonators resonate at the same frequency where their Q -factor is naturally maximum). The frequency where the Q -factor of a loop is maximum can be written as [25]:

$$f_{\max} = \frac{c^{8/7} \mu_0^{1/7} \rho^{1/7}}{4 \cdot 15^{2/7} \pi^{11/7} r_c^{2/7} r^{6/7}} \quad (3.1)$$

where μ_0 is the permeability of free space, ρ is the loop's material resistivity, r_c is the cross-sectional radius of the loop, and r is the radius of the loop. In order to design a proper SCMR system that operates at a certain frequency, f_0 , with high efficiency, the following equation must be satisfied:

$$f_0 = f_{\max} \quad (3.2)$$

Based on (3.1) and (3.2), the radii of the TX and RX resonator loops are equal to:

$$r = \frac{c^{4/3} \mu_0^{1/6} \rho^{1/6}}{4^{7/6} 15^{1/3} \pi^{11/6} r_c^{1/3} f_0^{7/6}} \quad (3.3)$$

In order to form resonant TX and RX loops, a lumped capacitor must be connected on each of these loops. This capacitor can be calculated using the following formula:

$$L = \mu_0 r \left[\ln \left(\frac{8r}{r_c} \right) - 2 \right] \quad (3.4)$$

$$C = \frac{1}{(2\pi f_{\max})^2 L} \quad (3.5)$$

where L is the inductance of each TX and RX loop. Therefore, the TX/RX resonators can be designed using (3.2)-(3.5). The source and load coils in all of our designs are scaled versions (i.e., have same geometrical shape) of the TX and RX resonator coils. Therefore, the scaling factor that scales the TX (or RX) resonator coil to the source (or load) resonator coil is the only parameter that needs to be determined once the TX and RX resonators are designed. ANSYS HFSS is used to optimize this scaling factor in order to achieve optimal power transfer efficiency. Based on our design experience and simulation results, the size of the source and load coils is typically 3/5 of the resonator size. It has been shown by several papers [7], [20] that the typical distance at which an SCMR system exhibits maximum efficiency is approximately equal to the diameter of the TX and RX resonators.

Coil orientation and alignment are critical in the design of efficient SCMR systems. In fact, conventional SCMR systems exhibit high sensitivity to angular misalignment. In Fig. 3.3, a typical standard SCMR system is shown along with the definition of azimuth and elevation misalignment angles. In Fig. 3.3, ℓ_1 is the distance between the source element and the TX resonator, ℓ_2 is the distance between the TX and RX resonators, and ℓ_3 is the distance between the RX resonator and the load element. In what follows, we explain the different types of misalignment cases that are critical for the performance of SCMR-based WPT systems.

For the angular azimuth and elevation misalignment studies presented here, the source loop and transmitter resonator stay still while the load loop and RX resonator are simultaneously rotated together around the transmitter.

A. Angular azimuth misalignment

In this case, the RX system (RX resonator and load element) rotates in the xy -plane around the z -axis from $\varphi = 0^\circ$ to 360° , while the TX system (TX resonator and source element) is fixed.

B. Angular elevation misalignment

In this case, the RX system is rotated in the yz -plane (i.e., elevation plane) from $\theta = 0^\circ$ to 360° around x -axis, while the TX system is fixed.

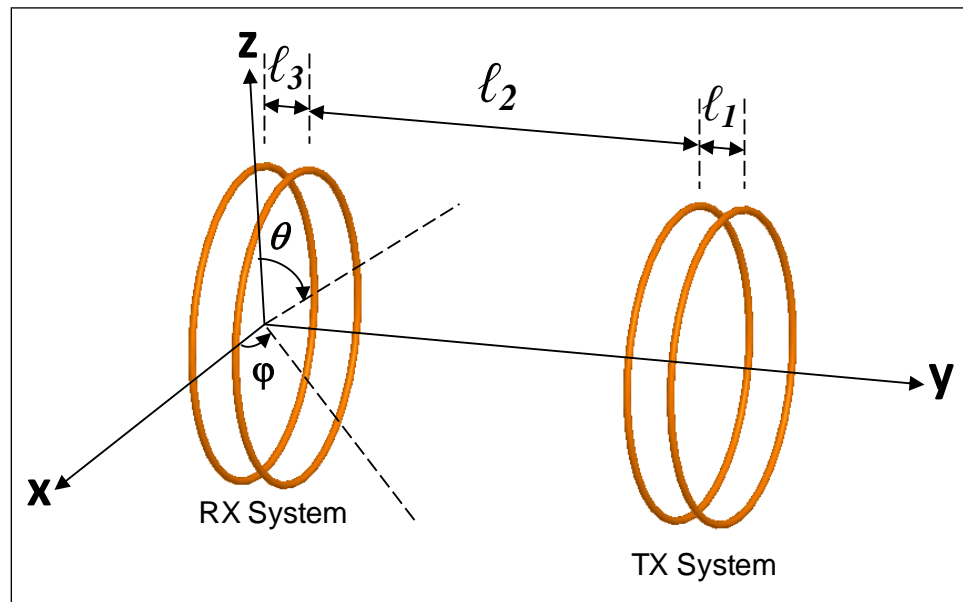


Figure 3.3. SCMR system illustrating azimuth and elevation misalignment angles, φ and θ , respectively.

C. Lateral misalignment

In this case, the RX system is misaligned by moving it parallel to the TX system while the distance between the planes of the RX and TX systems, ℓ_2 , is kept constant. The lateral misalignment offset distance, D , is shown in Fig. 3.4.

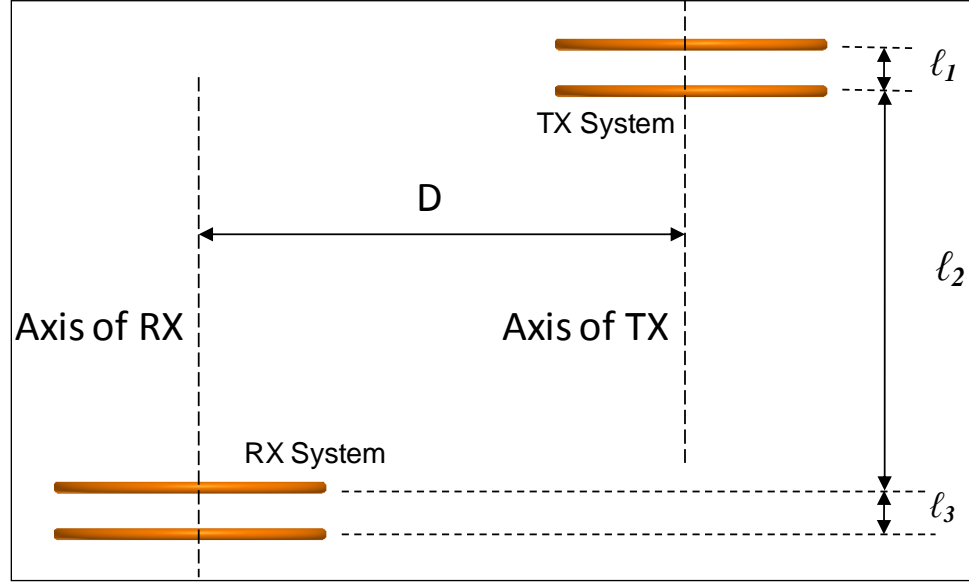


Figure 3.4. SCMR system with lateral misalignment.

Fig. 3.5(a) shows a standard SCMR system whereas our proposed novel SCMR systems, which are less sensitive to misalignment, are shown in Figs. 3.5(b)-3.5(d). The performance of these SCMR systems is examined in this section for the different misalignment conditions described in Section II. All the simulations in this paper were performed using version 16.0.0 of ANSYS HFSS [26] and Designer [27]. All SCMR resonators examined below were designed to resonate at the frequency where their Q-factor is maximum, which was accomplished by using analytical equations for the standard loops and simulations for the proposed 3-D loops.

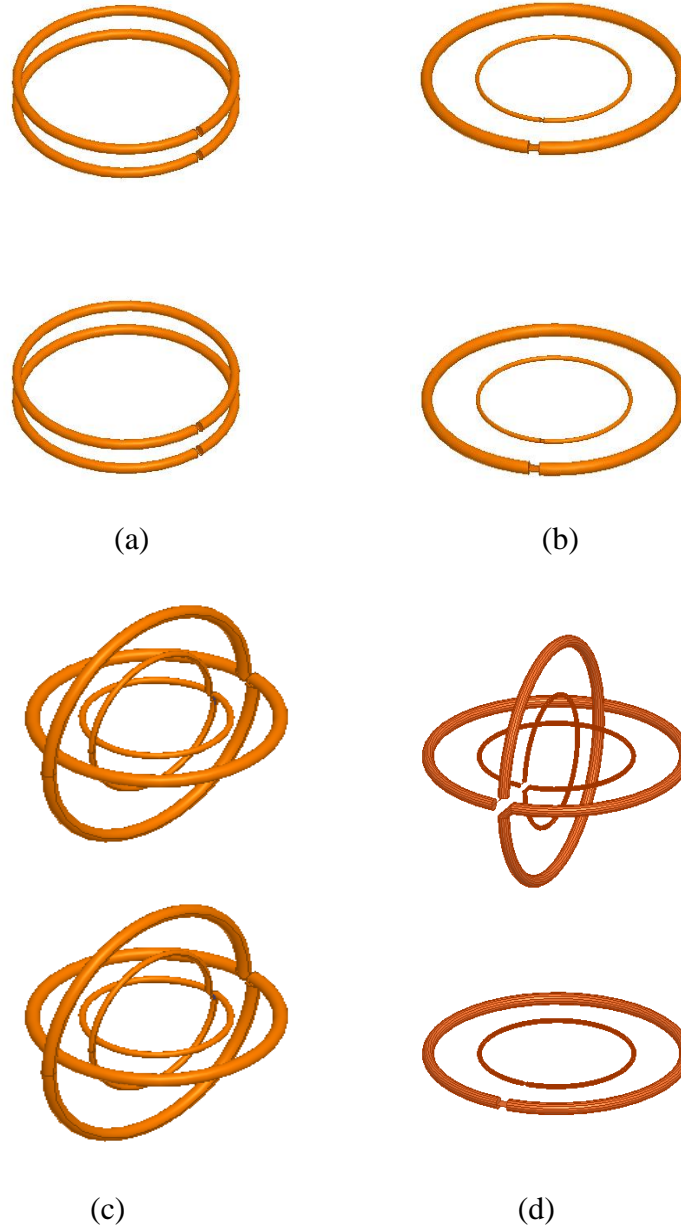


Figure 3.5. Different SCMR systems. (a) Standard SCMR with parallel loops elements. (b) Conformal SCMR. (c) 3-D SCMR. (d) Hybrid SCMR.

The entire WPT system is considered as a two-port network. It is assumed in all our designs that the source and load impedances are 50Ω . Therefore, in this paper, the following quantity is defined as

$$G_T = \text{Matched Transducer Power Gain} = |S_{21}|^2 \quad (3.6)$$

in order to compare the performance of different SCMR systems. Also, the quantity of angle range is defined, as the total range of angles for which the G_T is above a specified level. In addition, the new quantity of lateral range is defined, as the maximum lateral misalignment distance for which the G_T is above a specified level.

The gain G_T of our prototypes is measured using network analyzer based on the S -parameters. Ports 1 and 2 of the network analyzer are connected to the transmitter and the receiver, respectively and the S -parameters are measured. Then the data of the measured G_T are obtained by programming directly the equation $|S_{21}|^2$ on the network analyzer.

3.1.1 Standard SCMR

First, the performance of the conventional SCMR topology, which is shown in Fig. 3.5(a), is examined under different misalignment conditions. For angular azimuth rotation, the RX system rotates in the xy -plane around the z -axis, while the TX system is fixed. For angular elevation rotation, the RX system is rotated in the yz -plane around x -axis, while the TX system is fixed.

A standard SCMR system was designed for optimal performance following the equations presented in [25], and its prototype is shown in Fig. 3.6. The specifications of this SCMR system are as follows: the radius of the four loops is $r_l = 50\text{mm}$ and their cross-sectional radius is $r_c = 2.2\text{mm}$; $\ell_1 = \ell_3 = 23\text{ mm}$, and $\ell_2 = 120\text{ mm}$. An 18 pF capacitor is needed to achieve maximum G_T , and the operating frequency is 85.7 MHz.

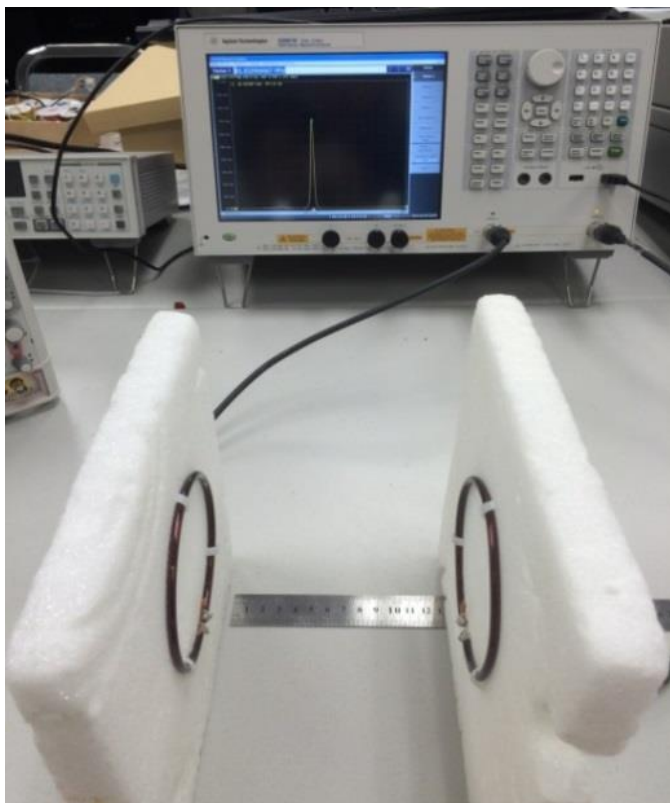
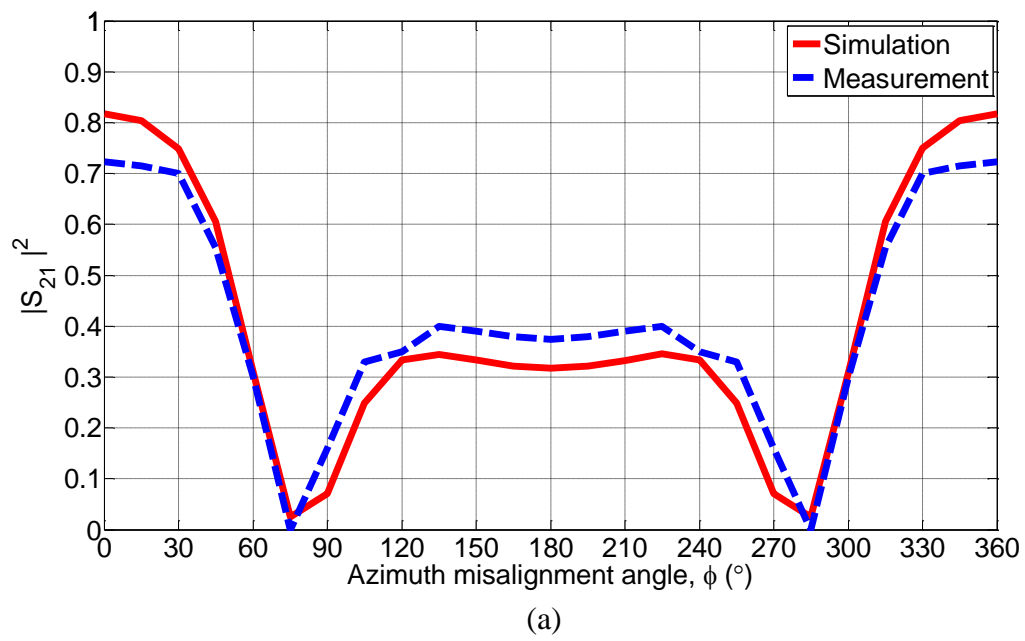
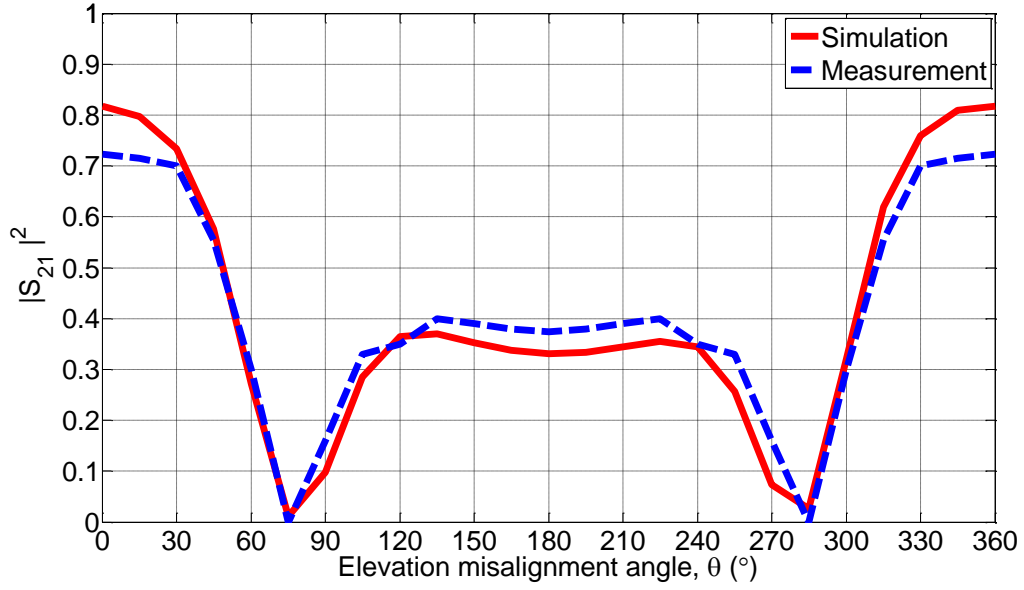
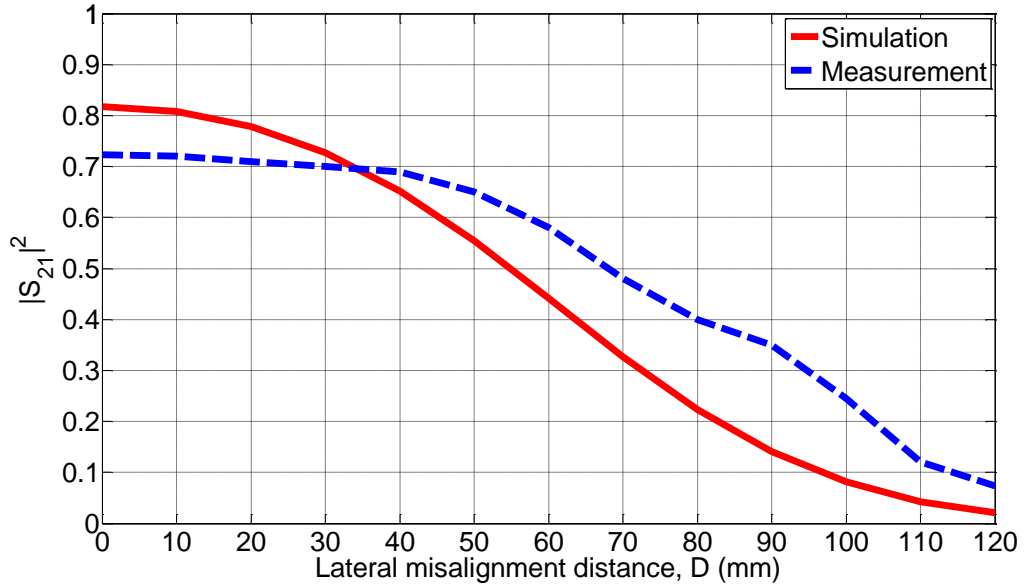


Figure 3.6. Prototype of standard SCMR system.





(b)



(c)

Figure 3.7. G_T of the standard SCMR system of Fig. 5(a) under different misalignment conditions. (a) Angular azimuth misalignment. (b) Angular elevation misalignment. (c) Lateral misalignment.

Fig. 3.7 shows the simulated and measured G_T of this standard SCMR system under the different misalignment conditions described in Section II. Fig. 3.7 clearly demonstrates the high sensitivity of conventional SCMR systems on the angular

misalignment between TX and RX systems. Also, it can be seen that $|S_{21}|^2$ drops rapidly for lateral misalignment distances that are greater than 40 mm. In what follows, the angle range and lateral range are reported based on the measured data. The results of Fig. 3.7 illustrate that SCMR's angle range for a $|S_{21}|^2$ level, which is set at 60% of its maximum, is 102° for both azimuth and elevation misalignment. The angle range for a $|S_{21}|^2$ level, which is set at 30% of its maximum, is 278° for both azimuth and elevation misalignment. The lateral range for a $|S_{21}|^2$ level, which is set at 30% of its maximum, is 78 mm. Also the G_T of this standard SCMR system exhibits two nulls at misalignment angles (azimuth or elevation) of 75° and 285° . Fig. 3.8 illustrates the range of this system.

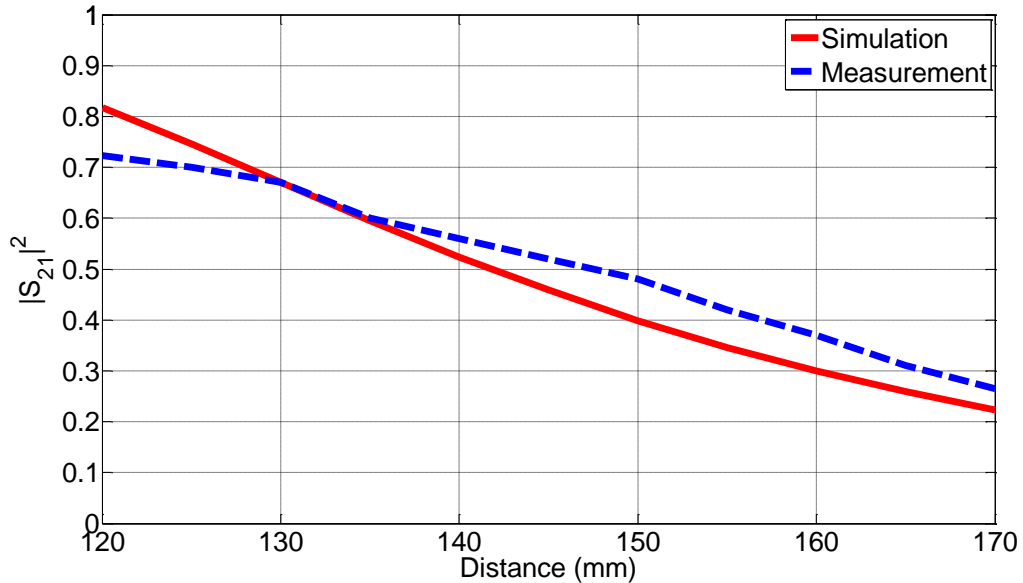


Figure 3.8. G_T of standard SCMR vs. distance.

3.1.2 Conformal SCMR (CSCMR)

The misalignment sensitivity of Conformal SCMR (CSCMR) system is studied here. For angular azimuth rotation, the RX system rotates in the xy -plane around the z -axis, while the TX system is fixed. For angular elevation rotation, the RX system is

rotated in the yz -plane around x -axis, while the TX system is fixed. In a CSCMR system, the source loop and load loop are embedded into the TX and RX resonators, respectively. Therefore, the source loop is coplanar with the TX resonator and the load loop is coplanar with the RX resonator (see Fig. 3.9). A standard SCMR system requires a separation between the source and the TX resonator as well as between the load and the RX resonator. Therefore, standard SCMR systems occupy significant volume and cannot be easily implemented in various applications. On the other hand, a conformal SCMR system has a source loop that is concentric and coplanar with the TX resonator (as well as a load loop that is concentric and coplanar with the RX resonator). Therefore, CSCMR systems are easier to implement for small devices. Furthermore, CSCMR is less sensitive to misalignment as our results will show in this section.

A CSCMR system is designed (see Fig. 3.10) with the following specifications: TX and RX resonators have a radius of 50 mm and a cross-sectional radius of 2.2 mm; the source and load loops have a radius of 30 mm and a cross-sectional radius of 0.8 mm; the distance between the TX and RX resonators is 120 mm. A 22 pF capacitor is connected to both TX and RX resonators in order for this system to operate at 76.2 MHz.

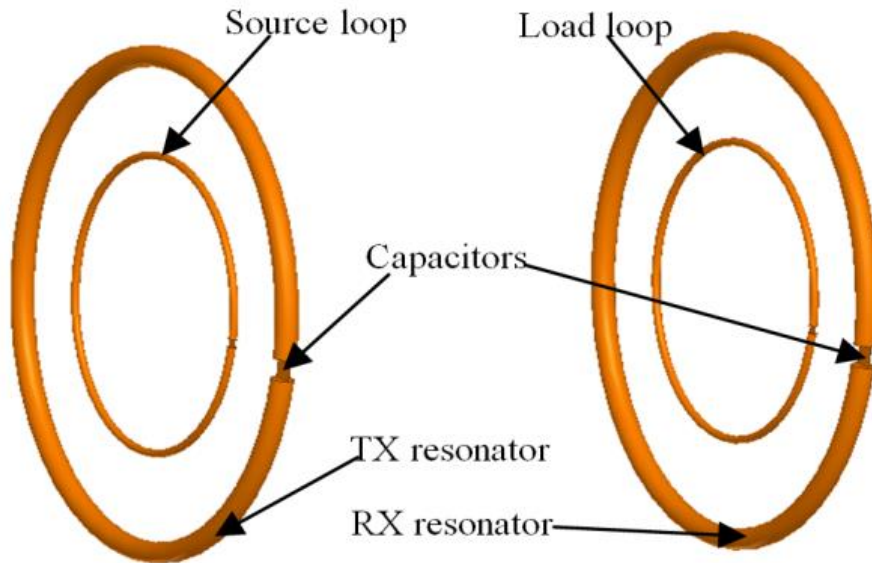


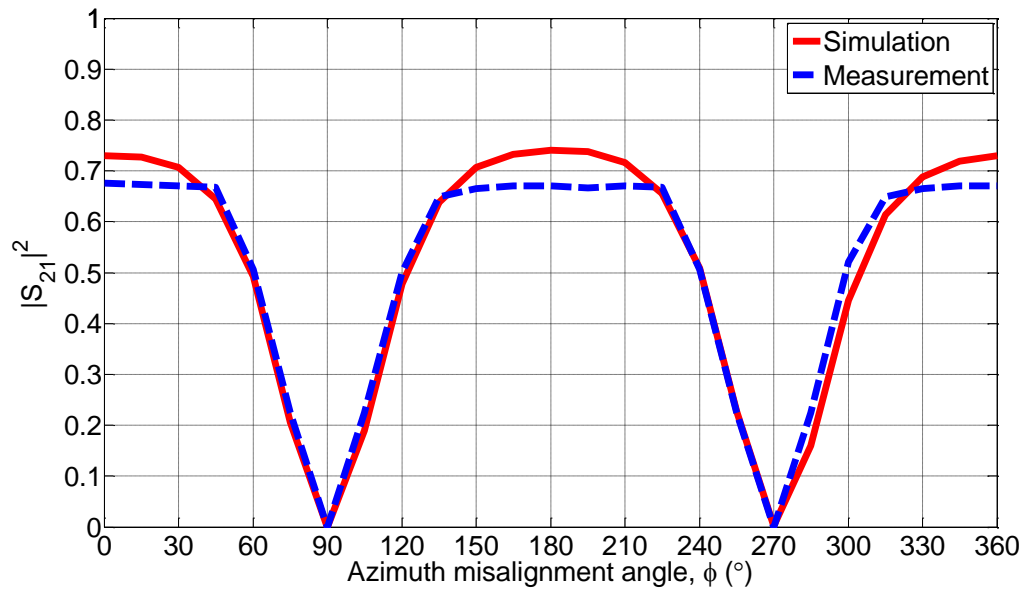
Figure 3.9. Schematic of conformal SCMR system.



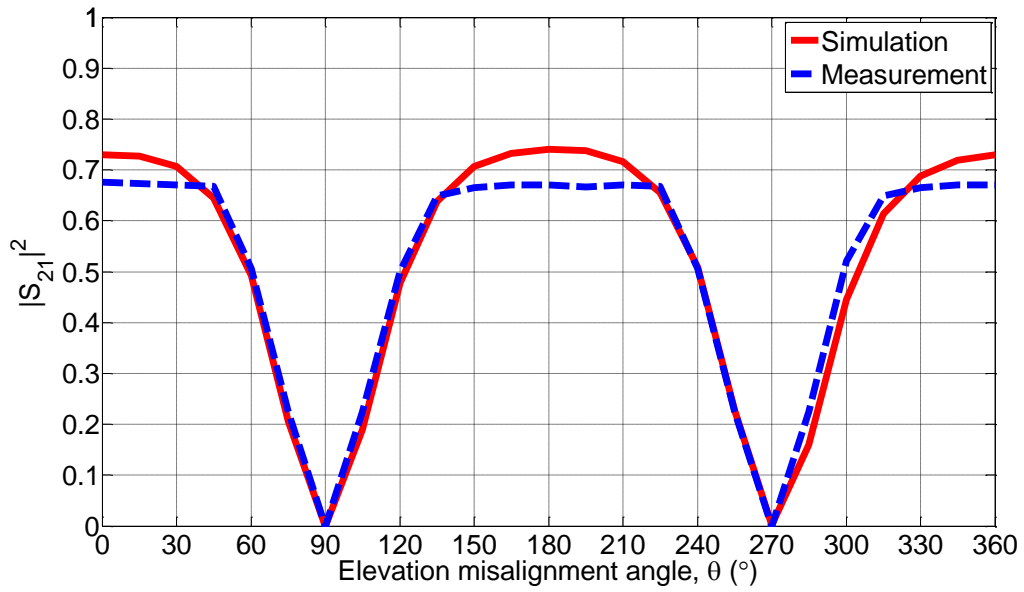
Figure 3.10. Prototype of conformal SCMR system.

Fig. 3.11 illustrates the G_T of this CSCMR system for different misalignment conditions. Fig. 3.11 shows that the G_T exhibits two nulls at 90° and 270° of azimuth or elevation misalignment. Furthermore, as the misalignment angle (azimuth or elevation)

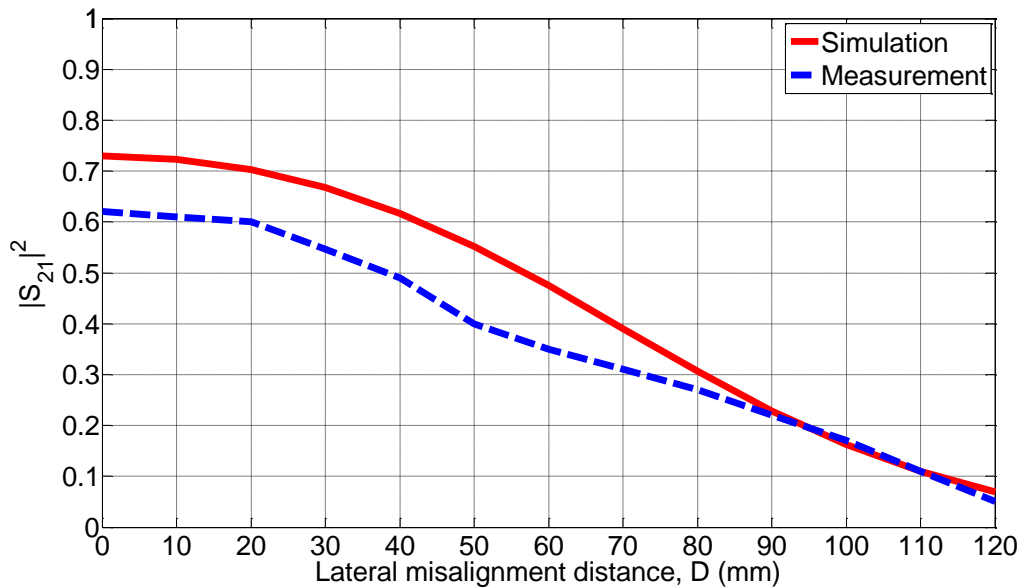
increases from 90° and 270° (null-to-null) CSCMR's G_T increases from zero to its maximum and then reduces back to zero; this is an improvement compared to the performance of standard SCMR. Specifically, as shown in Fig. 3.7, as the misalignment angle (azimuth or elevation) increases from 75° and 285° (null-to-null) standard SCMR's G_T increases from zero to only half of its maximum and then reduces back to zero. Therefore, by comparing Fig. 3.11 and Fig. 3.7, it can be concluded that CSCMR is less sensitive to azimuth and elevation misalignment than standard SCMR. Also, the results in Fig. 3.11 illustrate that CSCMR is reversible (i.e., operates with the same G_T when it is rotated in the azimuth or elevation plane by 180°) whereas standard SCMR is not. This occurs due to the geometrical symmetry of CSCMR systems.



(a)



(b)



(c)

Figure 3.11. G_T of CSCMR system of Fig. 5(b) under different misalignment conditions. (a) Angular azimuth misalignment. (b) Angular elevation misalignment. (c) Lateral misalignment.

In what follows, the angle range and lateral range are reported based on the measured data. The angle range of this CSCMR system for a $|S_{21}|^2$ level, which is set at 60% of its maximum, is 248° for both azimuth and elevation misalignment and is

significantly larger than the one (i.e., 102°) of standard SCMR. Also, the angle range of this CSCMR system for a $|S_{21}|^2$ level, which is set at 30% of its maximum, is 294° for both azimuth and elevation misalignment and is larger than the one (i.e., 278°) of standard SCMR. Furthermore, the lateral range for a $|S_{21}|^2$ level, which is set at 30% of its maximum, is 92 mm, and it is larger than the one (i.e., 78 mm) of standard SCMR. Therefore, it can be concluded that CSCMR is also less sensitive to lateral misalignment than standard SCMR. The G_T of this conformal SCMR system exhibits two nulls at misalignment angles of 90° and 270° . Finally, the range of this CSCMR design is shown in Fig. 3.12, and it is similar to the one of standard SCMR.

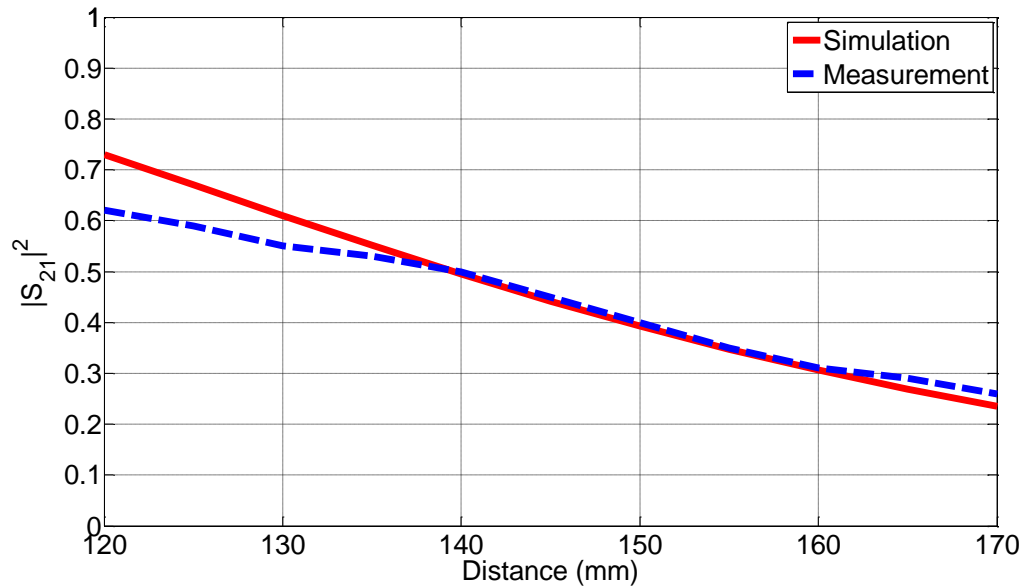


Figure 3.12. G_T of CSCMR vs. distance.

Based on the results of Figs. 3.11(a) and 3.11(b), CSCMR systems exhibit the same variation of $|S_{21}|^2$ for angular azimuth and elevation misalignment. This was also the case for SCMR systems, as shown in Figs. 3.7(a) and 3.7(b). Comparing the results for the CSCMR and SCMR systems, it can be concluded that they both have similar

variations except for the G_T from 120° to 240° of misalignment. Specifically, the standard SCMR system exhibits a G_T of only 30% to 40% for 120° to 240° of misalignment whereas the CSCMR system exhibits a G_T above 50% in the same range of misalignment angles. Also, it is observed by comparing Figs. 3.11(a) and 3.11(b) with Figs. 3.7(a) and 3.7(b) that the G_T of the CSCMR system raises back to its maximum value between its nulls whereas the G_T of the standard SCMR drops to a significantly lower value between its nulls. Therefore, the CSCMR system exhibits significantly less misalignment sensitivity and better performance compared to standard SCMR.

3.2 Misalignment Analysis of Proposed Misalignment Insensitive SCMR System

3.2.1 3-D SCMR

A novel SCMR system is proposed here, and it is shown in Fig. 3.13. In this SCMR system, the TX and RX resonator elements as well as the source and load elements are 3-D loops consisting of two continuous connected orthogonal loops. The TX and RX systems in 3-D SCMR systems are identical. Therefore, one of them is shown in Fig. 3.13. The source (or load) loop, the TX (or RX) resonator and the capacitor connected at the port of the TX (or RX) resonator are shown in Fig. 3.13. The input power (or load) is connected to the source (or load) loop, as shown in Fig. 3.13. The source (or load) loop has the same geometry as the TX (or RX) resonator. In fact, the source (or load) loop is a scaled version of the TX (or RX) resonator. The source (or load) loop and the TX (or RX) resonator loop are isolated from each other (i.e., they are not directly connected) and each of them is constructed by a single continuous copper wire that is bend accordingly to provide the 3-D geometry shown in Fig. 3.13. Also, each of

these 3-D loops consists of two orthogonal loops connected in series. The 3-D TX and RX resonator loops are designed so that they exhibit their highest Q -factor at the frequency of operation. Capacitors are connected at their feed point to resonate them at the operating frequency. In addition, the source and load loops are concentrically embedded into the TX and RX resonators, respectively. This type of system has a spherical symmetry and therefore, it is expected to be less sensitive to misalignment. The angular misalignment rotations are performed as follows: for angular azimuth rotation, the RX system rotates in the xy -plane around the z -axis, while the TX system is fixed; for angular elevation rotation, the RX system is rotated in the yz -plane around x -axis, while the TX system is fixed.

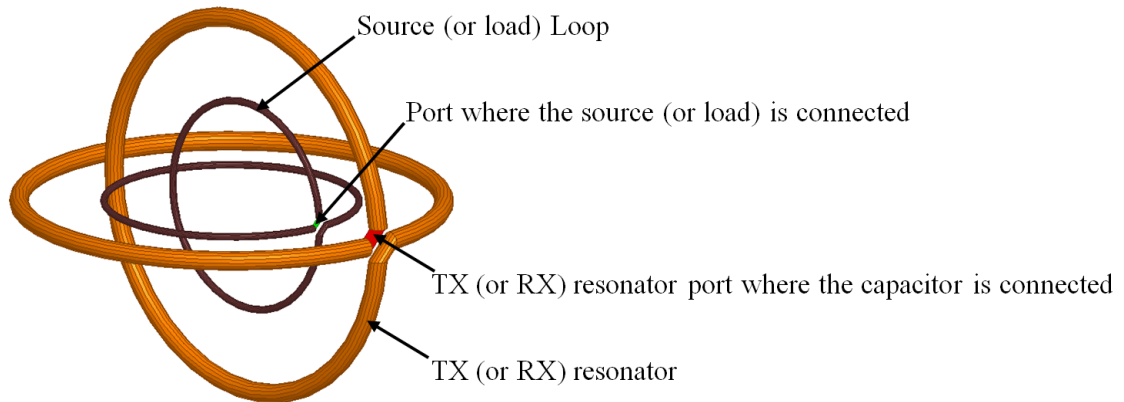


Figure 3.13. 3-D SCMR TX or RX system.

A 3-D SCMR system is designed (see Fig. 3.14) and its geometric specifications are described in what follows. The TX and RX resonators are comprised of two connected orthogonal loops with the following radii: the radius of the outer loop is $r_1 = 50$ mm, the radius of the inner loop is $r_2 = 45$ mm, and the cross-sectional radius of both loops is $r_c = 2.2$ mm. The source and load elements are comprised of two connected orthogonal loops with the following radii: the radius of the outer loop is $r_3 = 30$ mm, the

radius of the inner loop is $r_4 = 25$ mm, and the cross-sectional radius of both loops is $r_c = 0.8$ mm. The distance between the TX and RX systems is $\ell_2 = 120$ mm and it is defined as the distance from the center of the TX resonator to the center of the RX resonator. The frequency of operation is 80.2 MHz. Each of the TX and RX resonators are connected to a 10 pF capacitor. This capacitance value was found by simulation analysis so that maximum G_T is achieved by this system.

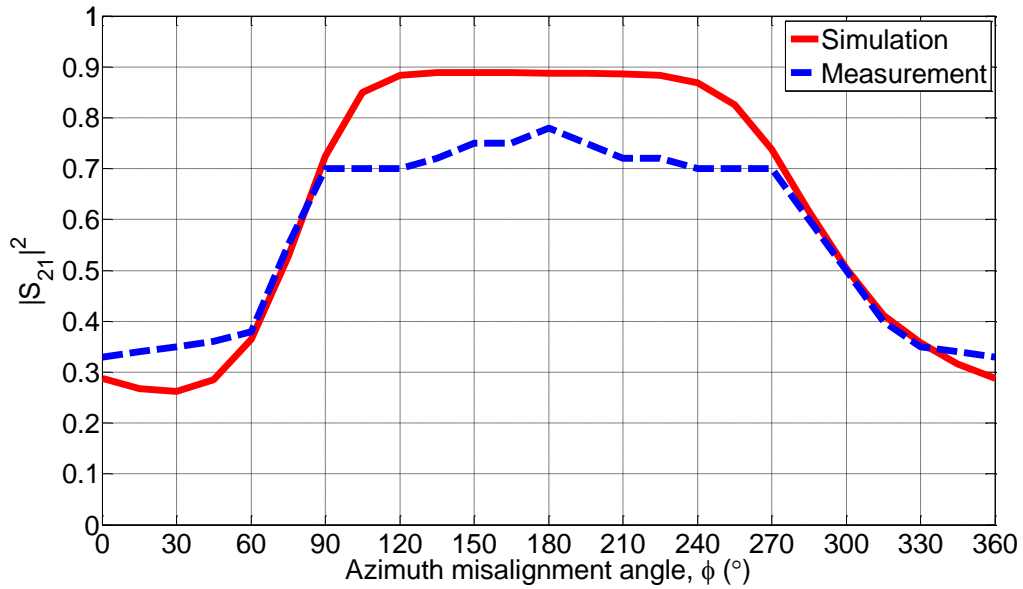


Figure 3.14. Prototype of 3-D SCMR system.

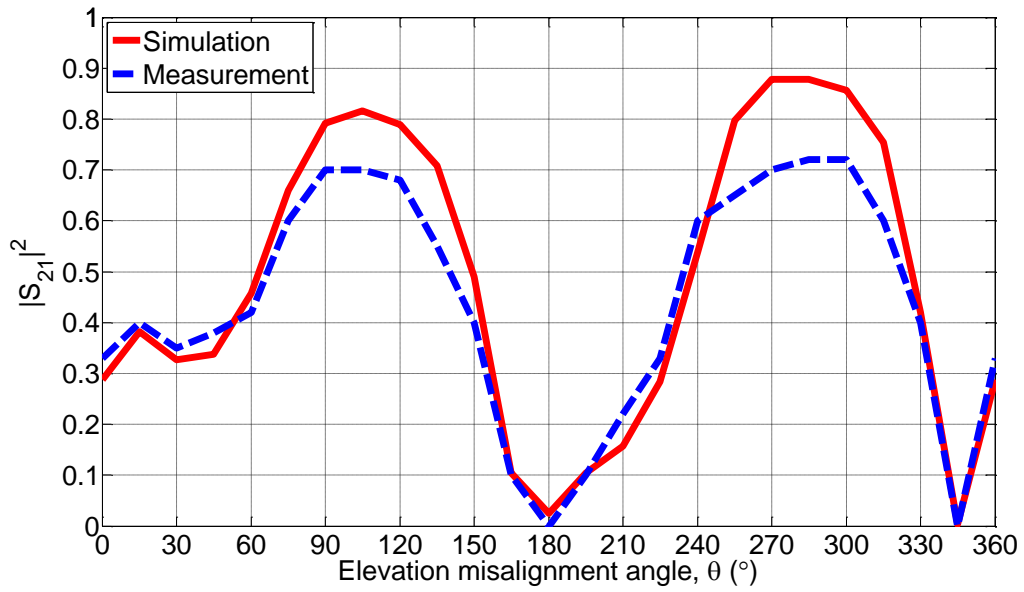
Fig. 3.15 illustrates the G_T of this 3-D SCMR system under different misalignment conditions. Specifically, Fig. 3.15(a) shows that for azimuth misalignment, the G_T of this 3-D SCMR system does not exhibit any nulls and it remains above 30% for the full range of 360° of azimuth misalignment. This is a clear advantage of this system over standard SCMR and CSCMR systems. However, Fig. 3.15(b) shows that for elevation misalignment, the G_T of this 3-D SCMR system exhibits two nulls at 180° and 345° and similar variation with the G_T of CSCMR system shown in Fig. 3.11(b). Some of

the difference between measurements and simulations can be attributed to the fact that prototypes were manually constructed and therefore, they are not exactly the same with simulation models. Especially, these 3-D loops are difficult to construct by hand and generate perfectly circular geometries. Also, the capacitors used in our prototypes have some losses and are not perfect as the capacitors used in the simulation, which contributes a slight drop in the measured G_T compared to the simulated one.

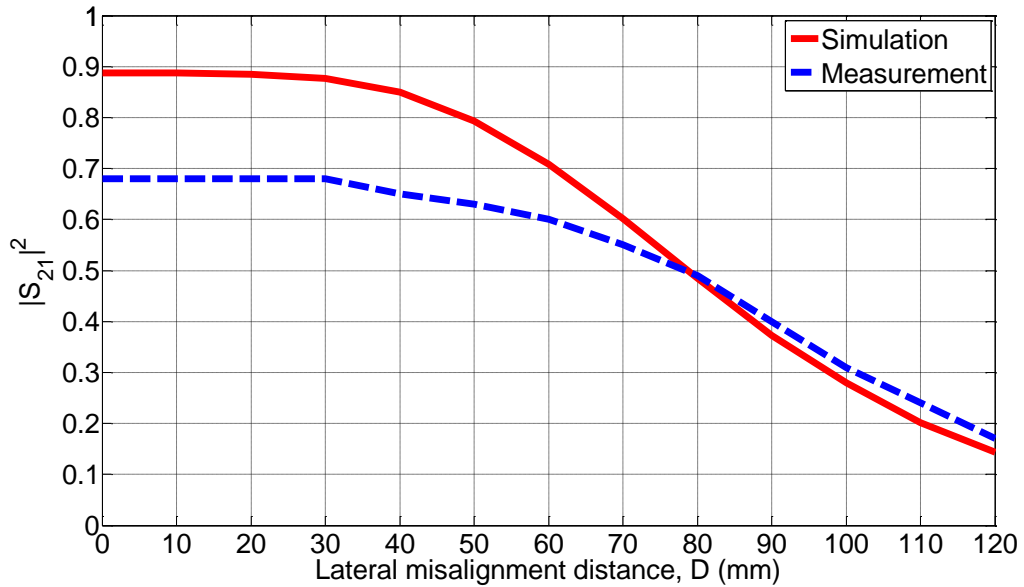
Even though in this case the transmitter and receiver are identical, Fig. 3.15(a) is different from Fig. 3.15(b) because the portions of the 3D loops that are aligned during rotation in the azimuth misalignment are different from the ones in the elevation misalignment. Also, Fig. 3.15(b) is not perfectly symmetric because each 3D loop is not perfectly symmetric. In fact each 3D loop is composed by two 2D loops that are connected in series and certain geometric modifications have to be done to avoid shorting of the 2D loops at the port, which in turn result in non-perfectly symmetric 3D loops.



(a)



(b)



(c)

Figure 3.15. G_T of 3-D SCMR system of Fig. 3.5(c) under different misalignment conditions. (a) Angular azimuth misalignment. (b) Angular elevation misalignment. (c) Lateral misalignment.

Based on the measured data, the angle ranges of this 3-D SCMR system for a $|S_{21}|^2$ level, which is set at 60% of its maximum, are 221° and 168° for azimuth and elevation misalignment, respectively. These angle ranges are less than the corresponding

ones of CSCMR (i.e., 248°). However, the angle ranges of this 3-D SCMR system for a $|S_{21}|^2$ level, which is set at 30% of its maximum, are 360° and 272° for azimuth and elevation misalignment, respectively; therefore, they are larger than the corresponding ones of CSCMR (i.e., 294°) and standard SCMR (i.e., 278°). From Fig. 15(c), it can be seen that the lateral range for a $|S_{21}|^2$ level, which is set at 30% of its maximum, is 102 mm and it is larger than the one (i.e., 92 mm) of CSCMR. This shows that 3-D SCMR is less sensitive to lateral misalignment performance than both standard SCMR and CSCMR.

The range of this 3-D SCMR system is shown in Fig. 3.16. By comparing Fig. 3.16 with Figs. 3.8 and 3.12, it can be seen that 3-D SCMR exhibit longer range than SCMR and CSCMR. Specifically, at a distance of 170 mm the G_T of 3-D SCMR is 30% versus the 20% G_T of both standard SCMR and CSCMR.

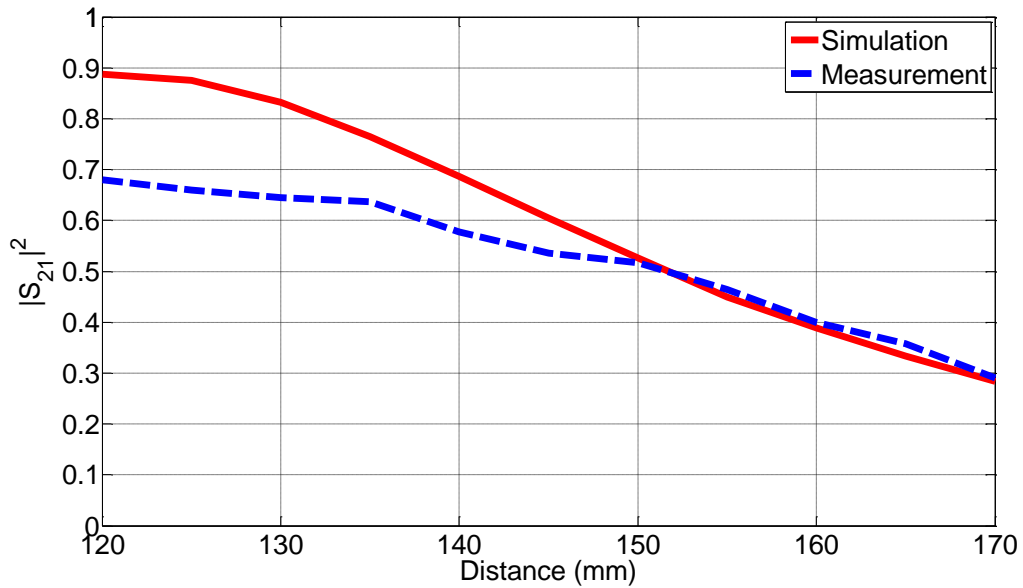


Figure 3.16. G_T of 3-D SCMR vs. distance.

The 3-D SCMR system is less sensitive to misalignment comparing to standard and conformal SCMR systems. Specifically, 3-D SCMR achieves misalignment insensitivity for azimuth angular rotation for the entire 360° of rotation as shown in Fig. 3.15(a). Also, the G_T of the 3-D SCMR system is above 70% for 90° to 270° of azimuth misalignment, whereas the G_T of the standard SCMR is less than 40% for the same range of misalignment. The maximum G_T of standard SCMR, CSCMR and 3-D SCMR are 80%, 75%, and 88% for the angular azimuth misalignment respectively. For angular elevation rotation standard SCMR, CSCMR, and 3-D SCMR systems all exhibit two nulls in the G_T . These nulls are near 90° and 270° for standard SCMR and CSCMR systems, and 180° and 345° for the 3-D SCMR system. The maximum G_T for standard SCMR, CSCMR and 3-D SCMR for the angular elevation misalignment are 80%, 75%, and 86%, respectively.

In order to quantify the SCMR's system efficiency, the operating power gain is used since it includes the effects of the reflection coefficient. The operating power gain is defined as the ratio of power dissipated at the load to the power delivered at the input of the two-port network, which is also the power input at the transmitter coil. The entire SCMR WPT system is considered as a two-port network. In order to better understand the power gain definition, this two-port network with source and load impedance is shown in Fig. 3.17.

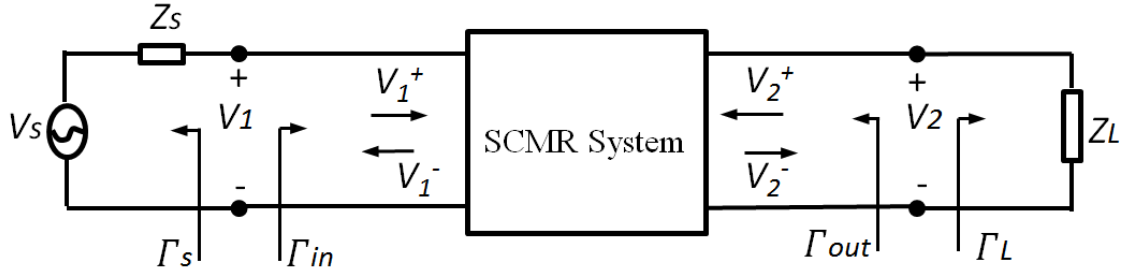


Figure 3.17. A two-port network for SCMR system with source and load impedances.

The operating power gain can be defined in terms of S-parameters per [28] as follows:

$$Gain_o = \frac{P_L}{P_{in}} = \frac{|S_{21}|^2 (1 - |\Gamma_L|^2)}{(1 - |\Gamma_{in}|^2) |1 - S_{22}\Gamma_L|^2} \quad (3.7)$$

where Γ_L is the reflection coefficient at the load,

$$\Gamma_L = \frac{Z_L - Z_0}{Z_L + Z_0} \quad (3.8)$$

and

$$\Gamma_{in} = S_{11} + \frac{S_{12}S_{21}\Gamma_L}{1 - S_{22}\Gamma_L} \quad (3.9)$$

Assuming the SCMR system is terminated to a 50Ω load and according to (3.2), $\Gamma_L = 0$, which in turn according to (3.3) makes $\Gamma_{in} = S_{11}$. In this case, the operating power gain is written as:

$$Gain_o = \frac{|S_{21}|^2}{1 - |S_{11}|^2} \quad (3.10)$$

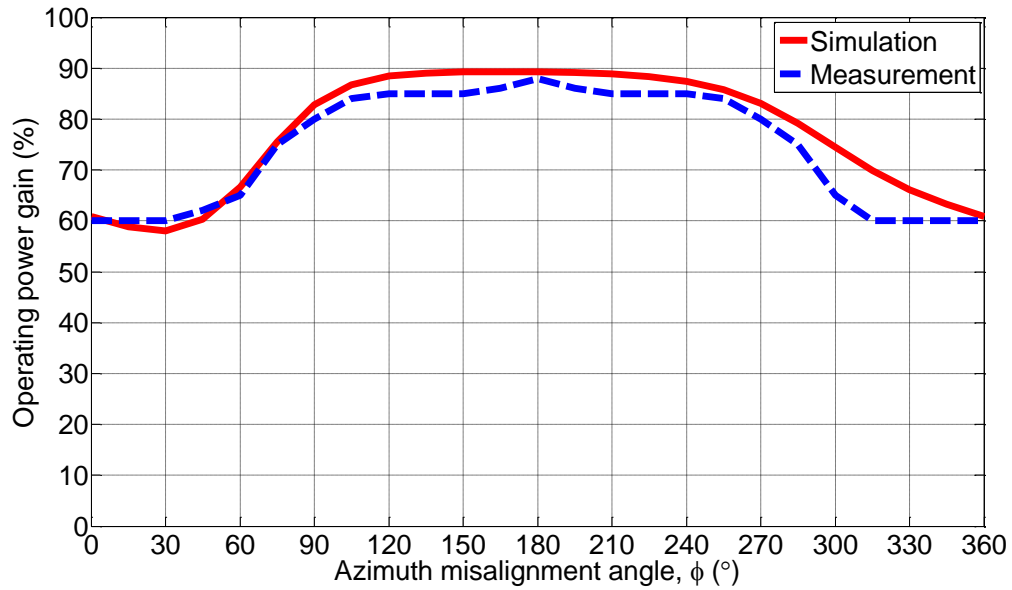


Figure 3.18. Operating power gain of 3-D SCMR.

Fig. 3.18 illustrates the simulated and measured operating power gain based on (3.10) for the 3-D SCMR for the azimuth misalignment case. By comparing Figs. 3.18 and 3.15(a), it can be observed that the operating power gain and the G_T exhibit similar variation versus the azimuth misalignment angle, but the amplitude of the operating gain is larger since it takes into account the reflection coefficient, S_{11} , at the input of the SCMR system. It should be noted that since this efficiency formula is based on a 50Ω load impedance, additional circuit blocks are needed if other load impedances are used.

3.2.2 Hybrid SCMR (HSCMR)

In this section, the previous two models of CSCMR and 3-D SCMR are combined into one system called Hybrid SCMR (HSCMR) as shown in Fig. 3.5(d). Specifically, the receiver is a CSCMR element whereas the transmitter is a 3-D SCMR element. Therefore, since this HSCMR system has a receiver that is conformal, it is easier to implement it in practice than the 3-D SCMR system. Also, this HSCMR system has a transmitter that

exhibits spherical symmetry. The angular misalignment rotations are performed as follows: for angular azimuth rotation, the RX system rotates in the xy -plane around the z -axis, while the TX system is fixed; for angular elevation rotation, the RX system is rotated in the yz -plane around x -axis, while the TX system is fixed.

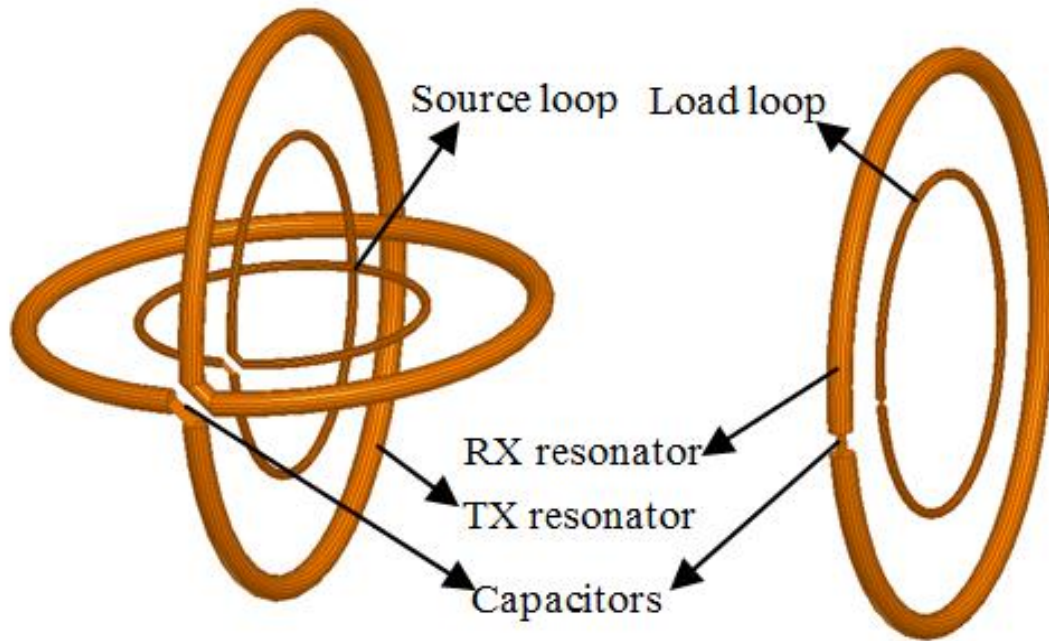
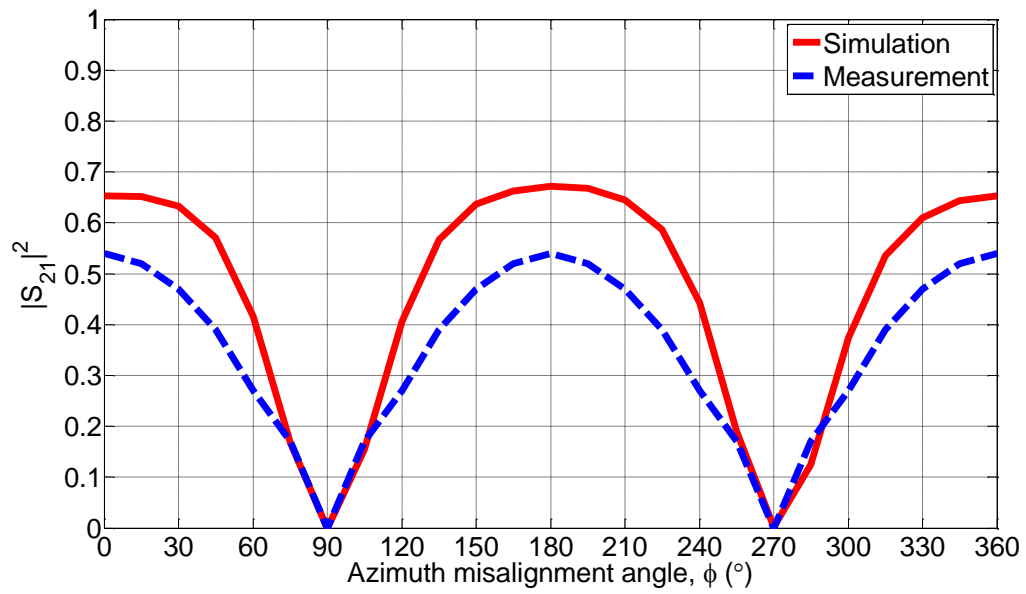


Figure 3.19. Schematic of HSCMR system.

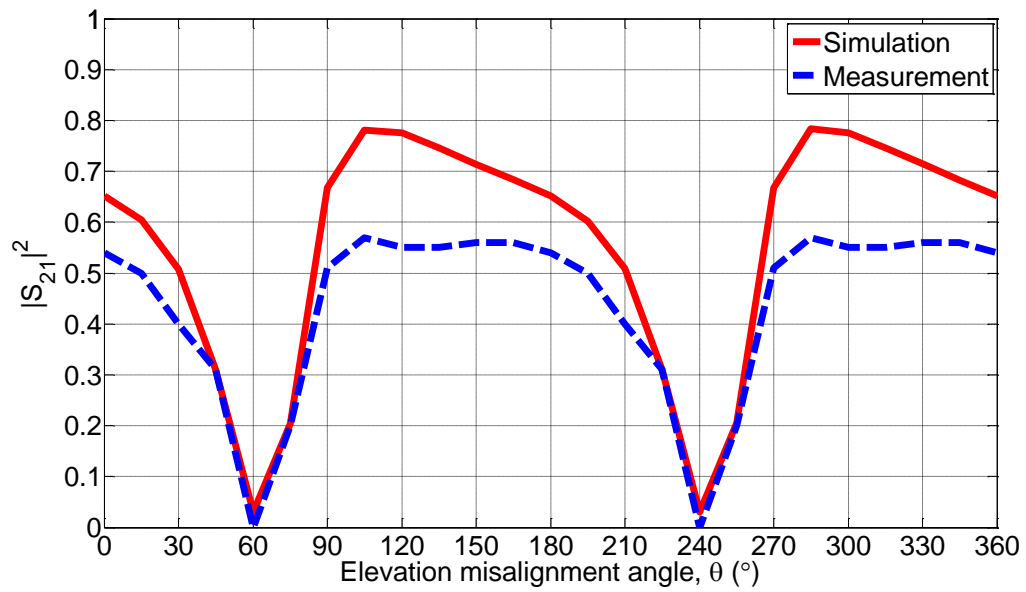
An HSCMR system is designed (see Fig. 3.19) and its geometric specifications are described in what follows. For the TX system's 3-D resonator, the radius of the outer loop is $r_1 = 50$ mm, the radius of the inner loop is $r_2 = 45$ mm, and the cross-sectional radius of both loops is $r_c = 2.2$ mm. The 3-D source element is comprised of two connected orthogonal loops with the following specifications: the radius of its outer loop is $r_3 = 30$ mm, the radius of its inner loop is $r_4 = 25$ mm, and the cross-sectional radius of both loops is $r_c = 0.8$ mm. A 10 pF capacitor is needed for the transmitter. The conformal RX system has the following geometric specifications: the radius of the outside loop is

50 mm with cross-sectional radius of 2.2 mm; the radius of the inside loop is 30 mm with cross-sectional radius of 0.8 mm. A 19.9 pF capacitor is connected on the RX resonator provide the best G_T . The operating frequency of this HSCMR system is 80.2 MHz. The distance between the center of TX and RX systems is 120 mm.

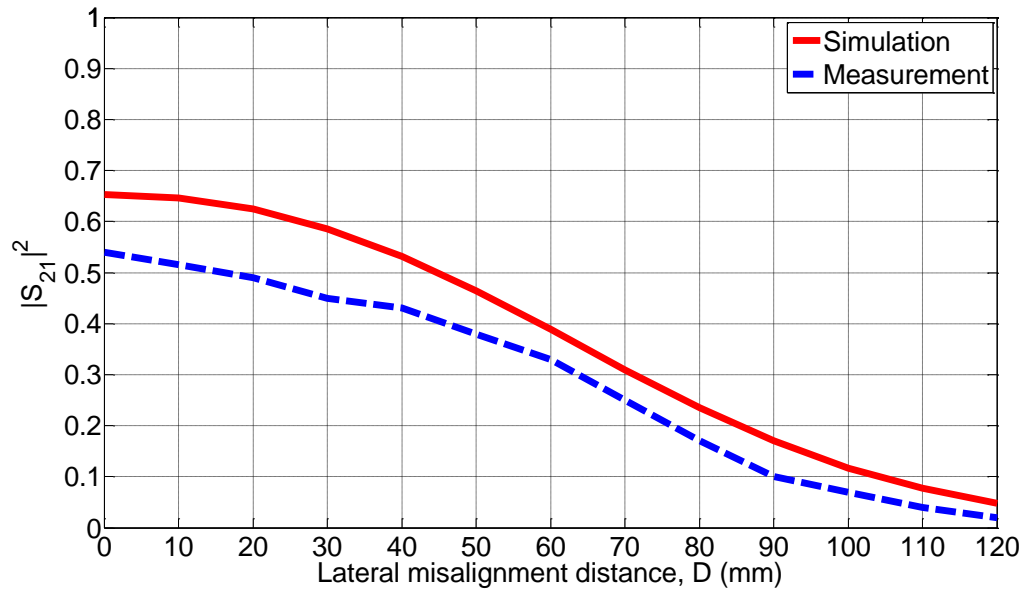
Fig. 3.20 illustrates the G_T of this HSCMR system for different misalignment conditions. Fig. 3.20(a) illustrates that the variation of HSCMR's G_T for azimuth misalignment is similar to the variation of CSCMR shown in Fig. 3.11(a), i.e., the G_T has two nulls at 90° and 270° and it raises to its maximum between the nulls. Fig. 3.20(b) shows that HSCMR's G_T for elevation misalignment has two nulls that are shifted by 30° lower compared to its nulls for azimuth misalignment. This can be useful in case WPT needs to be achieved at a 90° elevation angular misalignment. The misalignment results of HSCMR illustrate that it performs similarly to the conformal SCMR, since they both use the same type of receiver. The only difference is that the nulls of the G_T shift from 90° and 270° for the CSCMR to 60° and 240° for the HSCMR due to the fact that the HSCMR transmitter has two orthogonal loops that can couple with the receiver.



(a)



(b)



(c)

Figure 3.20. G_T of hybrid SCMR system of Fig. 5(d) under different misalignment conditions. (a) Angular azimuth misalignment. (b) Angular elevation misalignment. (c) Lateral misalignment.

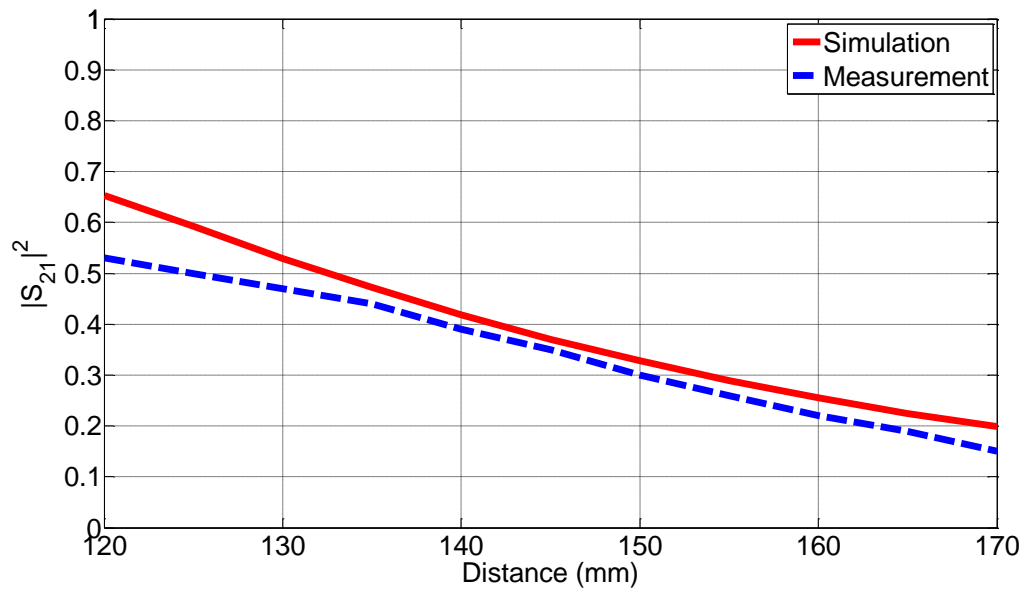


Figure 3.21. G_T of HSCMR vs. distance.

The angle ranges of this HSCMR system for a $|S_{21}|^2$ level, which is set at 60% of its maximum, are 241° and 259° for azimuth and elevation misalignment, respectively. HSCMR angle ranges are similar to the ones of CSCMR (i.e., 248°) but larger than the ones of 3-D SCMR (i.e., 221° and 168°). The angle ranges for a $|S_{21}|^2$ level, which is set at 30% of its maximum, are 290° and 306° for azimuth and elevation misalignment, respectively, which are again similar to the ones of CSCMR (i.e., 294°). Fig. 20(c) illustrates that the lateral range for a $|S_{21}|^2$ level, which is set at 30% of its maximum, is 86 mm, which is smaller than the ones of CSCMR (i.e., 92 mm) and 3-D SCMR (i.e., 102 mm) but larger than the one of standard SCMR (i.e., 78 mm). Fig. 3.21 depicts the G_T of HSCMR versus distance. By comparing Fig. 3.21 with the corresponding Figures for the other WPT systems presented above, it can be concluded that HSCMR's range is less than the one of 3-D SCMR but similar to the one of CSCMR.

3.3 Comparison Discussion

This paper proposed various novel topologies of SCMR systems that are less sensitive to misalignment between TX and RX systems than standard SCMR system. From the results shown above, it can be concluded that CSCMR exhibits less sensitivity to misalignment since its G_T between the angles where the nulls occur increases back to its maximum, whereas for standard SCMR its G_T drops to a significantly lower value between its nulls. This is due to the fact that the source and load loops are embedded concentrically in the TX and RX resonators, respectively. Therefore, when the CSCMR RX system is rotated to 180° of misalignment, its position compared to the TX system is exactly the same as its position for 0° misalignment. On the other hand, standard SCMR

uses a pair of parallel loops at each of the TX and RX systems, which results reduced G_T when the RX is rotated to 180° of misalignment. In addition, 3-D SCMR exhibits no nulls for azimuth misalignment which is a significant improvement over the standard and conformal SCMR. This happens because each of the loops of 3-D SCMR is constructed using two orthogonal loops connected in series; therefore, for any angle of rotation two pairs of loops (one at the TX and one at the RX system) are always coupled. For the elevation rotation, 3-D SCMR exhibits two nulls at 180° and 345° which can be attributed to the cancelation of the magnetic fluxes received by the two orthogonal loops at these two angles. HSCMR performs similarly to CSCMR since they both use the same receiver. The only difference is that the nulls of the G_T shift from 90° and 270° for the CSCMR to 60° and 240° for the HSCMR due to the fact that the HSCMR transmitter has two orthogonal loops that can couple with the receiver.

Table 3.1 summarizes the measured results presented above and compares the performance of the different SCMR systems. The angle misalignment ranges for azimuth and elevation misalignment are calculated based on the angles for which the G_T maintains a value above 60% or 30% of the maximum G_T of each system. It can be seen that all three proposed SCMR systems (i.e., conformal SCMR, 3-D SCMR, and hybrid SCMR) exhibit larger angle misalignment range compared to standard SCMR. In fact, 3-D SCMR exhibits the best performance regarding misalignment since it has no G_T nulls over the entire 360° azimuth rotation. Furthermore, a hybrid SCMR (HSCMR) system was proposed in an effort to provide a WPT system that has a conformal receiver, which maybe more suitable for certain applications. This HSCMR system is also less sensitive to misalignment compared to standard SCMR.

Table 3.1. Comparison of Different SCMR Systems

		Angle Misalignment Range (°) 60%	Angle Misalignment Range (°) 30%	Lateral range (mm) 30%
Standard SCMR	Azimuth	102	278	78
	Elevation	102	278	
Conformal SCMR	Azimuth	248	294	92
	Elevation	248	294	
3-D SCMR	Azimuth	221	360	102
	Elevation	168	272	
Hybrid SCMR	Azimuth	241	290	86
	Elevation	259	306	

CHAPTER 4

CYLINDRICAL MISALIGNMENT INSENSITIVE WIRELESS POWER TRANSFER SYSTEMS

In this chapter, another misalignment insensitive structure is proposed and studied. This is an improvement over the previous design in terms of power transfer efficiency and misalignment insensitivity performance. Section 4.1 illustrates the misalignment sensitivity issue facing all WPT systems. The misalignment performance of conformal SCMR is also included in this section. The proposed cylindrical SCMR system is presented in Section 4.2, which includes two systems based on copper wire and PCB. In Section 4.3, the wearable implementation is discussed and possible wearable applications are presented. Lastly, optimization of this cylindrical SCMR system is shown in Section 4.4.

4.1 Misalignment Sensitivity Background Study

Standard SCMR systems exhibit high sensitivity to angular misalignment, and they have been studied in several papers [17], [24]-[26]. Specifically, in [17] frequency tuning is applied and a nearly constant efficiency at approximately 75% was obtained until the receiver is rotated past 60°. Beyond 60°, the efficiency drops rapidly to zero from 60° to 90° misalignment. In [26], it was shown that the efficiencies vary from 40% to 20% from 0° to 45° misalignment angle, and from 20% to 0 from 45° to 90° misalignment angle. In this section, the misalignment analysis of conformal SCMR (CSCMR) systems is investigated. Conventional CSCMR systems are constructed so that the source and load loops are embedded into the TX and RX resonators, respectively,

which makes the TX and RX elements planar [27], as shown in Fig. 4.1. Also, Fig. 4.1 illustrates the definition of the azimuth misalignment angle for our study. Azimuth misalignment sensitivity examines how the efficiency of an SCMR system changes when the RX element (load loop and RX resonator) rotates around the TX element (source loop and TX resonator) in the xy -plane (i.e., rotates around the z -axis from $\varphi = 0^\circ$ to 360°), while the TX element is fixed. It should be noted that due to the reciprocity theorem [28], the effect of rotating the TX element around the RX element is the same with rotating the RX element around the TX element. In what follows, the azimuth misalignment sensitivities for all the SCMR systems will be examined. All the simulations in this paper were performed using ANSYS HFSS [29] and ANSYS Designer [30]. The load loops of all the designs examined here are connected to 50 ohm loads. All conformal SCMR resonators examined below were designed to resonate at the frequency where their Q-factor is maximum, which was accomplished by using analytical equations and simulations. All the SCMR systems presented here were designed to operate at the 27.12 MHz ISM band.

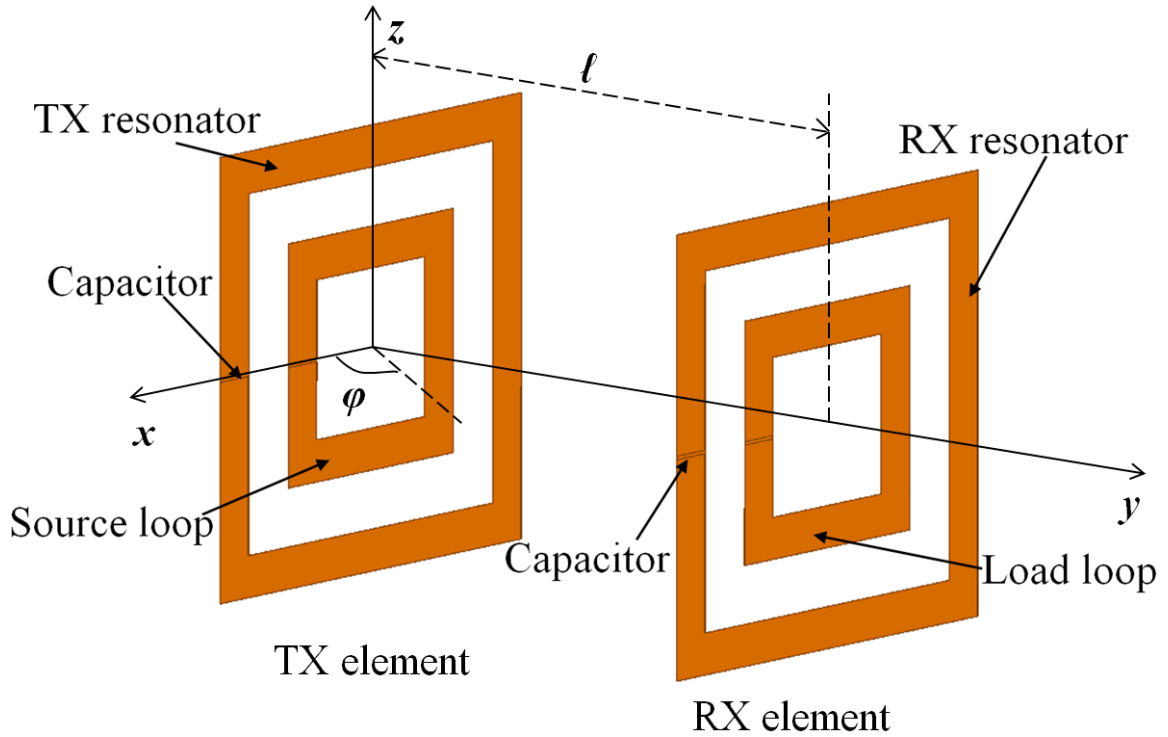


Figure 4.1. SCMR system illustrating azimuth angular misalignment.

In order to quantify SCMR system power transfer efficiency, the transducer power gain is used since it accounts for both source and load mismatches. The transducer power gain is defined as the ratio of power delivered to the load to the power available from the source. The entire SCMR WPT system is considered as a two-port network. In order to better understand the power gain definition, this two-port network with source and load impedance is shown in Fig. 4.2.

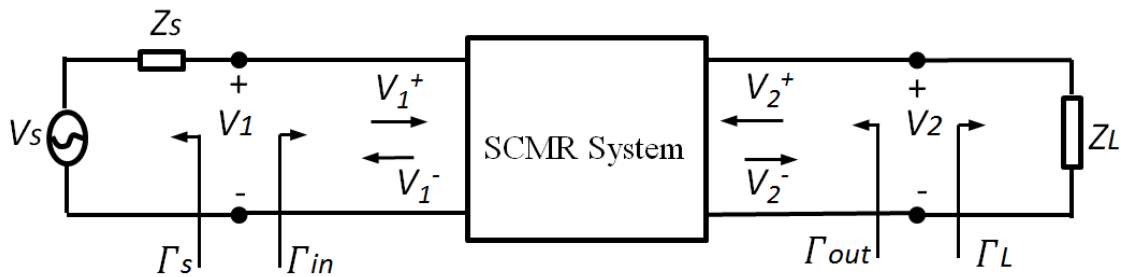


Figure 4.2. A two-port network for SCMR system with source and load impedance.

The transducer power gain can be defined in terms of S-parameters per [31] as follows:

$$G_T = \frac{P_L}{P_{avs}} = \frac{|S_{21}|^2 (1 - |\Gamma_s|^2)(1 - |\Gamma_L|^2)}{|1 - \Gamma_s \Gamma_{in}|^2 |1 - S_{22} \Gamma_L|^2} \quad (4.1)$$

where P_L is the power delivered to the load, and P_{avs} is the power available from the source. With reference to Fig. 4, the reflection coefficient seen looking toward the source is:

$$\Gamma_s = \frac{Z_s - Z_0}{Z_s + Z_0} \quad (4.2)$$

while the reflection coefficient seen looking toward the load is:

$$\Gamma_L = \frac{Z_L - Z_0}{Z_L + Z_0} \quad (4.3)$$

where Z_0 is the characteristic impedance reference for the scattering parameters of the two-port network. The mismatch corresponding to the input impedance of the terminated two-port network is given by the reflection coefficient Γ_{in} , and it is defined as

$$\Gamma_{in} = S_{11} + \frac{S_{12} S_{21} \Gamma_L}{1 - S_{22} \Gamma_L} \quad (4.4)$$

We assume in all our designs that the source and load impedances are 50 Ω , which, according to (4.2) and (4.3), makes $\Gamma_s = \Gamma_L = 0$, and reduces (3.1) to $G_T = |S_{21}|^2$. Therefore, in this paper, the power transfer efficiency, η , of all our designs is equal to G_T and it is defined as

$$\eta = |S_{21}|^2 \quad (4.5)$$

The efficiency of our prototypes is measured using a vector network analyzer and it is based on the S-parameters. Specifically, ports 1 and 2 of the network analyzer are connected to the transmitter and receiver, respectively, and the S-parameters are measured. Then, the data of the measured efficiency is calculated by directly programming the equation $|S_{21}|^2$ on the network analyzer.

In a conventional CSCMR system, the source loop and load loop are embedded into the TX and RX resonators, respectively. Therefore, the source loop is coplanar with the TX resonator and the load loop is coplanar with the RX resonator (see Fig. 4.1). This topology is completely planar and saves a lot of space in practical implementations, whereas standard SCMR requires the source loop and TX resonator to be separated, as well as the RX resonator and load loop. For standard SCMR systems, the TX and RX resonators must be placed between the source and load loops which makes their performance very sensitive to misalignment, as was discussed in [21]. The conventional CSCMR elements can be either circular or rectangular. All our designs in this paper use rectangular elements.

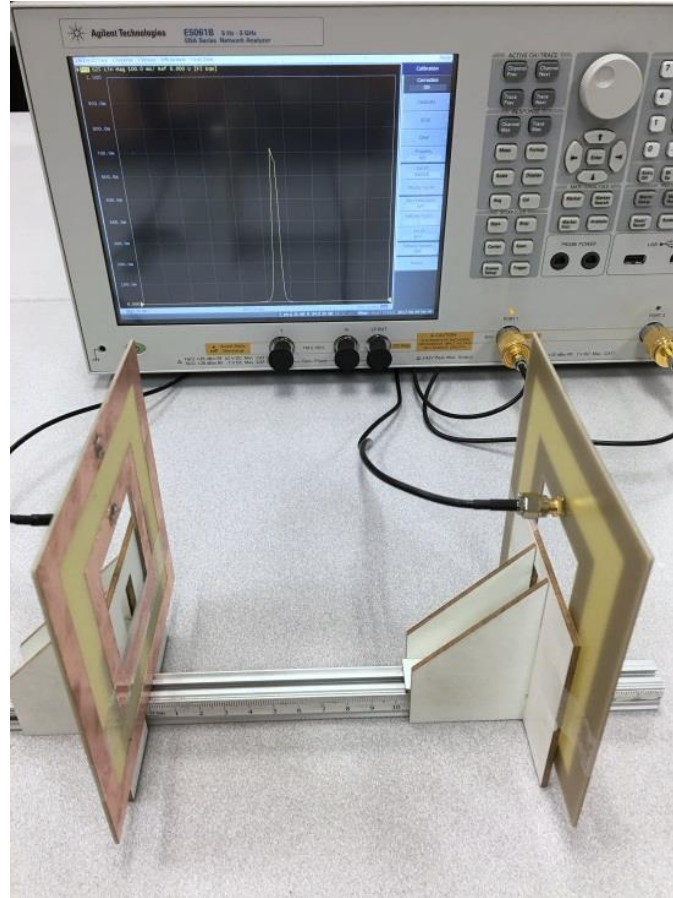


Figure 4.3. Measurement setup of conventional conformal SCMR for 180° of misalignment.

A conventional conformal SCMR system is designed (see Fig. 4.3) under the design guidelines presented earlier with the following specifications. The TX and RX resonators (outside loops) are squares with lengths of 115 mm. The source and load loops are squares with lengths of 57.5 mm (half the size of the resonators). The trace of all the square loops is 12 mm wide and 0.035 mm thick copper. The distance between the TX and RX elements is 150 mm, which was optimized through simulations. Since the TX and RX elements are identical in this case, the Q-factors of both elements are also the same. As shown in Fig. 4.4, this system's Q-factor naturally exhibits its maximum at

27.12 MHz. The capacitors used on both resonators are 139 pF. The operating frequency of this system is 27.12 MHz.

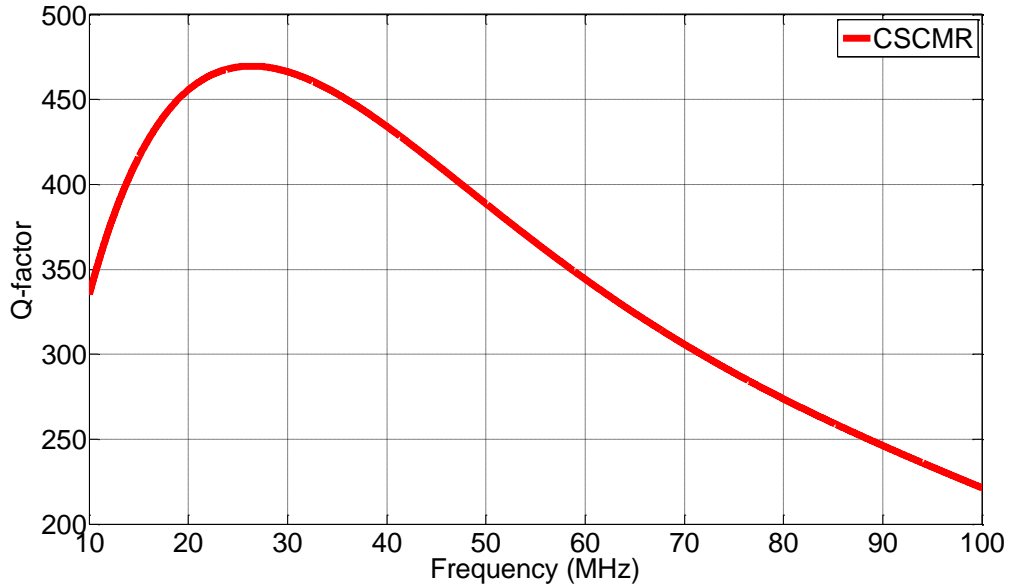


Figure 4.4. Simulated Q-factor of elements of conventional CSCMR system.

Fig. 4.5 plots the efficiency of this conventional CSCMR system versus the azimuth misalignment angle between the transmitter and receiver. It shows that the efficiency stays approximately 70% for misalignment angles of 0° to 60° , 120° to 240° and 300° to 360° . Also, since no magnetic flux can be coupled when the transmitter is perpendicular to the receiver, the efficiency drops from 70% to 0% from 60° to 90° , 120° to 90° , 240° to 270° , and 300° to 270° . Our goal in this chapter, is to develop SCMR systems that do not exhibit nulls in their efficiency for any angle of azimuth misalignment. These designs will be presented in the following sections.

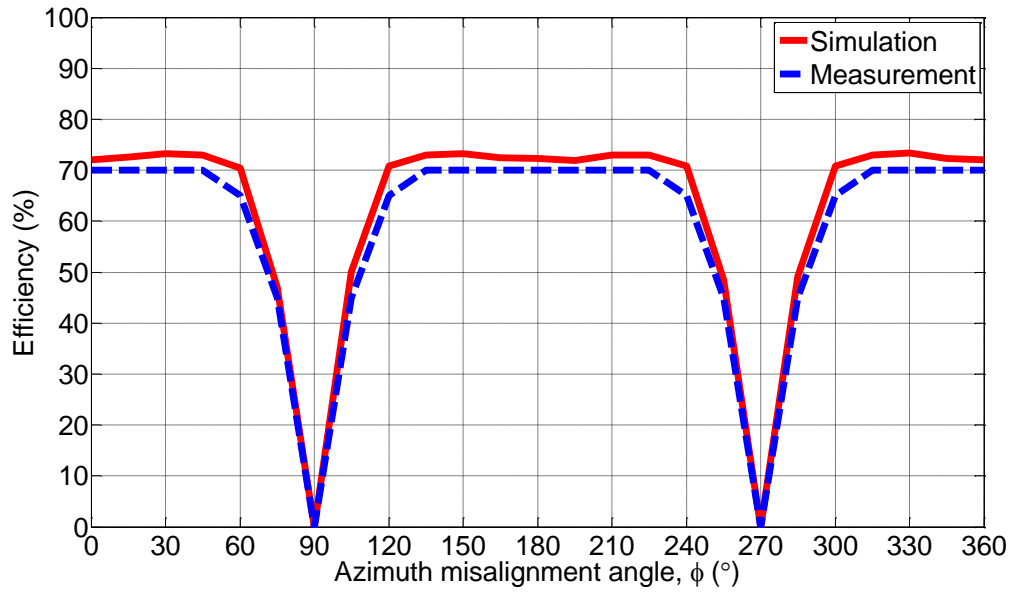


Figure 4.5. Misalignment results of conventional conformal SCMR.

4.2 Cylindrical Misalignment Insensitive SCMR system

4.2.1 Cylindrical SCMR based on Wire Elements

A new SCMR system is proposed here, and it is shown in Fig. 4.6. In this system, the TX element is a 3-D cylindrical wire structure (see Fig. 4.6) and it is proposed for the first time here. Also, this system uses a receiver with conventional CSCMR elements (see Fig. 4.6). The source loop and TX resonator are designed so that they can wrap around a cylinder in order to create cylindrical symmetry for the transmitter thereby providing constant efficiency for the entire 360° of angular misalignment without any nulls. The rotation angle, which is illustrated in Fig. 4.6, is the angle spanned by the cylindrical source and TX resonator elements. The misalignment setup starts out at 0° when the conformal RX element is facing the gap of the TX element, as shown in Fig. 4.6. The misalignment rotation from 0° to 360° is defined as the RX element rotating around the

TX element counterclockwise while keeping the same distance, as illustrated in Fig. 4.6 with the rotation direction arrow.

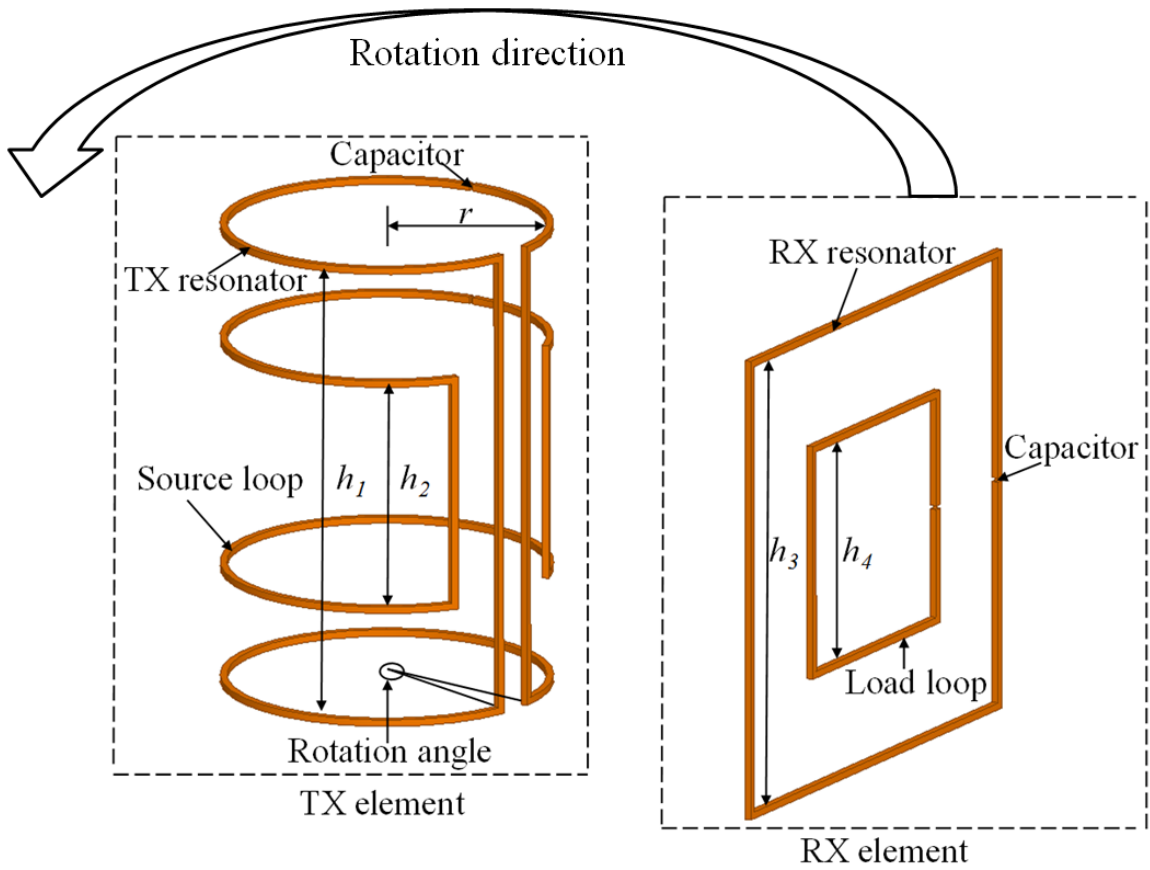


Figure 4.6. Schematic of proposed cylindrical SCMR based on wire elements.

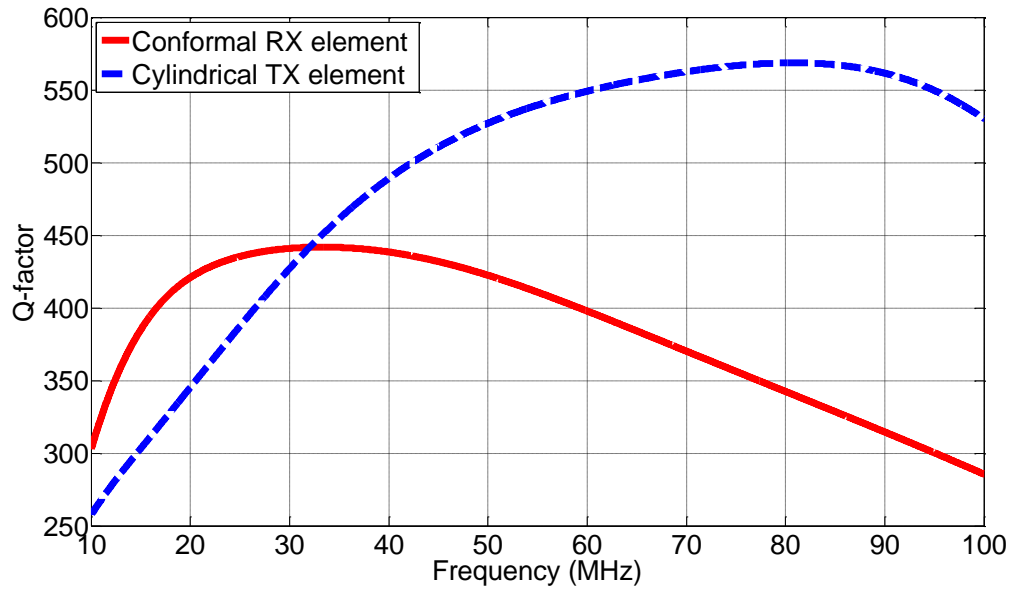


Figure 4.7. Simulated Q-factor of elements of proposed cylindrical SCMR system based on wire elements.

It should be pointed out, that the geometries of the cylindrical elements are kept consistent with the geometry of the CSCMR design in terms of the heights of the source loop and TX resonator. This was done in order to have a fair comparison among all the designs, and to ensure that geometry differences do not contribute to differences in efficiency. Different geometrical parameters, such as height, radius and cross-sectional radius of the cylindrical element can be optimized and their effect on the WPT performance can be studied. However, the main scope of this paper is to prove the misalignment insensitivity and high efficiency of this design. Therefore, the optimization of this design will be examined by our future work and in this paper, the parameters remain consistent for fair comparisons of the different systems. Fig. 4.7 illustrates the simulated Q-factors of the TX and RX elements of this system. The Q-factor of the conformal RX element exhibits its maximum at the desired frequency, but the cylindrical

TX element does not. This is expected, since the geometries of the cylindrical elements are different from the geometries of the conformal elements.

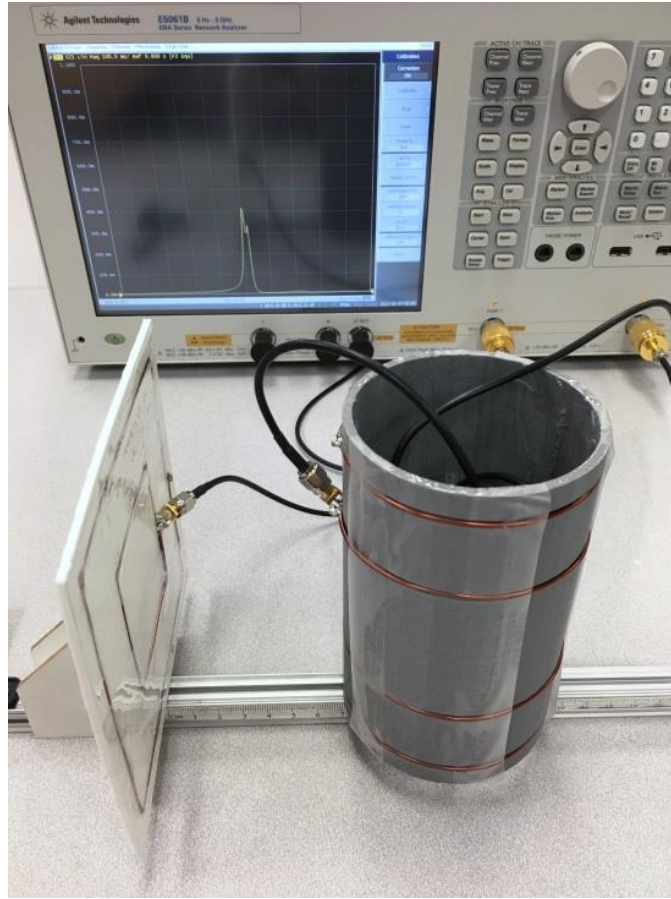


Figure 4.8. Measurement setup of proposed cylindrical SCMR based on wire elements for 180° of misalignment.

A prototype of the proposed cylindrical SCMR based on copper wire is shown in Fig. 4.8. The radius of the cylindrical elements is $r = 40$ mm. The height of the TX resonator is $h_1 = 115$ mm. The height of the source loop is $h_2 = 57.5$ mm (half the size of the resonator). The cross-sectional radius of the copper wire is 1.7 mm. The rotation angle of the TX resonator is 345° . Our simulation analysis found that when the rotation angle of the source loop is equal to $8/9$ of the TX resonator (which is 306.7°), maximum efficiency is achieved. Squared structures are used for the RX element and they are made

using the same wire as the TX element with a cross-sectional radius of 1.7 mm. The length of the resonator is $h_3 = 115$ mm and the length of the load loop is $h_4 = 57.5$ mm (half the size of the resonator). The distance between the outer surface of TX elements and RX elements is 70 mm. The capacitors used on the TX and RX resonators are 82 pF and 100 pF, respectively. The operating frequency for this system is 27.12 MHz.

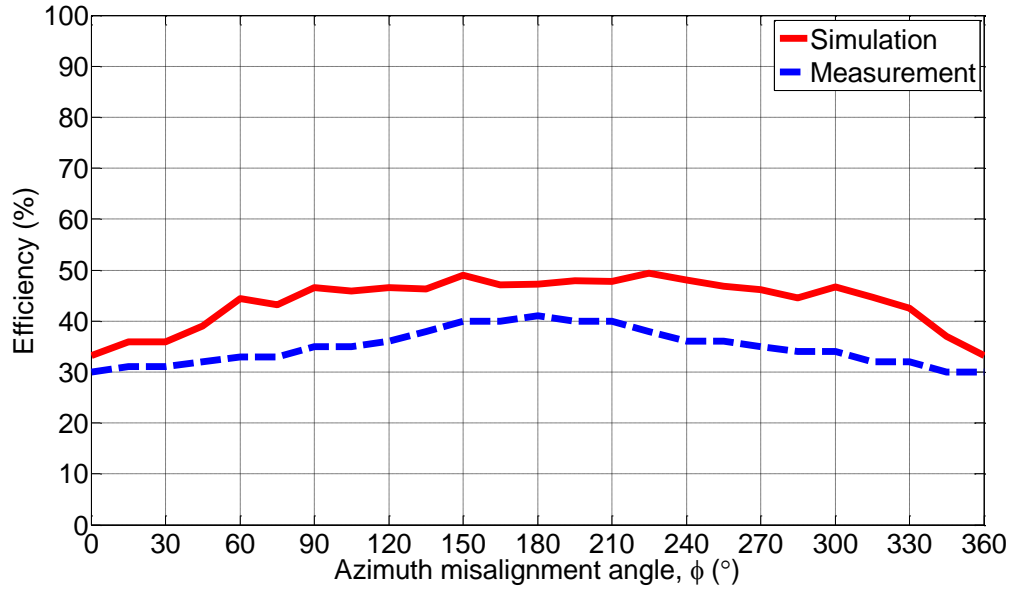
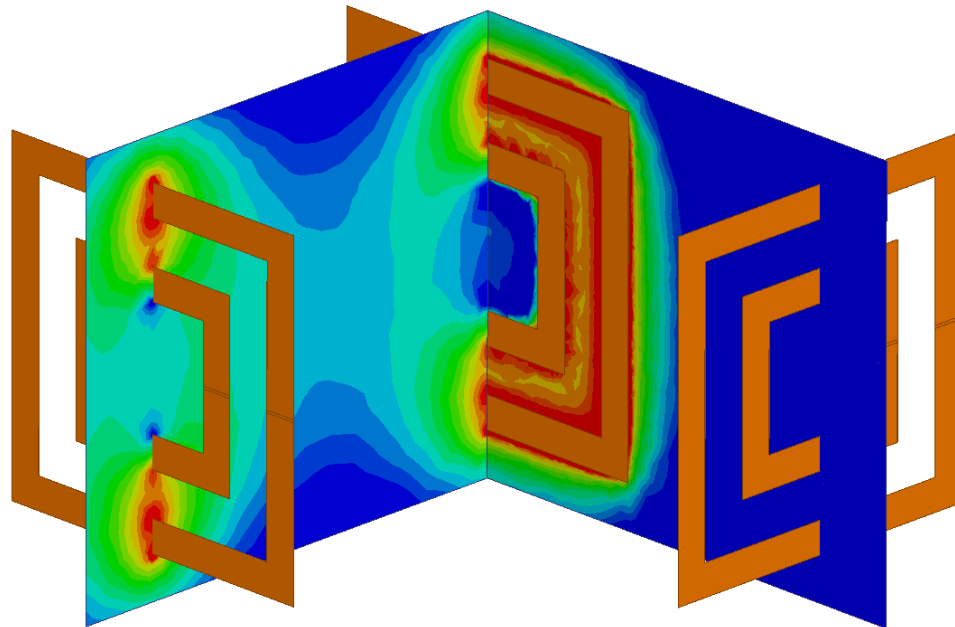


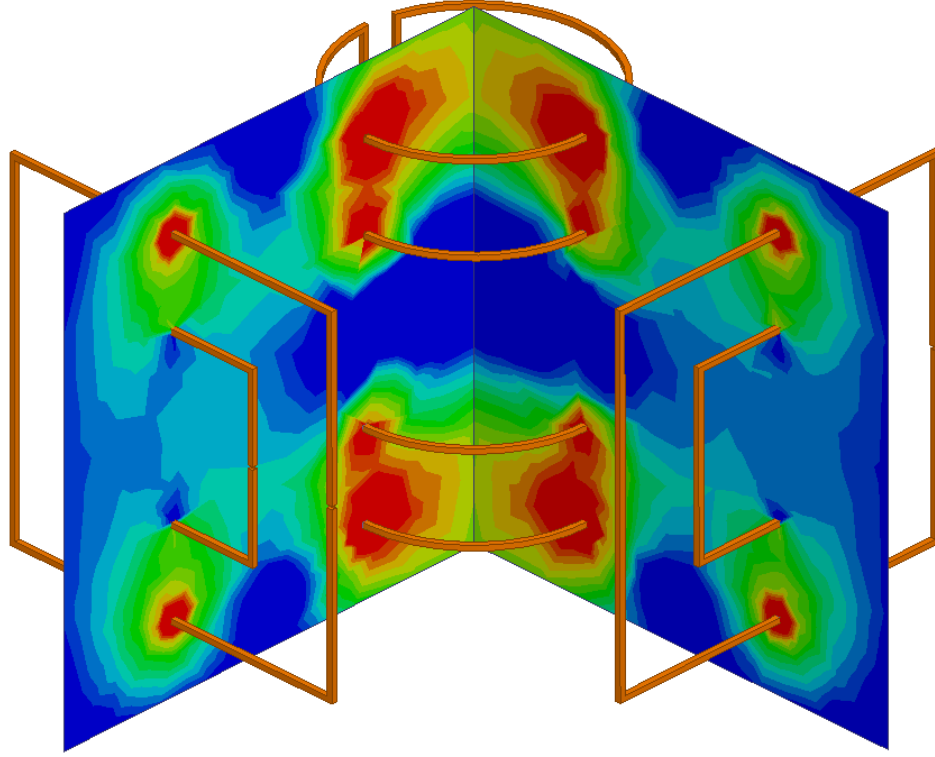
Figure 4.9. Misalignment results of proposed cylindrical SCMR based on wire elements.

Fig. 4.9 illustrates the efficiency of the proposed cylindrical SCMR system for 360° of azimuth misalignment. It can be seen that the efficiency varies from 30% to 40% throughout the 360° misalignment rotation, also it exhibits no null for any angle, which solves the misalignment problem of CSCMR described above. This happens, because the proposed cylindrical SCMR TX elements generate a magnetic field that is symmetric around these elements. On the contrary, conventional CSCMR TX elements generate a magnetic field that has nulls at certain locations around these elements (at these null locations the conventional CSCMR TX and RX elements cannot couple yielding zero

WPT efficiency). This is confirmed in Fig. 4.10 that compares the magnetic field distributions of conventional CSCMR and proposed cylindrical SCMR systems. Fig. 4.10 shows that in a conventional CSCMR system there is no coupling when the RX element is positioned perpendicularly to the TX element whereas in a proposed cylindrical SCMR system, there is coupling between the cylindrical TX element and the RX element for approximately 360° of azimuth misalignment. The slight difference between simulations and measurements in Fig. 4.9 can be attributed to capacitor losses. In the simulations capacitors are ideal, whereas in practice capacitors exhibit some loss. In our measurement setup, non-magnetic, high-Q, low ESR (equivalent series resistance) ceramic capacitors are used with Q-factor above 1000 at our operating frequency of 27.12 MHz. Even though high-Q capacitors are used, they still exhibit small loss and this is the reason that the simulated and measured results are slightly different. This was also explained in [27].



(a)



(b)

Figure 4.10. Magnetic field generated by (a) conventional CSCMR, and (b) proposed cylindrical SCMR.

Fig. 4.9 also shows that the efficiency of the proposed cylindrical SCMR system is smaller than the efficiency of the conventional CSCMR system (see Fig. 4.5) for most azimuth misalignment angles. This occurs because the copper wire that is used has small cross-sectional radius. According to [28],

$$R = \frac{l}{P} R_s = \frac{l}{P} \sqrt{\frac{\omega \mu_0}{2\sigma}} \quad (4.6)$$

where R is the DC resistance of the copper loop, l is the length of the copper wire, P is the perimeter of the cross section of the wire, R_s is the conductor surface resistance, ω is the angular frequency, μ_0 is the permeability of free space, and σ is the conductivity of the metal. According to (4.6), the dc resistance of the cylindrical system based on copper

wire is 0.5Ω . Given that l doesn't change once the geometry of the model is decided and other parameters are all constant, the only parameter that affects the DC resistance is P , which in turn makes the cross-sectional radius of the copper wire the determining factor for R . The smaller the radius is, the higher the resistance of the loop, thereby the lower the efficiency. This is validated by comparing the simulated efficiency of three proposed cylindrical SCMR systems constructed by copper wire with different cross-sectional radii in Fig. 4.11. It can be concluded from Fig. 4.11, as expected, that the thicker the wire is, the higher the efficiency. Furthermore, thicker wire makes the gap between the edges of the cylinders smaller, which in turn results in higher starting and finishing efficiencies when rotating. However, given the difficulty in bending thick copper wire, it was not possible for us to manually manufacture the prototype with thicker copper wire and maintain the dimensional accuracy of the prototype compared to the simulated model.

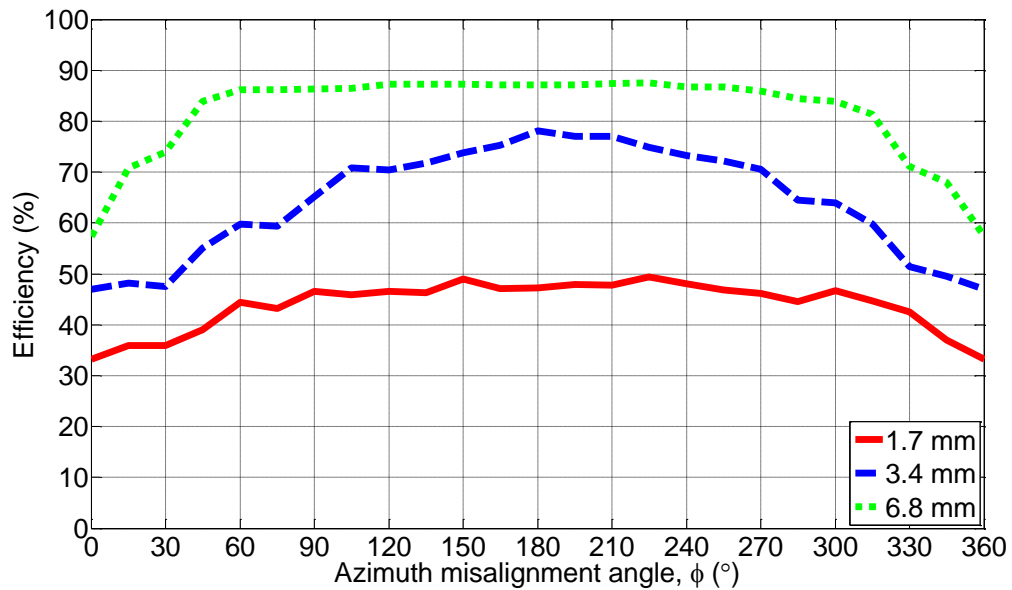


Figure 4.11. Simulated results of three proposed cylindrical SCMR systems based on wire elements with different cross-sectional radii.

4.2.2 Cylindrical SCMR with Flexible PCB

In this section, an improved design of proposed cylindrical SCMR is discussed, and it is shown in Fig. 4.12. This system uses flexible PCBs to construct the cylindrical elements of the transmitter instead of wires, which were used in the previous section. The flexible PCB consists of a bendable polyethylene (PTFE) substrate laminated with 0.035 mm thick copper. By using this material, the cylindrical elements can be easily fabricated by producing the flexible PCB to the desired size and shape, then wrapping it around a cylinder base made by a 3-D printer. This method does not only simplify our manufacturing process, but also generates a prototype that is accurately made and has almost the same geometry with the simulation model. As shown in Fig. 15, the simulated Q-factors of the elements of the flexible PCB system are similar to the ones of the copper wire system, where the Q-factor of the conformal RX element naturally exhibits its maximum at 27.12 MHz and the Q-factor of the cylindrical element does not. The position demonstrated in Fig. 4.12 is considered 0° misalignment, where the gap of the TX element is facing the RX element. The process of misalignment rotation from 0° to 360° is defined as the RX element rotating around the TX element counterclockwise while keeping the same distance, as illustrated in Fig. 4.12 with the rotation direction arrow.

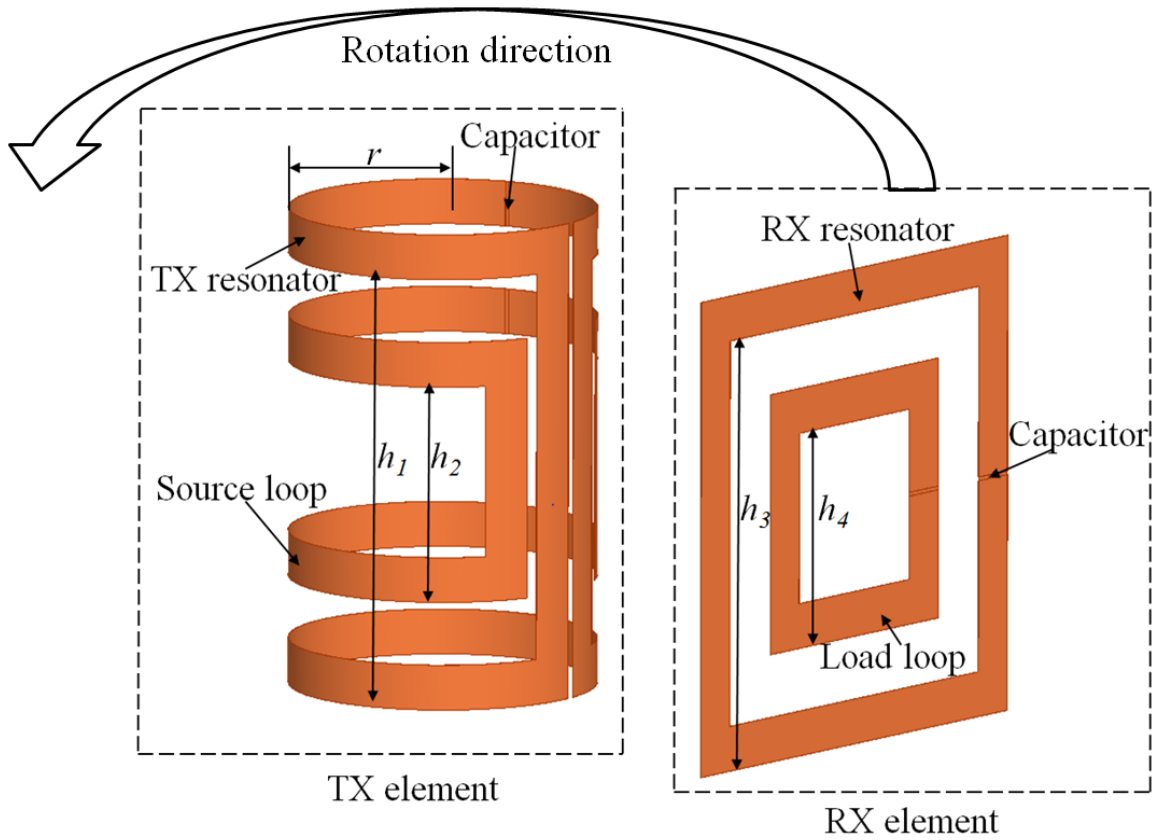


Figure 4.12. Schematic of proposed cylindrical SCMR based on flexible PCB.

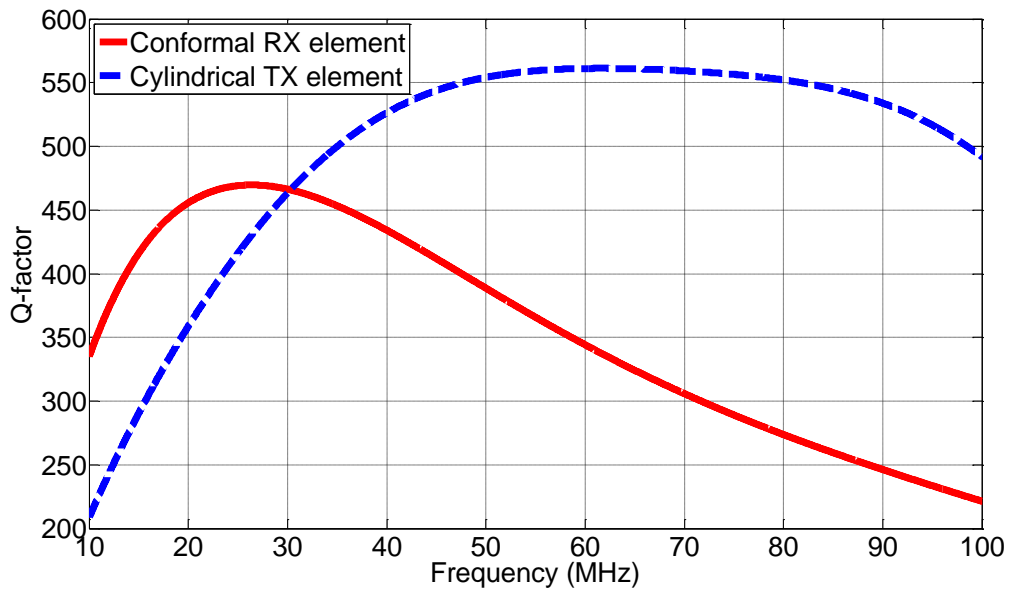


Figure 4.13. Simulated Q-factor of elements of proposed cylindrical SCMR system with flexible PCB.

A flexible PCB cylindrical SCMR prototype is illustrated in Fig. 4.14 with the radii presented below. The radius of the cylindrical elements is $r = 40$ mm. The height of the TX resonator and source loop is $h_1 = 115$ mm and $h_2 = 57.5$ mm (half the size of the resonator). The rotation angle of the TX resonator is 340° and the rotation angle of the source loop is set as $7/8$ of the TX resonator, i.e., 297.5° . These rotation angles were determined for optimal performance through simulation analysis. The squared RX elements have $h_3 = 115$ mm length for the resonator and $h_4 = 57.5$ mm (half the size of the resonator) length for the load loop. The flexible PCB used is 12 mm wide. The distance between the outer surface of TX elements and RX elements is 70 mm. The capacitors for the TX and RX resonators are 120 pF and 139 pF, respectively. The operating frequency is 27.12 MHz.

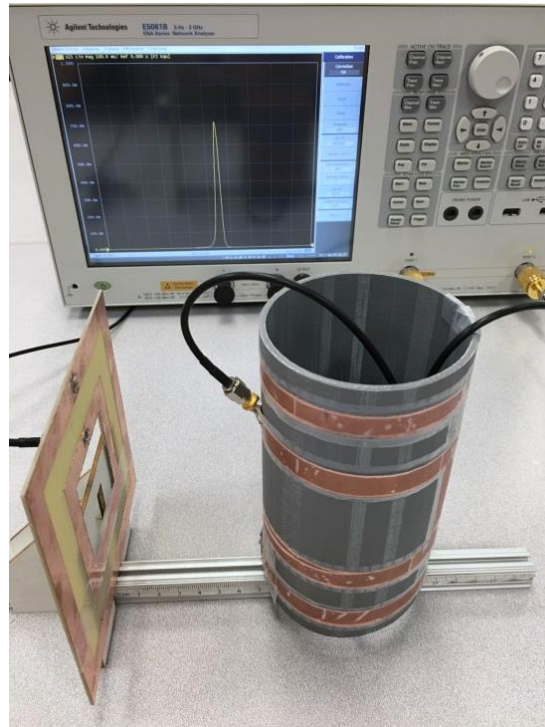


Figure 4.14. Measurement setup of proposed cylindrical SCMR with flexible PCB for 180° of misalignment.

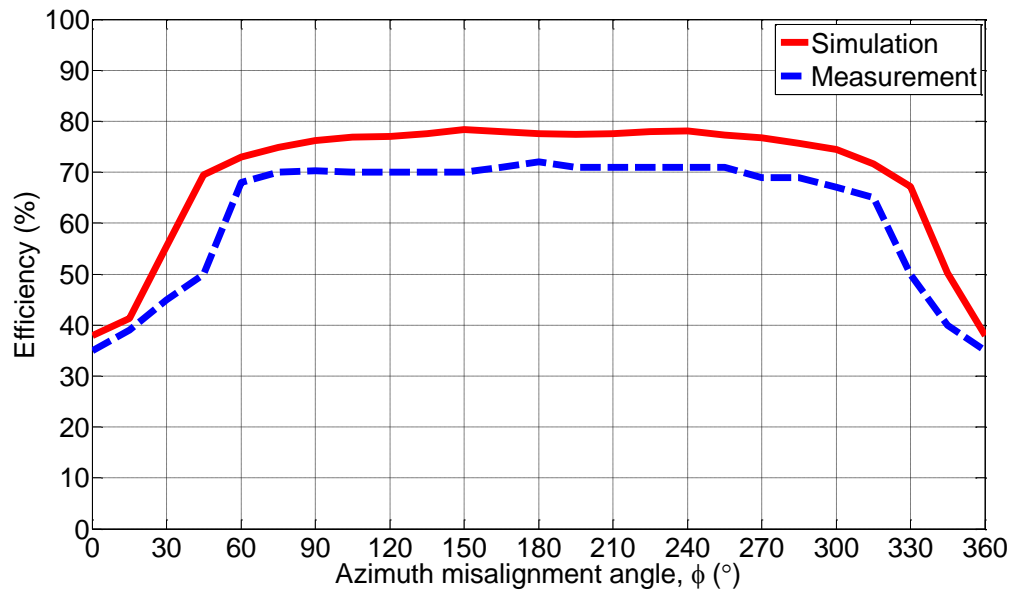


Figure 4.15. Misalignment results of proposed flexible PCB cylindrical SCMR.

Fig. 4.15 shows the misalignment performance for the proposed flexible PCB cylindrical SCMR system. Since it has the same topology with the wire model discussed previously, no nulls were generated throughout the 360° misalignment rotation. This shows that the proposed cylindrical topology is indeed misalignment insensitive independently of the cross-section of the conductive traces. Also, the flexible PCB design achieves higher efficiencies. Specifically, the efficiency varies from 35% to 70% for 0° to 60° , and 270° to 360° misalignment angles. Then, the efficiency stays around 70% from 60° to 270° (measurement data) whereas for the efficiency of the wire model stayed at around 35% for all the angles. The smallest efficiency occurs when the RX elements are at 0° and 360° misalignment angle. At these positions, less magnetic energy can be coupled between TX and RX since the gap of the cylindrical resonator is facing the conformal receiver. Even though the flexible PCB has much thinner trace than the copper wire, its ability to generate higher efficiency is still expected and this is explained in what

follows. The main geometries of both systems (wire and flexible PCB systems) are the same and therefore, the total lengths of the copper wires and flexible PCB traces are the same. The electrical equivalent radius is shown in [28], and for a metal strip whose thickness is negligible, its equivalent circular cylinder radius is

$$a_e = 0.25a \quad (4.7)$$

where a is the width of the strip. In this case, the width of the flexible PCB is 12 mm, therefore the equivalent radius is 3 mm. According to (11), it is obvious that with 0.14Ω , the dc resistance of the flexible PCB model is much smaller than 0.5Ω of the copper wire model, hence higher efficiency is achieved. The cylindrical structures of the source loop and TX resonator are not complete (do not cover 360° of rotation) and this explains the drop in efficiency for low and high angles of misalignment. In conclusion, the proposed flexible PCB cylindrical SCMR system provides misalignment insensitive performance and achieves large efficiencies for most angles.

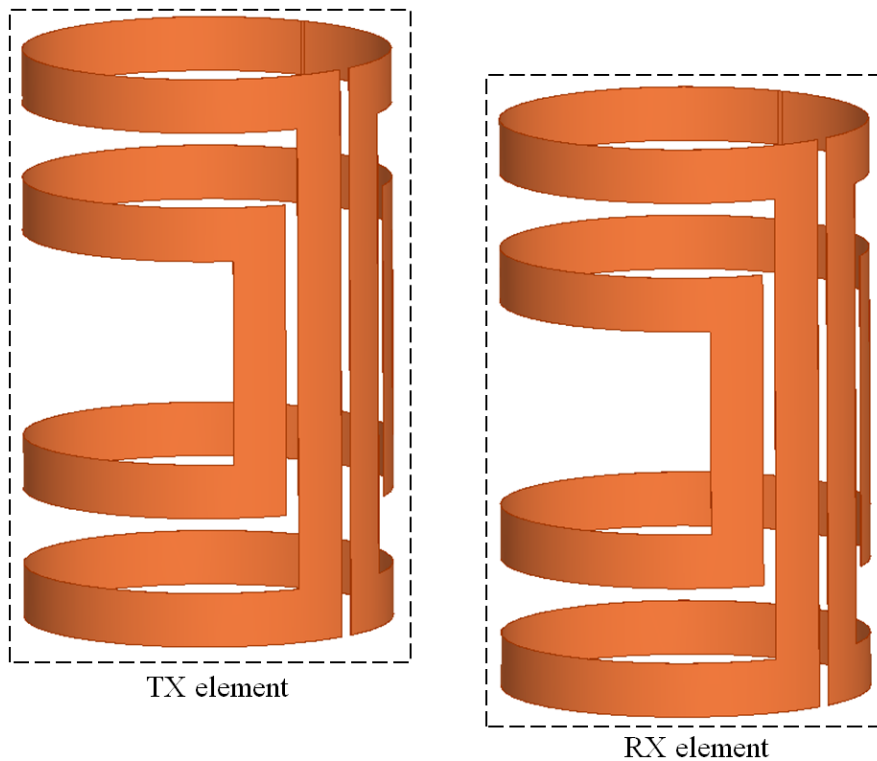


Figure 4.16. Simulation model of flexible PCB cylindrical SCMR with cylindrical TX and RX elements.

To expand upon the results achieved above, the misalignment behavior of a SCMR system with both TX and RX elements being cylindrical, is examined here. Although it was discussed in the introduction section that it is not practical for certain applications to have both TX and RX elements be cylindrical, these results are presented for completeness. In the simulation setup, 0° misalignment is shown in Fig. 4.16 where the RX element is facing the gap of TX element. The distance between the outer surfaces of both elements is 50 mm, which is optimized from simulation to achieve highest efficiency. The smaller range of this SCMR system compared to the system of Fig. 4.12 is expected since this SCMR system is operating at a higher frequency. Since the geometry of the cylinder is different than the conformal SCMR, the frequency where its Q-factor exhibits its maximum is different, therefore the operating frequency is changed.

In this case, the maximum efficiency of the system occurs when the operating frequency is 90 MHz. The capacitors used on both TX and RX elements are 9 pF. The simulated efficiency for different misalignment angles is illustrated below in Fig. 4.17.

Fig. 4.17 shows that the SCMR system with both TX and RX elements cylindrical also exhibits no nulls in the misalignment setup, while achieving relatively high efficiencies. Specifically, the efficiency stays at around 78% from 75° to 285° misalignment angles, while varies from 52% to 78% from 0° to 75° and 285° to 360° misalignment angles. In conclusion, our results indicate that the cylindrical SCMR systems of Figs. 4.12 and 4.16 provide significantly less sensitivity to misalignment compared to standard SCMR and conventional CSCMR systems. Also, the cylindrical SCMR system of Fig. 4.12 will be more practical for most applications as it allows either the TX or the RX to be conformal.

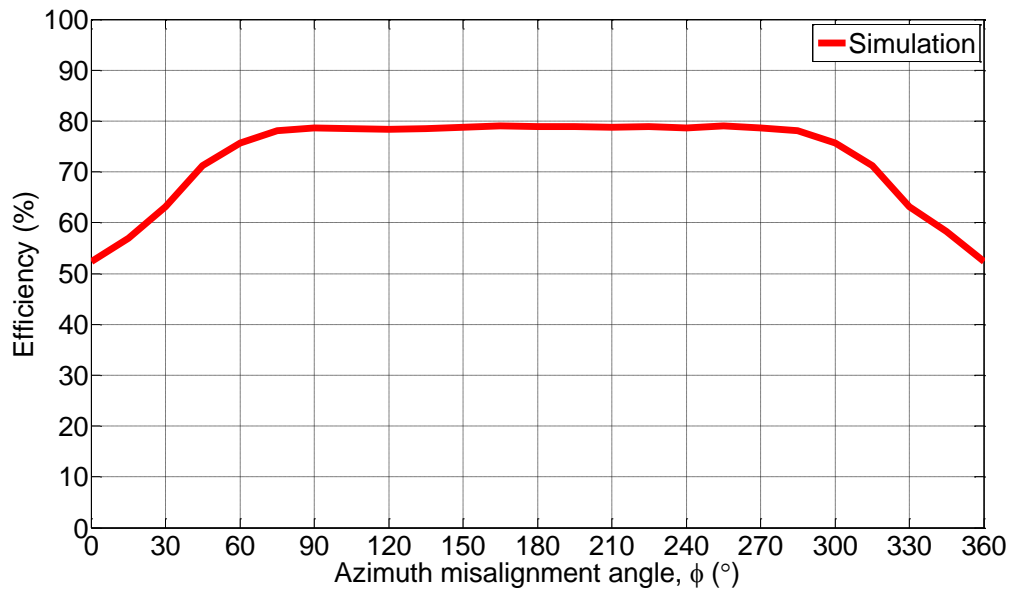


Figure 4.17. Simulated misalignment result of flexible PCB cylindrical SCMR with cylindrical structures for both TX and RX elements.

4.2.3 Lateral Misalignment Comparison of CSCMR and Proposed Cylindrical SCMR

In this section, the lateral misalignment performance comparison of conventional CSCMR and proposed cylindrical SCMR systems is presented. The cylindrical SCMR system with flexible PCB is chosen to be compared with CSCMR for the lateral misalignment for their same 12 mm width copper material and approximately 70% highest achievable efficiencies for both systems. The measurement setups for both systems are consistent with previous sections where the range for CSCMR is 150 mm and 70 mm for cylindrical SCMR. The misalignment angle for CSCMR is set at 0° and 180° for cylindrical SCMR for them to achieve maximum efficiencies. Figs. 4.18 and 4.19 illustrate the measured performance comparison between conventional CSCMR and proposed cylindrical SCMR with flexible PCB for x -axis and z -axis lateral misalignment, respectively. The x -axis and z -axis are defined in Fig. 4.1.

For the x -axis lateral misalignment (see Fig. 4.18), the efficiency of conventional CSCMR stays approximately constant at 70% from 0 cm to 7 cm of lateral misalignment and then gradually drops to almost zero from 7 cm to 18 cm of lateral misalignment. The efficiency of proposed cylindrical SCMR (see Fig. 4.18) stays approximately constant at 70% from 0 cm to 4 cm of lateral misalignment, and then gradually drops to almost zero from 4 cm to 18 cm of lateral misalignment. Therefore, conventional CSCMR has better performance in terms of x -axis lateral misalignment. This is expected as the cylindrical element in this case has smaller width in the x -axis than the conformal element.

For the z -axis lateral misalignment, the performance for conventional CSCMR (see Fig. 4.19) is identical to that of the x -axis lateral misalignment because of the

symmetry in its square design for both transmitter and receiver. However, the efficiency of the proposed cylindrical SCMR (see Fig. 4.19) stays approximately constant at 70% from 0 cm to 3 cm of lateral misalignment, and then gradually drops to almost zero from 3 cm to 9 cm. From 9 cm to 14 cm the efficiency increases from 0 to 32.5% while surpassing the efficiency of CSCMR at 13 cm and starts decreasing again after 14 cm to almost zero at 23 cm. The null of the efficiency at 9 cm and the local maximum at 14 cm can be attributed to destructive and constructive addition of the magnetic fields at these distances, respectively.

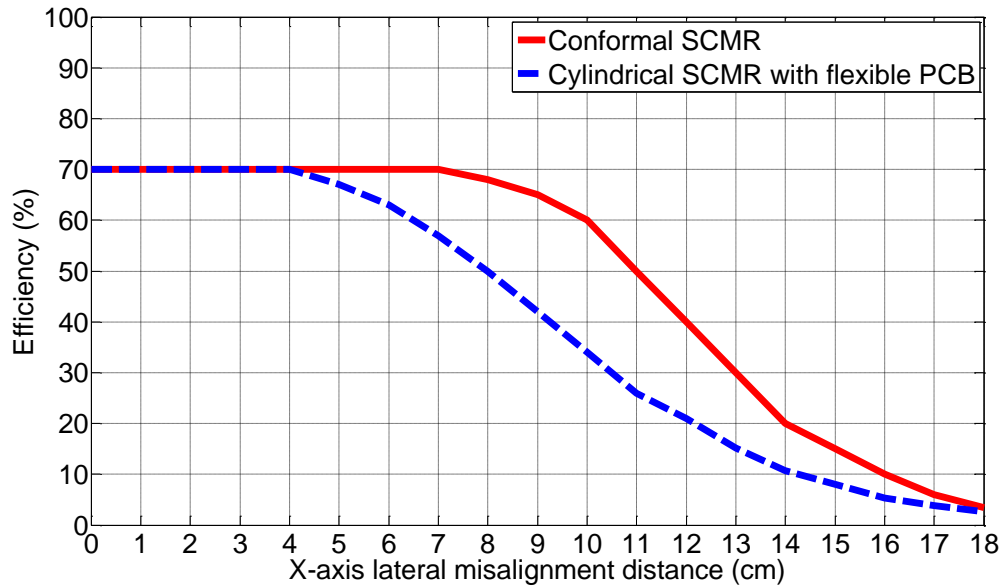


Figure 4.18. Measured x-axis lateral misalignment results of conventional CSCMR and proposed cylindrical SCMR with flexible PCB.

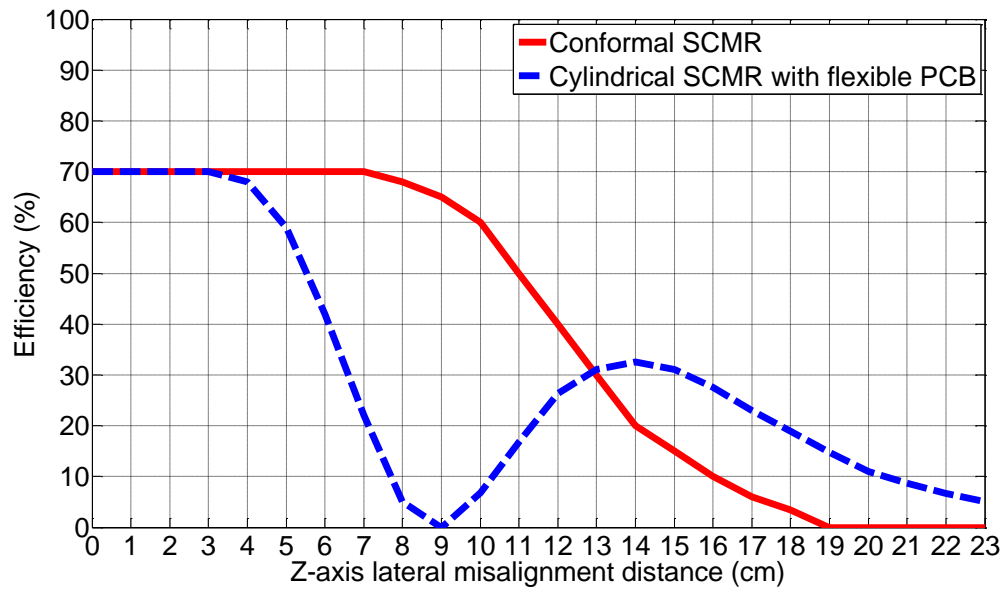


Figure 4.19. Measured z-axis lateral misalignment results of conventional CSCMR and proposed cylindrical SCMR with flexible PCB.

In summary, conventional CSCMR provides better performance than the proposed cylindrical SCMR for both the x -axis and z -axis lateral misalignment. The lateral misalignment results were provided for completeness for this research. However, the proposed cylindrical SCMR design was specifically developed to address the problems of standard SCMR and conventional CSCMR for angular misalignment, for which it indeed provided significantly improved performance with no nulls in the efficiency.

4.3 Wearable Applications for Cylindrical SCMR systems

In previous sections, the conventional CSCMR and the proposed cylindrical SCMR were compared in terms of their misalignment sensitivity and it was concluded that the proposed cylindrical geometry is significantly less misalignment sensitive as it exhibits no nulls through the 360° of misalignment rotation. Specifically, the proposed

cylindrical SCMR system with flexible PCB maintained approximately constant efficiency of 70% from 60° to 270° of misalignment angle, and exhibited an efficiency that varied from approximately 35% to 70% for misalignment angles between 0° to 60° and 270° to 360°, as shown in Fig. 4.15. In this section, the possible wearable applications of this proposed cylindrical topology are discussed.

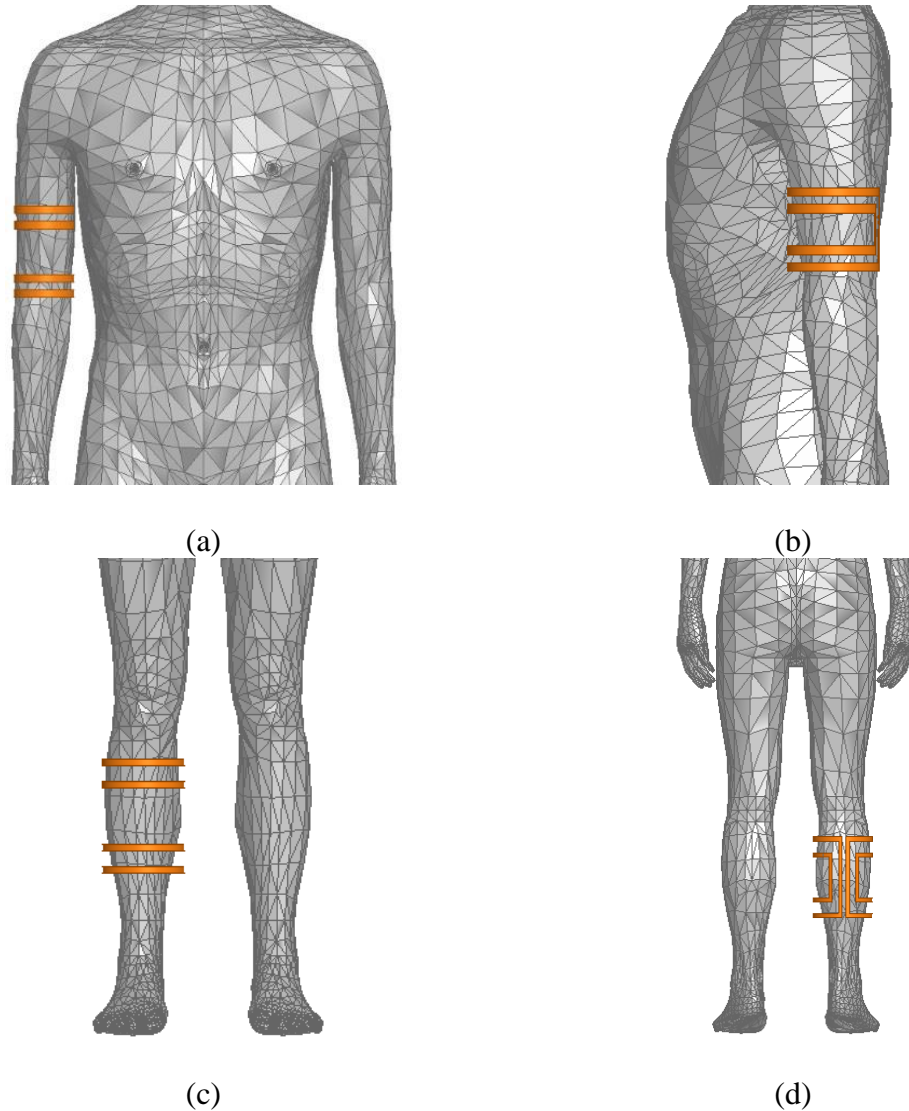
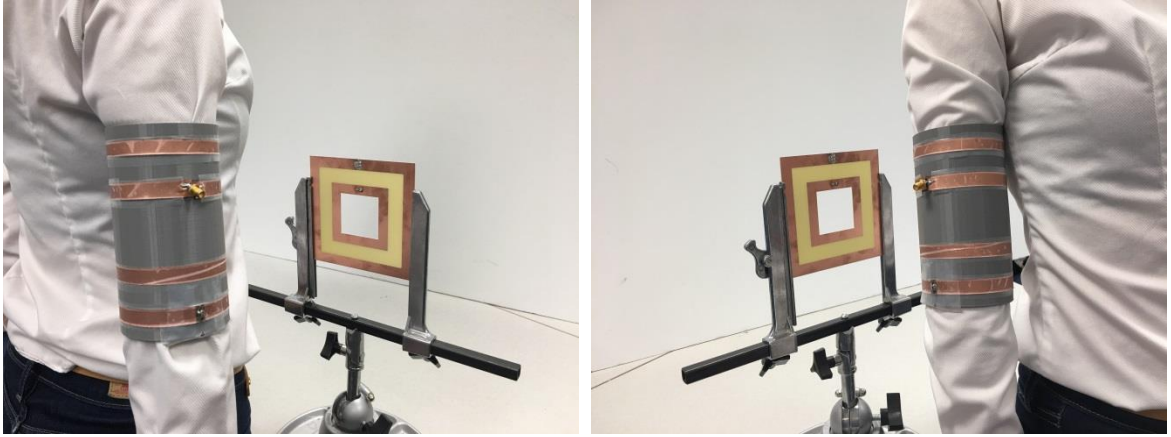


Figure 4.20. Demonstration of wearable cylindrical SCMR in simulation.

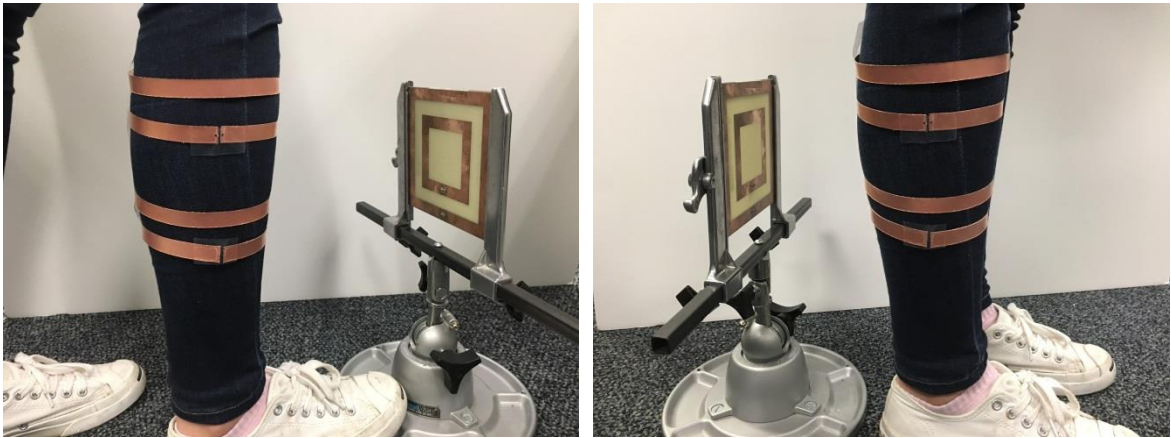
Given the cylindrical geometry of the proposed SCMR system, the new models can easily be wrapped around a human's arm or leg while maintaining its shape and

position, as shown in Fig. 4.20. A human body model that includes more than 300 parts of biological tissues was used. In this human body model the materials of biological tissues are characterized by 28 sets of frequency-dependent relative permittivity ϵ_r and conductivity σ . This model is compatible with ANSYS HFSS and it was used in our simulations. Also, in order to show how this system actually works in future practical applications, the cylindrical system prototype with flexible PCB was placed on the arm and leg of a volunteer, as shown in Fig. 4.21. Such cylindrical elements can be implemented either on wearable devices that separate the elements from the skin using non-metallic materials or they can be woven into the clothes (i.e., electronics woven in textiles). It is worth mentioning that in this wearable application, the transmitter is the conformal planar element and the receiver is the cylindrical element. For practical reasons, the volunteer rotates from facing the conformal transmitter as shown in Fig. 4.21 (a) and (c) to the opposite way illustrated in Fig. 4.21 (b) and (d), which is a 180° rotation. Given that only 180° rotation is needed here, the part of the cylindrical structure that is not complete can be avoided which will eliminate low efficiencies caused by the gap thereby enabling this wearable system to have high steady efficiencies through 180° of misalignment. For comparison purposes, the distance between the transmitter and receiver is kept the same with the system presented in the previous section. The following results are from the model being wrapped around the arm, as an example.



(a)

(b)



(c)

(d)

Figure 4.21. Wearable cylindrical SCMR in measurement setup.

Fig. 4.22 illustrates the results from both simulation with human body in HFSS and measurement. Fig. 4.22 is a plot only showing 0° to 180° misalignment, as discussed previously in this section. In wearable situations, it is most practical to only measure 0° to 180° misalignment, with 0° being the volunteer facing the conformal elements, and 180° being her facing away from the conformal elements (see Fig. 4.21). With this setup and by facing the gap of the cylindrical loops towards the human body, we can avoid the angles that face this gap toward the conformal TX element, which yields lower

efficiencies as shown in Fig. 4.15. In other words, Fig. 4.22 shows the efficiencies from 90° to 270° per the setup of Fig. 4.15, and this is the reason that the efficiency does not decrease at the beginning and end of Fig. 4.22. Since the cylindrical elements are wrapped around human arm, the performance of the system is affected by the properties of the human body, which are shown in Table 4.1. Here, we only listed the four sets of the biological tissue properties that were most relevant to this specific placement, i.e., wrapping around the arm. During the simulation process, all of the properties in Table 4.1 are taken into consideration. Given that the material resistivity is the reciprocal value of the conductivity, the optimal design of the system will be different. The simulated and measured results also show that the efficiency of this design in the wearable case (see Fig. 4.22) is approximately 10% lower than the efficiency of the same design in air (see Fig. 4.15).

Table 4.1. Material Properties of Human Body in Simulation

	Permittivity	Conductivity
Blood	154.6	1.15
Bone	36.6	0.0925
Fatty tissue	9.726	0.032
Muscle	107.2	0.67

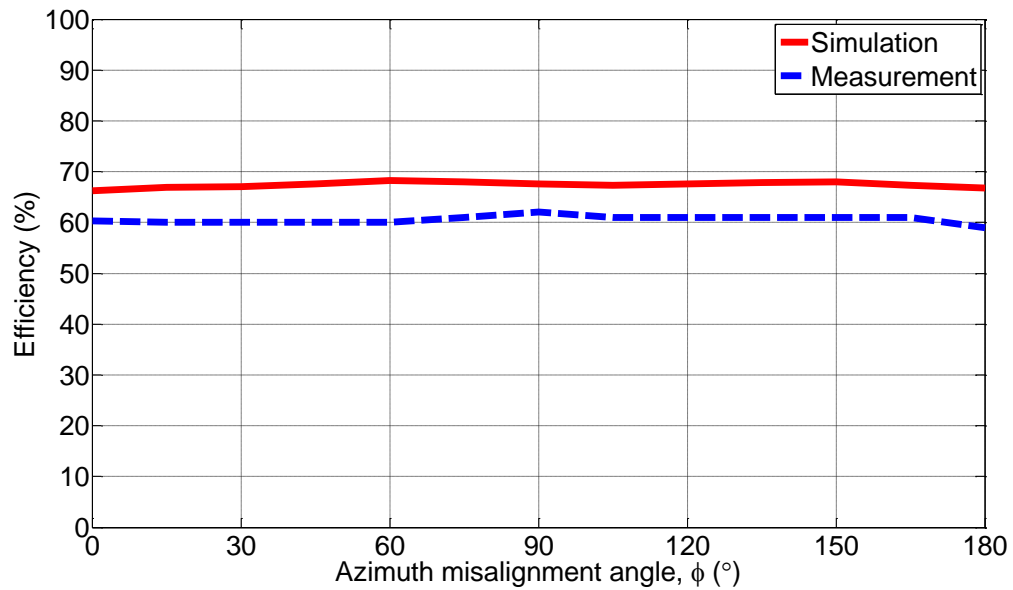


Figure 4.22. Misalignment results of wearable cylindrical SCMR system from 0° to 180° (this angle range corresponds to angles 90° to 270° per the setup of Fig. 4.15).

The purpose of this section is to demonstrate that the cylindrical system presented earlier provides misalignment insensitive performance also for wearable scenarios. Detailed investigation of such scenarios is beyond the scope of this paper and the optimization of the proposed cylindrical SCMR systems for wearable applications will be studied by future research. Furthermore, the safety of such wearable systems according to the relevant safety regulations will be studied in the future. The slight difference in efficiency between simulation and measurement is because the capacitors used in the prototype are not ideal as in simulation, therefore slightly affecting the performance of the system. The results of Fig. 4.22 clearly show that this cylindrical SCMR topology can be used as a wearable device, if direct contact with the skin is avoided.

The advantage of this system for wearable applications is that no matter which way a person turns, this device can always transfer or receive power or data as needed,

without concerns of the orientation. One good example of the application would be for a patient lying in bed in a hospital. The conformal transmitter (receiver) could be set under the bed while the cylindrical receiver (transmitter) is wrapped around the patient's arm or leg. With this setup, no matter which way the patient is turning, power or data can always be wirelessly transferred. As a result, using the wearable cylindrical system can be very convenient for a patient by eliminating all the wires whilst maintaining a high efficiency.

4.4 Optimizing Cylindrical SCMR

Previously, it was mentioned that in our designs, the geometries of the cylindrical elements are kept consistent with the geometry of the CSCMR design in terms of the heights of the source loop and TX resonator. This was done to have a consistent comparison among all the designs, and to ensure that size differences did not contribute to differences in efficiency. However, this procedure results in the cylindrical elements not resonating at the maximum Q-factor frequency, as shown in Figs. 4.7 and 4.13, hence the highest possible efficiency was not achieved. In order to optimize the cylindrical SCMR system to achieve higher efficiency, in this section we design a cylindrical SCMR system based on wire elements for the TX and RX elements with maximum Q-factor at the operating frequency of 27.12 MHz.

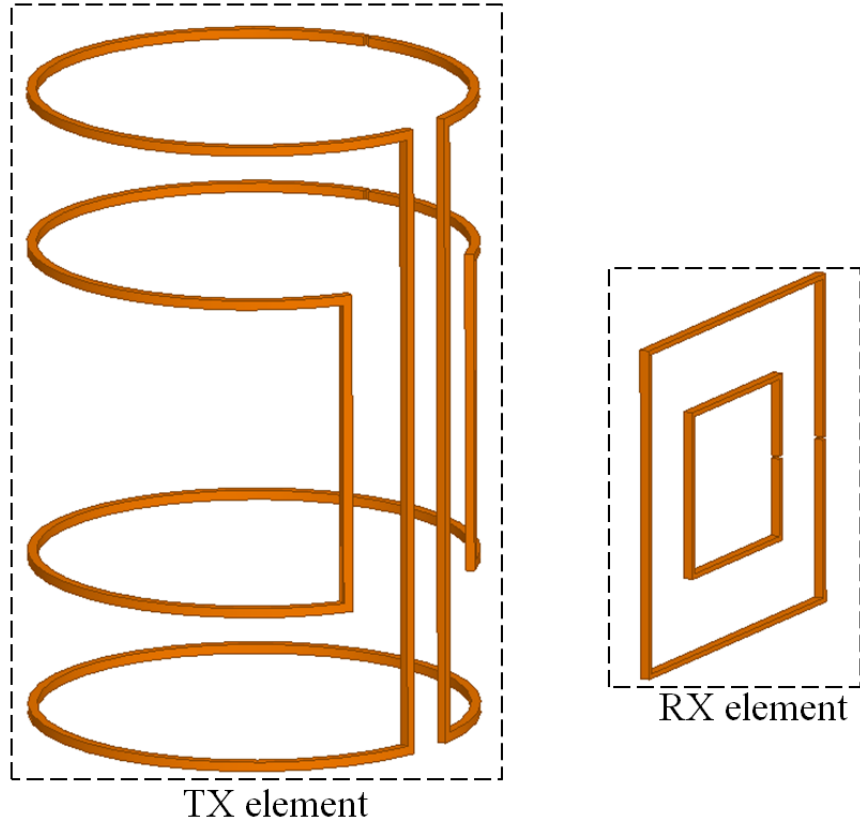


Figure 4.23. Optimized cylindrical SCMR system based on wire elements.

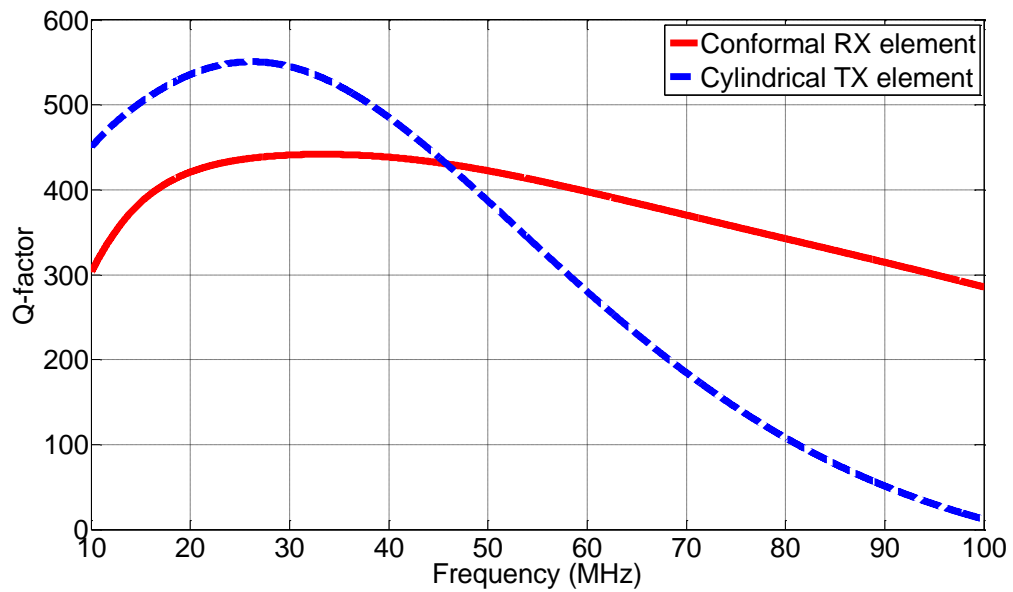


Figure 4.24. Simulated Q-factor of elements of optimized cylindrical SCMR system based on wire elements.

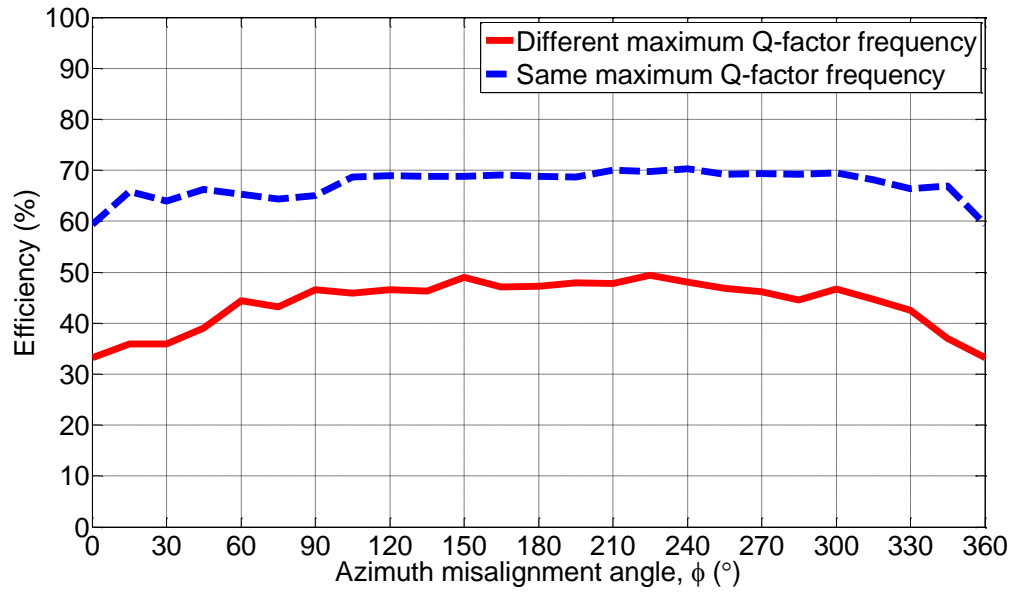


Figure 4.25. Comparison of simulated misalignment results of proposed and optimized cylindrical SCMR systems based on wire elements.

As was shown in Fig.4.7, the maximum Q-factor frequency of the cylindrical element is larger than the operating frequency. In order to optimize the efficiency, the size of the cylindrical element has to be larger for the Q-factor to resonate at a lower frequency. Using simulation tools, we found out that when the cylindrical TX element is 1.9 times larger than the original size while the conformal RX element stays the same, the frequency of the maximum Q-factor of both elements coincide at 27.12 MHz.

The optimized cylindrical SCMR system is shown in Fig. 4.23 and its specifications are as follows. The radius of the cylindrical elements is 76 mm. The height of the TX resonator is 218.5 mm. The height of the source loop is 109.25 mm. The conformal RX element is the same with the design in section 4.1, where the height of RX resonator is 115 mm and the height of load loop is 57.5 mm. The distance between the outer surface of the TX and RX element is 70 mm. The capacitors for TX and RX

resonators are 54 pF and 100 pF, respectively. This system design results in the same maximum Q-factor frequency of 27.2 MHz for both TX and RX elements, as it can be seen in Fig. 4.24.

Given that in this design both TX and RX resonators achieve their maximum Q-factor at the same frequency, this design should achieve higher efficiency than the previous design. Fig. 4.25 confirms this, as it shows that the efficiency of the design presented here (that has TX and RX resonators exhibiting maximum Q-factors at 27.12 MHz) is significantly larger than the efficiency of the design in section 4.1 (that has TX and RX resonators that do not both exhibit maximum Q-factors at 27.12 MHz). Specifically, the efficiency of the optimized cylindrical SCMR system is approximately 20% larger than the efficiency of the design in section 4.1 over the entire 360° of misalignment rotation.

This chapter aimed to present a novel structure that generates no nulls throughout the 360° misalignment rotation and this was achieved by both the optimized design of this section (with TX and RX resonators that exhibit maximum Q-factors at 27.12 MHz) as well the design of section 4.1 (with TX and RX resonators that have the same height). It was also shown that optimization of the efficiency can be done by changing the size of the cylindrical element. Before this section, the heights of the TX and RX resonators of all designs were kept the same to avoid comparing elements with different heights and introducing another variable in the comparison of the designs that could lead to uncertainty about their performance comparison.

CHAPTER 5

SIMULTANEOUS POWER AND DATA TRANSFER WITH BROADBAND STRONGLY COUPLED MAGNETIC RESONANT SYSTEM

In this chapter, a planar broadband CSCMR system is designed, and it is implemented with backscattering modulation to transfer power and data simultaneously. The design of the broadband planar CSCMR system is presented in Section 5.1. In Section 5.2, the system description for all the components is discussed, which includes backscattering modulation, data rate discussion, power transmitter/data receiver and RF-to-DC converter/data transmitter. The performance of the system is shown with measurement results in Section 5.3. This system is able to achieve high efficiency wireless power transmission while transferring 10 Mbps data signal through the same link.

5.1 Design of Planar Broadband CSCMR system

The ability to transfer power and data simultaneously through the same wireless link can be beneficial when implementing SCMR system with sensors. This way, battery-free sensors can be used for situations where it is not practical to change batteries for sensors, such as inside concrete or inside the human body. Furthermore, the wider the bandwidth, the higher data rate the system can achieve, making broadband system preferable for such applications. A broadband CSCMR system, which uses two resonator loops instead of one in each TX/RX element was first proposed in [50]. The system presented in [50] used copper wire for all the loops, as shown in Figure 5.1 (a), so it was not suitable for PCB manufacturing. Here, a broadband and planar CSCMR system is developed that is suitable for PCBs, as shown in Figure 5.1(b); therefore, this design is

more appropriate for practical applications. In a broadband CSCMR system, the inner loop is the source/load loop; the middle loop is the inner resonator loop whose radius and capacitor value determine the center operating frequency; the outer loop is the outer resonator loop whose radius and capacitor value are adjusted according to the inner resonator size to achieve the needed bandwidth. The radii of the inner loop, middle loop and outer loop are r_1 , r_2 and r_3 , respectively, and the cross-sectional radius of the copper wire is r_c , as shown in Figure 5.1 (a). In what follows, the design process of our planar broadband CSCMR system will be discussed.

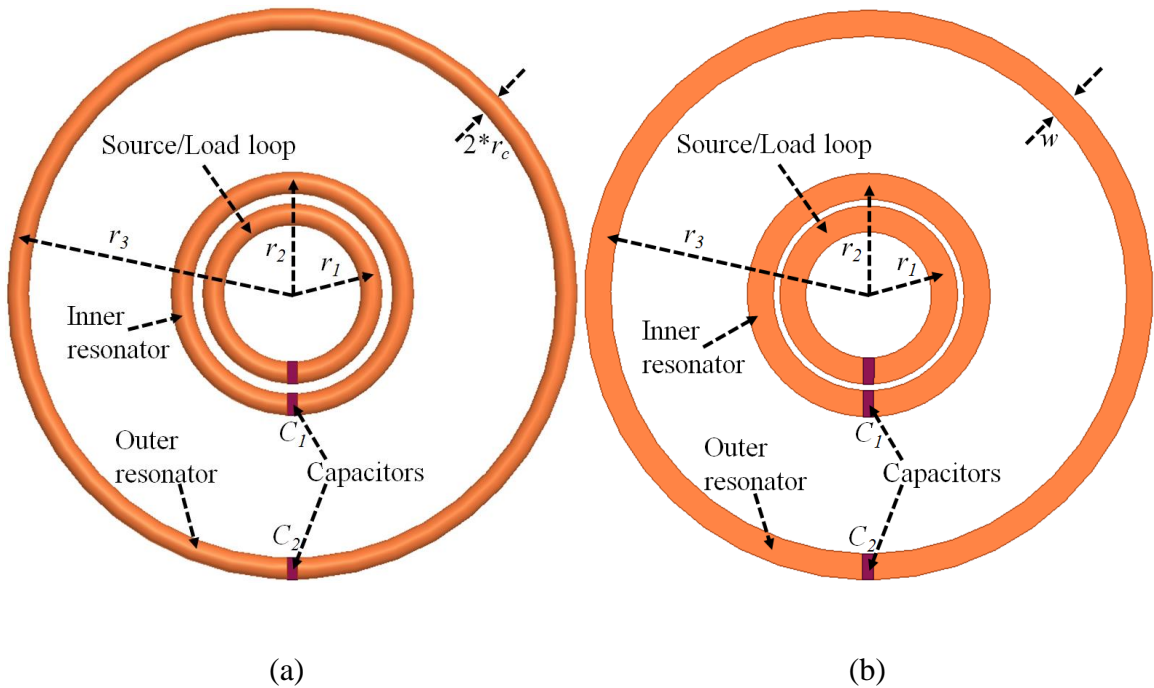


Figure 5.1. Geometry of a broadband CSCMR TX or RX element: (a) wire-based, (b) PCB-based.

Figure 5.1 (b) illustrates similar geometrical parameters for the planar broadband CSCMR, where w is the trace-width. To convert the wire-based CSCMR design to the planar one, the equivalent planar trace-width of a circular wire is calculated according to the following equation and assuming the thickness of the copper trace is negligible [54]:

$$a = 4a_e \quad (5.1)$$

where a is the trace-width, and a_e is the cross-sectional radius, as shown in Figure 5.2. In other words, the equivalent trace-width is 4 times the cross-sectional radius of the copper wire. Since eq. (5.1) is an approximate relationship, simulations need to be performed to find the optimal equivalent trace-width.

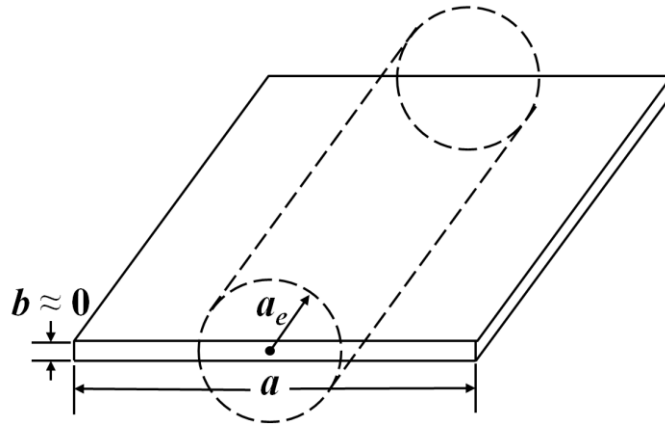


Figure 5.2. Electrical equivalent radius from circular cylindrical wire.

Our objective here, is to develop a broadband CSCMR system with center frequency of 100 MHz. First, a wire narrowband CSCMR system is developed to find the optimal relation between the wire cross-sectional radius and the trace width for a 1.6-mm thick FR4 board that we plan to use for our broadband design. The copper wire cross-sectional radius r_c is set to be 1.5 mm. From eq. (2.3) and (2.5), the radius and capacitor value of the SCMR system resonator loop can be derived as 42.4 mm and 13.9 pF, respectively. The radius of the source and load loop is set as 28 mm, $2/3$ of the size of the resonators [50]. Then, this wire CSCMR system is converted to a planar one. The planar CSCMR has all the same design parameters as the wire one except for the trace width. Since (5.1) is an approximate relation simulations with ANSYS HFSS are performed for

different trace-widths, w , to find the optimal value of w that provides maximum efficiency at 100 MHz. Figure 5.3 illustrates the simulated wireless power transfer efficiency of the planar CSCMR system for different equivalent trace-widths. These results show that when the trace-width is 4 times the cross-sectional radius of the wire, the operating frequency is higher than 100 MHz; however, as the trace-width decreases, the operating frequency decreases as well. When the trace-width is 3.2 times the cross-sectional radius of the wire, the center frequency of the planar system is 100 MHz, which is the desired operating frequency. Using this optimal trace-width, the size of the main resonator can be determined by eq. (2.3).

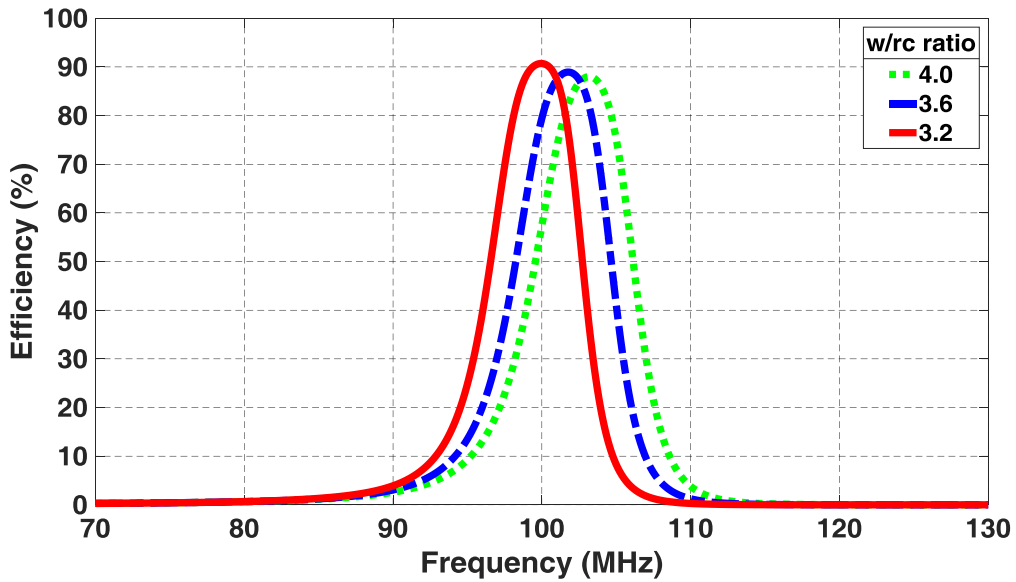


Figure 5.3. Simulated efficiency results of different trace-width.

To develop our broadband CSCMR design (using $w = 3.2r_c$), a similar process to the one presented in [50] is followed to find the optimal ratios of r_2/r_1 , r_3/r_2 , and d/r_3 (where d is the distance between the transmitter and the receiver of the CSCMR system).

The steps of this process are as follows and all the data are simulated using ANSYS HFSS:

- (a) Figure 5.4 plots the simulation comparison of broadband CSCMR efficiency for different r_2/r_1 ratios. It can be observed that when $r_2/r_1 = 1.4$ the performance of the broadband CSCMR is optimal in terms of power transfer efficiency and flatness of the efficiency plot. Therefore, it can be concluded that the optimal ratio of r_2/r_1 is 1.4.

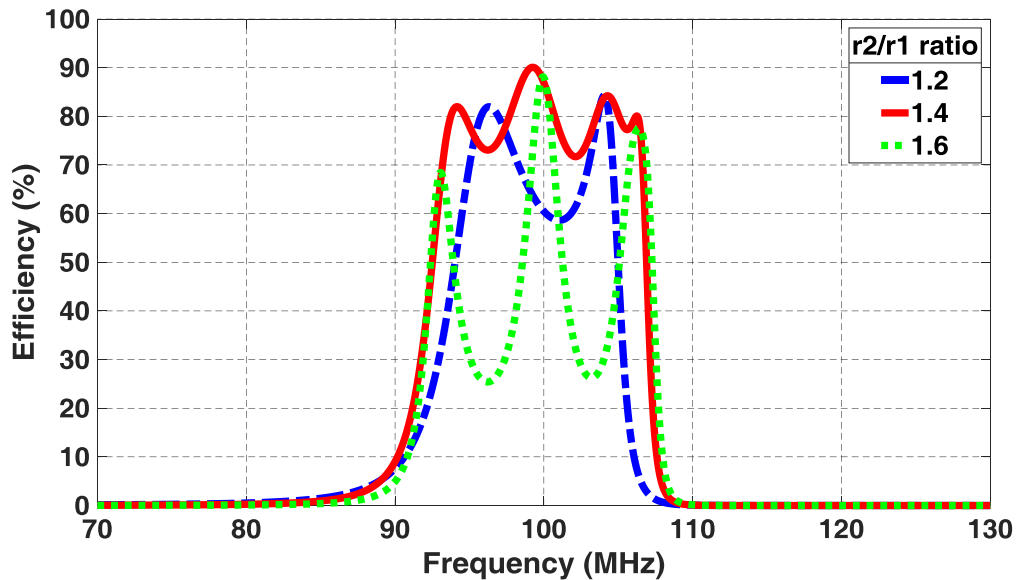


Figure 5.4. Simulated efficiency results of different r_2/r_1 ratio.

- (b) The simulated results illustrated in Figure 5.5 show the performance of the broadband CSCMR for different values of r_3 . Specifically, when the ratio of r_3/r_2 is 2.3 and 2.7, both systems have large drops in their efficiency and when r_3/r_2 ratio is equal to 2.5 the system has the best performance.

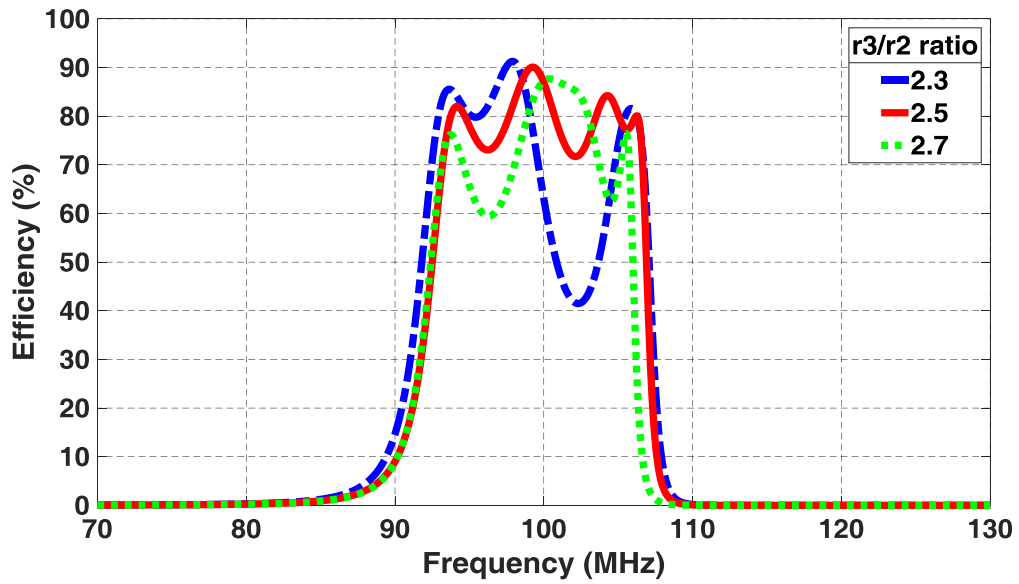


Figure 5.5. Simulated efficiency results of different r_3/r_2 ratio.

(c) Figure 5.6 shows that the bandwidth and efficiency of our system are optimal when the operating distance is equal to the radius of the outer resonator.

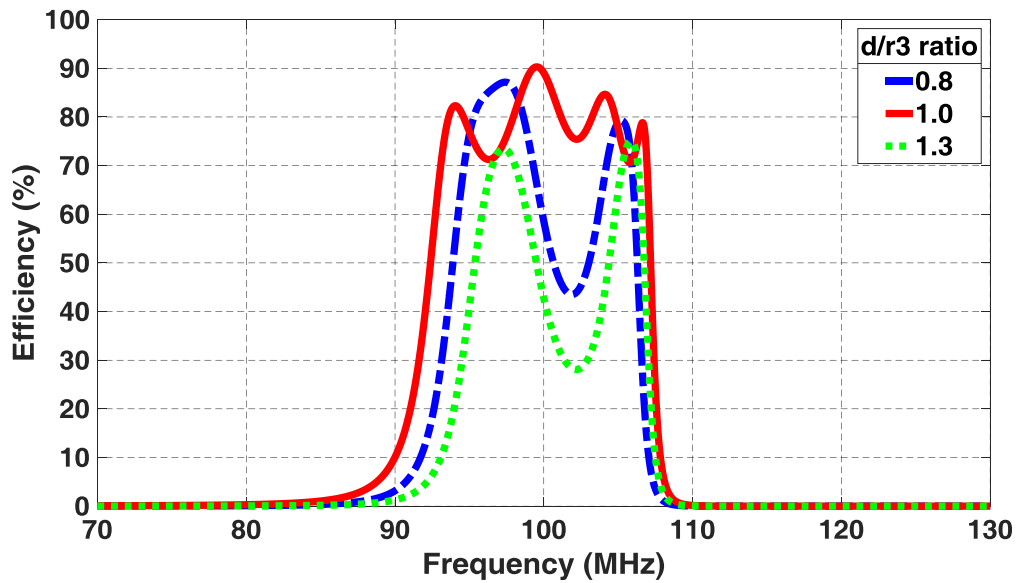


Figure 5.6. Simulated efficiency results of different d/r_3 ratio.

In summary, our broadband planar CSCMR systems on 1.6-mm thick FR4 board can be designed as follows: the equivalent trace-width w is 3.2 times the radius of the copper wire; r_2 is determined by the operating frequency and trace-width from eq. (2.3); $r_1 = r_2/1.4$; $r_3 = 2.5r_2$; the optimal distance, $d = r_3$; the capacitor value for r_2 is determined by eq. (2.5) and the capacitor value for r_3 is optimized by simulation. Based on these criteria, a broadband planar CSCMR system whose operating frequency is 120 MHz has the following specifications: $r_1 = 25$ mm; $r_2 = 35$ mm; $r_3 = 87.5$ mm; $w = 4.8$ mm; $C_1 = 12$ pf; $C_2 = 2.7$ pf and $d = 87.5$ mm.

However, designs generated following this method are often large, especially when operating at low frequencies. For example, in our system that operates at 120 MHz, the diameter for the outermost loop is 175 mm, which is large for practical applications (including wearable or embedded sensors). Therefore, miniaturization of our broadband planar CSCMR systems is needed.

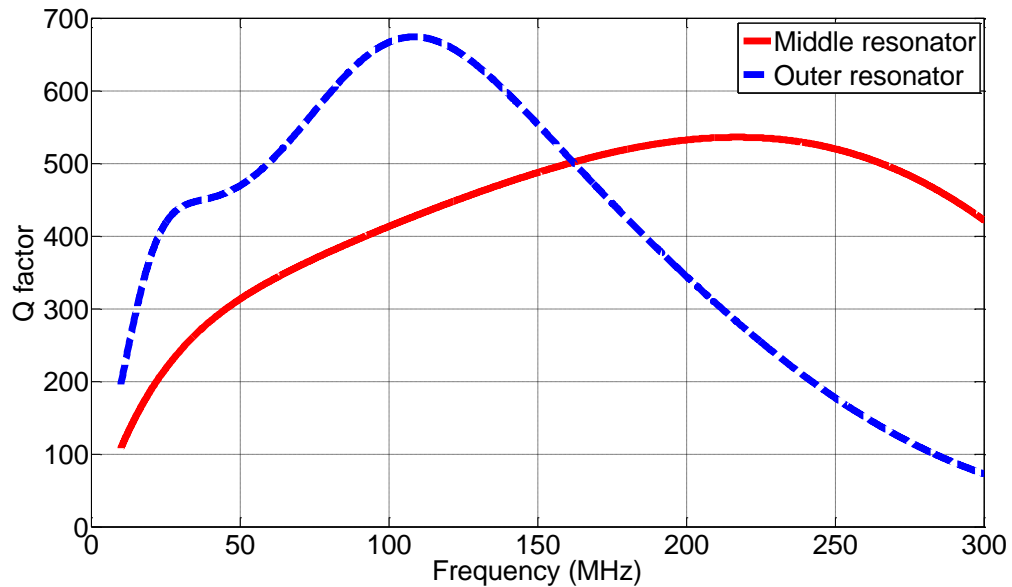


Figure 5.7. Q-factors of the two resonators.

Therefore, in what follows we design a new miniaturized broadband CSCMR system based on the same optimal structure ratios identified above: $r_1 = 14$ mm; $r_2 = 20$ mm; $r_3 = 50$ mm; $w = 4.8$ mm and $d = 50$ mm. The Q-factors for both resonator loops are presented in Figure 5.7. Observing from the plot, the maximum Q-factor for r_2 is around 220 MHz, and for r_3 is around 100 MHz. Given the fact that these two resonators are both contributing to the broadband performance, the operating frequency should take both resonators' Q-factor into consideration. For this specific case, we determine it is acceptable when both Q-factors are above 400 for our system, which is 100 MHz to 180 MHz.

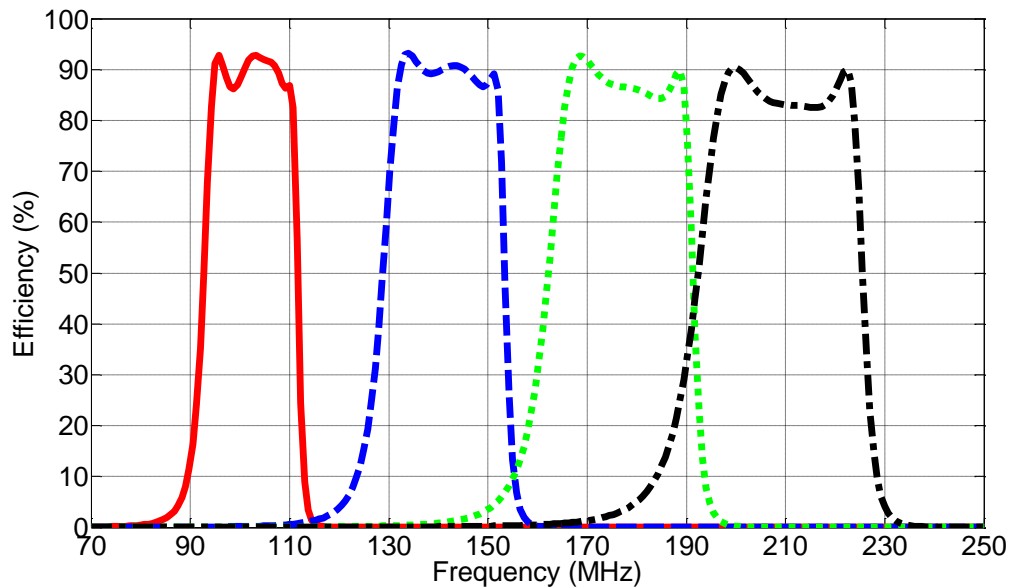


Figure 5.8. Simulated efficiency for different capacitors.

Next, the capacitor values for the resonators are changed, while the other parameters of the system stay the same. It is seen that the maximum efficiency of all four plots are above 80% while providing large bandwidth. Table 5.1 further illustrates this plot by listing the capacitor values and the resulting bandwidth. It can be concluded that a

broadband planar CSCMR system can be used for a long range of frequencies, which is determined by the Q-factors of both resonators. As the operating frequency gets higher, the fractional bandwidth slightly decreases, which is in accordance with the Q-factor plot. The interaction between the two resonators and the acceptable operating frequency range is very important to the design of broadband planar CSCMR, and it will be studied in future research. It is worth noting that at 210 MHz, the system becomes extremely sensitive to capacitor value changes. A difference in capacitor value as little as 0.5 pF will largely compromise the broadband performance, hence it is not recommended to tune the system to operate at a frequency that is beyond the acceptable Q-factor range.

Table 5.1. Bandwidth Range with Different Capacitors

C_1 (pF)	C_2 (pF)	Center Frequency (MHz)	-3 dB Bandwidth (MHz)	Fractional Bandwidth
40	10	100	92.55~111.74 (19.19)	19.2%
25	6	130	118.23~141.49 (23.26)	17.9%
21.5	5	140	128.55~153.55 (25)	17.9%
17.5	4	155	142.66~169.4 (26.74)	17.3%
14	3	175	161.82~191.44 (29.62)	17%
10.2	2	210	191.92~225.69 (33.77)	16.2%

Based on the discussion above, the finalized broadband planar CSCMR design parameters are as follows: $r_1 = 14$ mm; $r_2 = 20$ mm; $r_3 = 50$ mm; $w = 4.8$ mm; $d = 50$ mm; $C_1 = 31$ pf; $C_2 = 7.6$ pf and the center operating frequency is 117 MHz. The simulated and measured efficiency for this system are shown in Figure 5.9. The agreement between the

simulations and measurements is very good and the slight difference in both bandwidth and efficiency is due to the capacitor loss that it is not taken into account in our simulations. In the following sections, this broadband planar CSCMR design will be used to combine wireless power transfer and high-data rate communication.

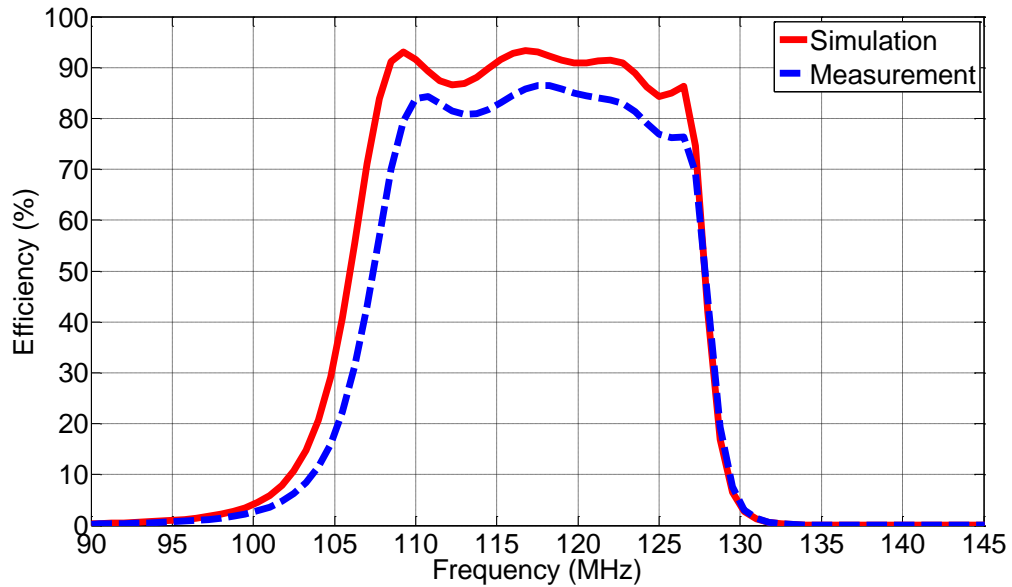


Figure 5.9. Simulated and measured efficiency results of the broadband planar CSCMR system.

5.2 System Description

In this section, power transfer and high data-rate communication are combined through the same wireless link. Figure 5.10 illustrates a system with a power transmitter that wirelessly sends power to a sensor, which in turn sends its data back to the transmitter through the same wireless link. It is expected that this type of system will enable new battery-free wireless sensors for various applications such as, implantable and wearable devices as well as structural health monitoring. In what follows the system is explained.

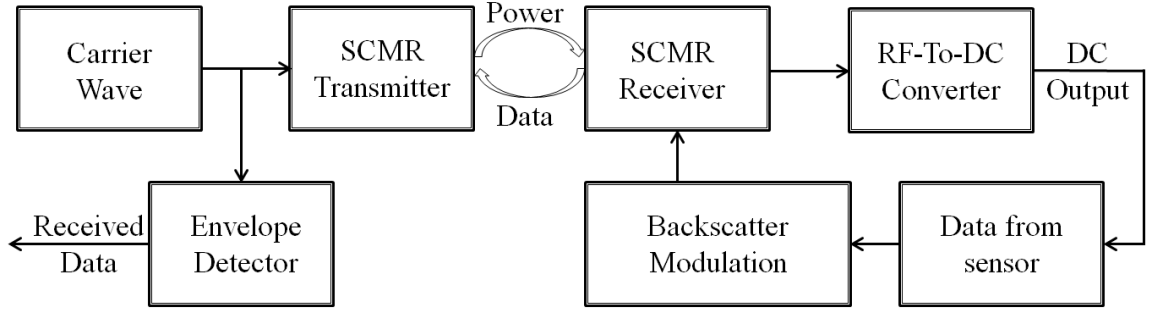


Figure 5.10. Block diagram of the system description.

5.2.1 Backscattering modulation

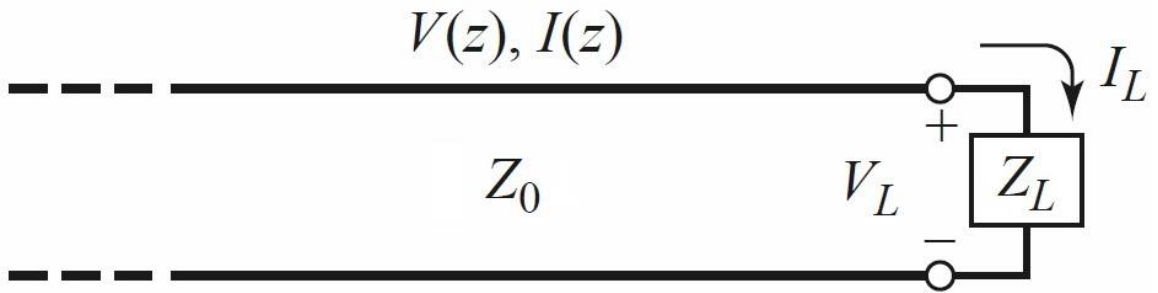


Figure 5.11. Lossless terminated transmission line.

Consider the case of an RF wave being transmitted on a lossless transmission line with a characteristic impedance of Z_0 , terminated with a load impedance Z_L , as seen in Figure 5.11. According to transmission line theory, if Z_L is not matched with Z_0 , a portion of the power destined for the load will be reflected back to the source. The amount of reflection depends on the reflection coefficient, defined as:

$$\Gamma = \frac{V_0^-}{V_0^+} = \frac{Z_L - Z_0}{Z_L + Z_0} \quad (5.2)$$

This fact can be exploited to achieve data communication. By varying the load impedance between two states, a backscattering system is able to harness the received wave and reflect it back in a modulated state. To elaborate, consider an extreme case where the load is switching between open and short circuit state. When the load is open,

Z_L is infinite, the reflection coefficient is 1, which means the source wave will be reflected back entirely in its positive polarity; when the load is short, Z_L is 0, the reflection coefficient is -1, which means the source wave will be reflected back entirely in its negative polarity. By switching between these two states, the source wave will be modulated by the load impedance and this is how the data is transmitted.

In our implementation, switching between two impedance states is accomplished by using a MOSFET. As shown in Figure 5.12, the data stream in the form of voltage signals is connected to the gate of the MOSFET as the control signal while the drain is connected to the SCMR RX element and source is connected to the ground. The load impedance will depend upon the state of the transistor. When the transistor conducts, Z_L will be small; when the transistor is off, Z_L will be large.

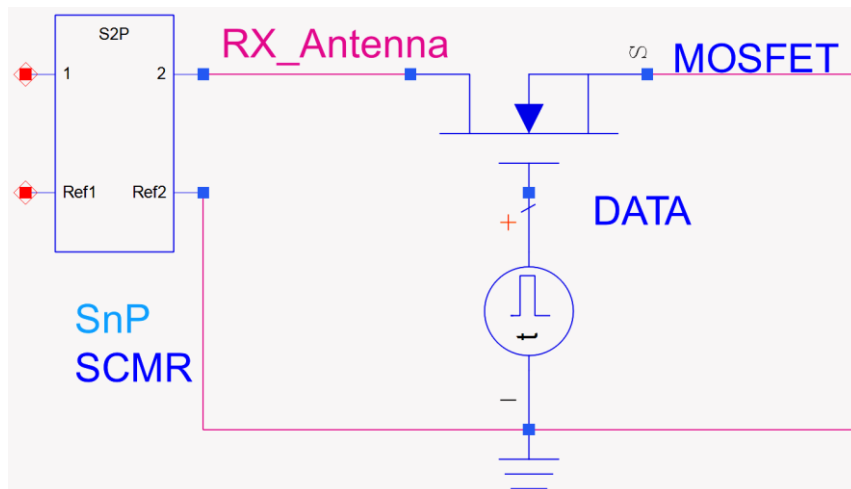


Figure 5.12. Simulation schematic of the backscattering modulation.

5.2.2 Data rate

The Shannon-Hartley theorem illustrates the maximum rate at which information can be transmitted over a communication channel of a specified bandwidth in the presence of noise, whose formula is as follows:

$$C = B \log_2 \left(1 + \frac{S}{N} \right) \quad (5.3)$$

where C is the channel capacity of the wireless link, B is the bandwidth of the channel, S/N is the power ratio of the communication signal to the noise and interference at the receiver. It demonstrates the theoretical upper bound of a communication link. Therefore, the channel capacity can be increased by either: increasing the bandwidth or by increasing the SNR. Assuming SNR is kept the same, a wireless link that has larger bandwidth is bound to have larger channel capacity than a narrowband system. This is why broadband planar CSCMR system is essential because it can be utilized in applications where high data rate communication is required.

In [77], it was mentioned that different data rate is required for different medical applications. The highest target data rate application is for video/medical imaging, which is 10 Mbps. This paper aims to develop a system that can simultaneously transmit power and communicate with high data rates; therefore, a data rate of 10 Mbps is used as an example specification. However, our proposed broadband planar CSCMR system is capable of supporting significantly higher data rate communication due to its large bandwidth, which is an advantage for future applications. Since the load impedance in our system changes between two states, only binary data can be transmitted. Therefore, if our system is able to transfer a data signal at 5 MHz frequency, the data rate would subsequently be 10 Mbps.

Table 5.2. Data Rate Required for Different Applications [77]

Application	Target data-rate
Deep brain stimulation	1 Mbps
Hearing aid	200 kbps
Capsule endoscope	1 Mbps
Drug dosage	<1 kbps
ECG	72 kbps (500 Hz sample, 12-bit ADC, 12 channels)
EEG	86.4 kbps (300 Hz sample, 12-bit ADC, 24 channels)
EMG	1.536 Mbps (8 kHz sample, 16-bit ADC, 12 channels)
O ₂ /CO ₂ /BP/respiration/glucose monitoring, accelerometer	<10 kbps
Audio	1 Mbps
Video/medical imaging	<10 Mbps

5.2.3 Power transmitter/data receiver

The schematic of the power transmitter (which is also the data receiver) circuit is shown in Figure 5.13. The CARRIER port is connected to 117 MHz RF power source; the TX port is connected to our broadband planar CSCMR TX element and the ENVELOPE port is connected to an oscillator for receiving data send through backscattering modulation. The backscattered modulated signal goes through an envelope

detector, which consists of a Schottky diode, capacitors and a resistor. The values of the RC circuit components in this envelope detector are determined by the carrier frequency and message bandwidth to satisfy the following relations:

$$\frac{1}{f_c} \ll RC \ll \frac{1}{W} \quad (5.4)$$

where f_c is the carrier frequency and W is the message bandwidth; in our case, 117 MHz and 5 MHz, respectively. Based on (9), we chose $R = 470 \Omega$ and $C = 100$ pf. The additional capacitor C_2 is used as a coupling capacitor, which blocks DC signals.

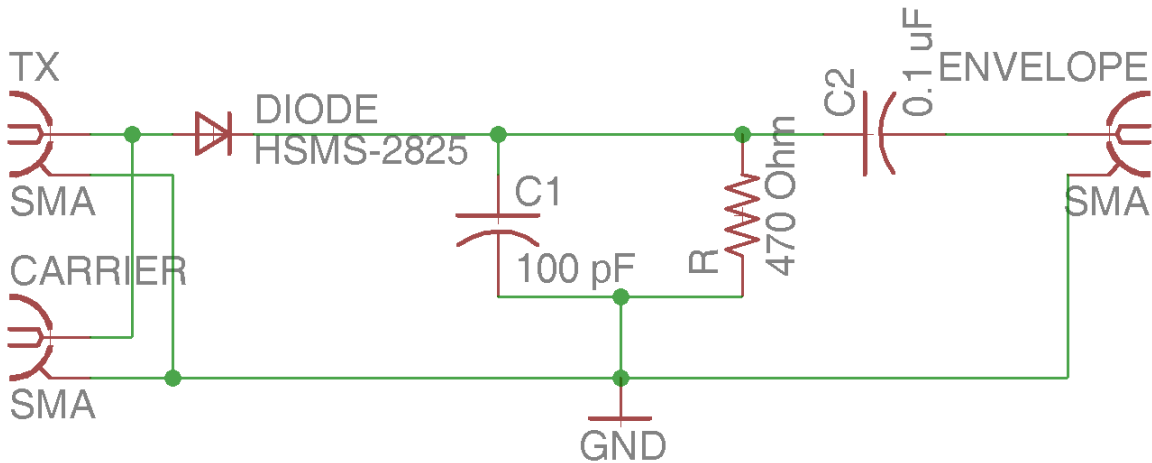


Figure 5.13. Schematic of the power transmitter/data receiver.

5.2.4 Power Receiver/data transmitter

The schematic of the power receiver (which is also the data transmitter) is shown in Figure 5.14. A square wave signal at the DATA port, simulating the data sent by the sensor, oscillates at 5 MHz and it is connected to the gate of a MOSFET, which forms the backscattering modulator. The RX port is connected to the RX element of the broadband planar CSCMR system to a bridge rectifier followed by a $1 \mu\text{F}$ smoothing capacitor. HSMS 2825 Schottky diodes were used in the bridge rectifier for their high frequency response and low drop out voltage. The produced DC power is used to power the sensor

in practical applications. In our proof-of-concept prototype resistors will be used to represent the power drawn by sensor. This enables us to measure exactly the power conversion efficiency for different resistive loads.

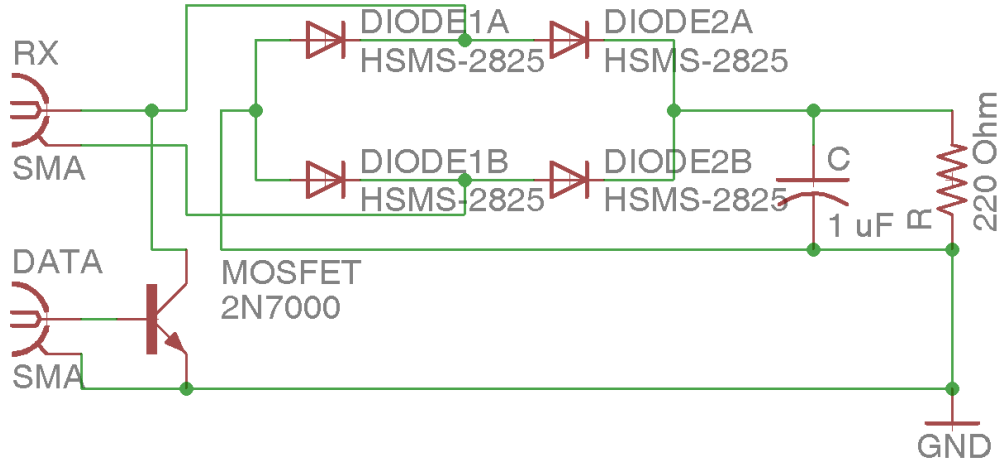


Figure 5.14. Schematic of the power receiver/data transmitter.

5.3 Simulation and Measurement and Results

In this section, simulation and measurement validations of the system will be discussed. ANSYS HFSS was used to simulate the broadband planar CSCMR system and the equivalent two-port network was exported in a file using S-parameter representation. Then, this two-port network was imported into Keysight Advanced Design System (ADS) to simulate the entire system including the power transmitter/data receiver and power receiver/data transmitter. The simulation schematic for the entire circuit is shown in Figure 5.15. In Figure 5.16, the measurement setup of the prototyped system is illustrated.

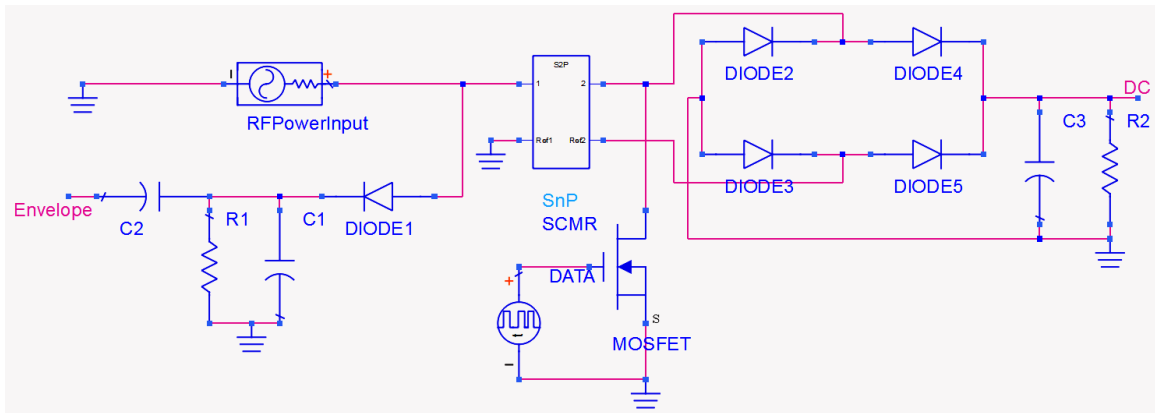


Figure 5.15. Simulation schematic of the system.

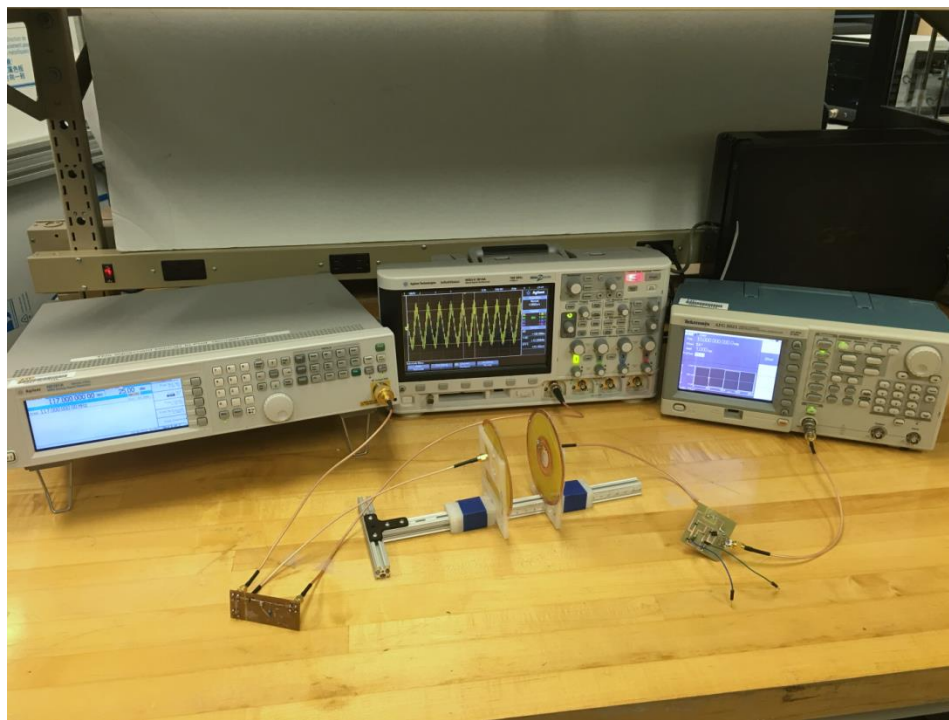


Figure 5.16. Measurement setup.

5.3.1 Comparison between standard and broadband SCMR

Figure 5.17 compares our broadband CSCMR system to a standard CSCMR system. It can be clearly seen that the broadband CSCMR system provides significantly larger bandwidth compared to the standard CSCMR system. Specifically, the 3 dB bandwidth for the broadband and standard CSCMR system is 22.26 MHz and 3.28 MHz,

respectively. Therefore, our broadband CSCMR system exhibits approximately 7 times larger bandwidth than standard CSCMR system, while also maintaining approximately 10% higher power efficiency.

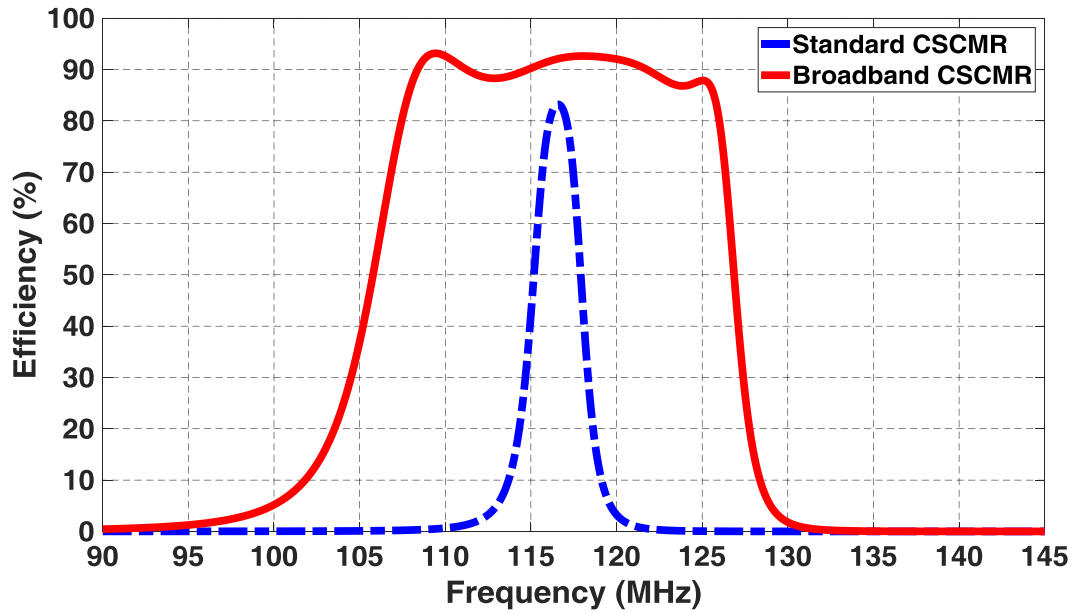


Figure 5.17. Simulated efficiency results for broadband and standard CSCMR systems.

Due to its larger bandwidth, broadband planar CSCMR system can transfer data at a much higher rate. Figure 5.18 compares the data transfer ability standard and broadband CSCMR systems. The data frequency for both systems is 5 MHz. All the other parameters of the two systems are the same. It can be seen that the broadband CSCMR system exhibits received data with clearly discernible bits before and after the demodulator; however, the standard (i.e., narrowband) CSCMR system exhibits received data with no discernible bits.

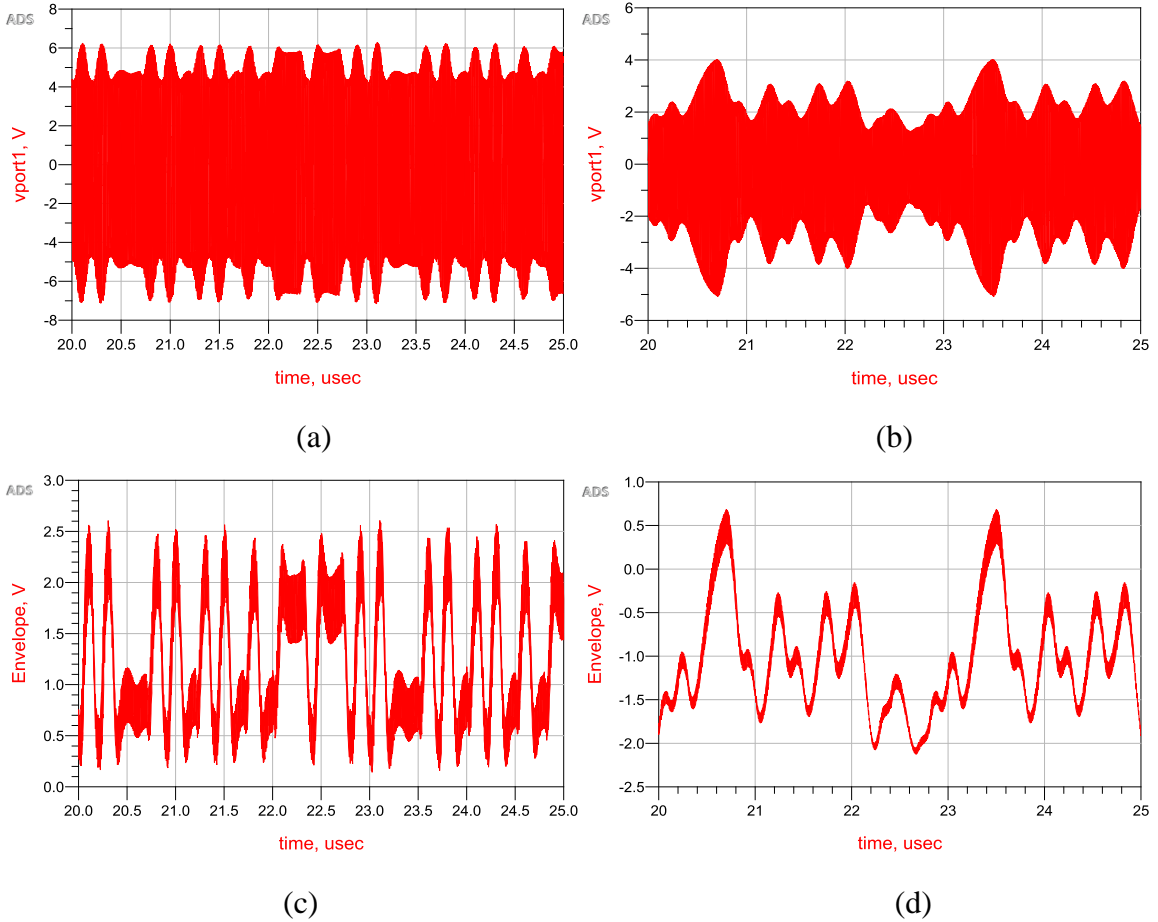


Figure 5.18. Simulated received data before and after envelope detector comparison between: (a) and (c) broadband CSCMR system, and (b) and (d) standard CSCMR systems.

5.3.2 Power efficiency

Our proposed system simultaneously achieves high power transfer efficiency and high data rate communication. High power transfer efficiency is accomplished by our highly efficient CSCMR elements and our bridge rectifier. Figure 5.19 shows the power conversion efficiency as the load resistance varies. The power input is directly connected to the CSCMR transmitter for accurate efficiency calculation. Our signal generator generates 25 dbm power, which is 316 mW, but because of the cable loss, the actual

measured power that reaches our SCMR system is 290 mW. The efficiencies that are shown in Figure 5.19 include both the wireless power transfer loss and rectifier loss. Figure 5.19 shows that the efficiency without the data peaks at approximately 45% for load resistance values between 220 Ω to 830 Ω . Considering that the efficiency of our CSCMR elements is around 80%, the efficiency of our rectifier is approximately 56%. Also, Figure 5.19 illustrates that the power efficiency decreases when the data input is connected. However, when the load resistances are between 220 Ω - 1480 Ω , the efficiencies are still above 30%. Given the fact that data is being transferred through the same link, 30% harvested DC power is satisfactory.

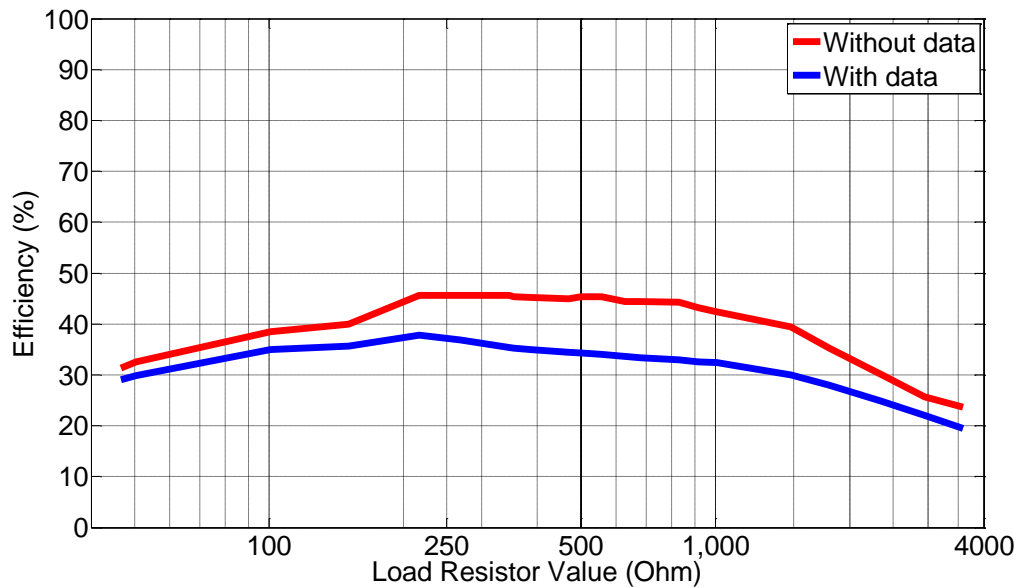


Figure 5.19. Measured RF-to-DC power conversion efficiency.

5.3.3 Data communication

As previously mentioned, for our prototype, a square wave at 5 MHz frequency is used to simulate the data from a sensor. Specifically, the square wave has 1 V peak-to-peak voltage with 500 mV offset, which makes the minimum voltage at 0 V and

maximum voltage at 1 V. The high voltage represents logic 1 and low voltage represents logic 0. When the voltage is high, the MOSFET conducts, the load impedance is small; and when the voltage is low, the MOSFET is off, the load impedance is large. If the modulated signal is visible at the power transmitter, this means that the data transfer is successful.

Figure 5.20 shows the transmitted and received data signal at the power transmitter side. It can be seen that the received data are clearly discernible with different bits and they are in sync with the transmitted data. Furthermore, it reads from the plot that $1/\Delta X = 10 \text{ MHz}$, which is equivalent to 10 Mbps data rate. This plot shows that through backscattering modulation, 10 Mbps data signal can be successfully transmitted while the system is providing DC power to the load efficiently.

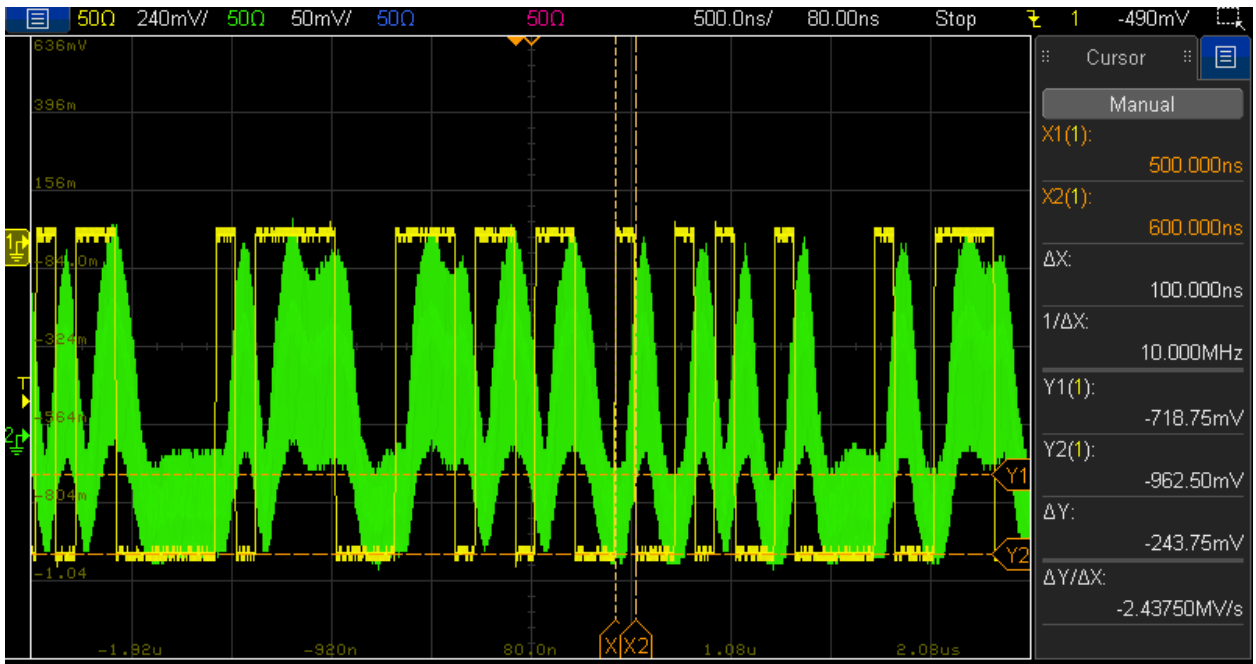


Figure 5.20. Input data (yellow plot) and received data (green plot) comparison.

CHAPTER 6

CONCLUSION AND FUTURE WORK

6.1 Conclusions

This dissertation presented novel structures of strongly coupled magnetic resonant systems for wireless power transfer applications. New misalignment insensitive SCMR systems were developed here for the first time. Also, a broadband planar CSCMR system is used to transfer power and data through the same wireless link using backscattering modulation.

The first misalignment insensitive SCMR system was presented in Chapter 3. This novel 3-D structure utilized two orthogonally connected continuous copper loops for both the source/load elements and resonators. Therefore, both the transmitter and receiver were 3-D structures. By configuring the element parameters according to the design process, this system exhibited misalignment insensitivity throughout 360° of angular misalignment. A disadvantage of this system is the fact that it uses 3-D structures for both the transmitter and receiver, which will not be practical in some cases. Also, such 3D structures occupy large volume.

Another misalignment insensitive SCMR system was presented in Chapter 4. This system used a novel cylindrical design. Furthermore, this system requires only the transmitter or the receiver to have a 3-D structure, while the other one can be a planar structure. This is an important advantage over our first misalignment insensitive system in this second system can use a planar receiver that can be easily incorporated in many

applications such as mobile devices, implantable sensors and embedded sensors for structural health monitoring.

A broadband planar CSCMR system was presented in Chapter 5. This system is integrated with a backscattering modulation system so that it transmits both power and data wirelessly. In fact, 10 Mbps data rate transmission was achieved along with a simultaneous wireless power transfer (with 30% efficiency, which includes the RF-DC loss).

The novel systems presented in this dissertation are expected to enable the development of new technologies for communication and sensing, such as wearable and implantable devices and sensors for structural health monitoring.

6.2 Future Work

The SCMR systems presented here exhibit insensitivity to only azimuth angular misalignment. New geometries can be explored in the future to achieve misalignment insensitive WPT systems for both azimuth and elevation misalignment.

For our SCMR systems that combine power and data transmission, different modulation methods besides backscattering modulation can be studied in the future. Also, in our current systems, the MOSFET is turned on and off; therefore, only two stages of impedance can be transmitted (0 and 1). If an N-stage voltage controlled switch, which connects to N different impedance values, is used in the future, then N-level amplitude modulation can be achieved. With such a switch, even higher data rates can be achieved.

Moreover, frequency modulation instead of amplitude modulation can be explored. Since load modulation changes the impedance of the load, the transmitted

power is being affected by varying the reflection coefficient. If frequency modulation can be implemented, load impedance can always be matched to 50Ω , which will maximize the delivered power.

Finally, the trade-off between range and size of the SCMR systems should be studied and optimized in the future. Miniaturizing the size of SCMR systems leads to lower range. Therefore, new miniaturized systems are needed that can still provide high efficiency and long range.

REFERENCES

- [1] J. Lee and B. Han, "A Bidirectional Wireless Power Transfer EV Charger Using Self-Resonant PWM," *IEEE Trans. Power Electron.*, vol. 30, no.4, pp. 1784-1787, Apr. 2015.
- [2] K. Finkenzeller, *RFID Handbook: Fundamentals and Applications in Contactless Smart Cards and Identification*, 2nd ed. New York:Wiley, 2003, pp. 65-112.
- [3] P. V. Nikitin, K. V. S Rao, and S. Lazar , "An Overview of Near Field UHF RFID," *Proc. RFID IEEE Int. Conf.*, pp. 167 – 174, Mar. 2007.
- [4] D. Ahn and S. Hong, "Wireless Power Transmission With Self-Regulated Output Voltage for Biomedical Implant," *IEEE Trans. Ind. Electron.*, vol. 61, no. 5, pp. 2225-2235, May 2014.
- [5] K. Chang-Gyun, S. Dong-Hyun, Y. Jung-Sik, P. Jong-Hu, and B. H. Cho, "Design of a contactless battery charger for cellular phone," *IEEE Trans. Ind. Electron.*, vol. 48, no. 6, pp. 1238–1247, Dec. 2001.
- [6] A. Kurs, A. Karalis, R. Moffatt, J. Joannopoulos, P. Fisher, and M. Soljagic, "Wireless Power Transfer via Strongly Coupled Magnetic Resonances", *Science*, vol. 317, no. 5834, pp. 83-86, July 2007.
- [7] V. Choudhary, A. Kadir and S. P. Singh, "Wireless power transmission 'a novel idea'". *International Journal of Scientific & Engineering Research*, vol. 2, pp.1-6, Sept. 2011.
- [8] A. Karalis, J.D. Joannopoulos and M. Soljagic, "Efficient wireless non-radiative mid range energy transfer". *Annals of Physics*, vol. 323, pp.34-38, Jan. 2008.
- [9] S. J. Mazlouman, A. Mahanfar and B. Kaminska, "Mid-range wireless energy transfer using inductive resonance for wireless sensors". *ICCD'09 Proceedings of the 2009 IEEE International Conference on Computer design*, pp517-522, 2009.
- [10] J. Agbinya, *Wireless Power Transfer*. River Publishers, Melbourne: 2012.
- [11] D. W. Baarman, "Making Wireless Truly Wireless: The Need for a Universal Wireless Power Solution," *Fulton Innovation*, Paper 2009.
- [12] A. P. Sample, D. T. Meyer and J. R. Smith, "Analysis, Experimental Results, and Range Adaptation of Magnetically Coupled Resonators for Wireless Power Transfer". *IEEE Transactions on Industrial Electronics*, vol. 58, no. 2, pp. 544-554, 2011.
- [13] C. A. Balanis, *Antenna Theory: Analysis and Design*, Wiley, New Jersey, 2005.

- [14] W. C. Brown, "The History of Power Transmission by Radio Waves," *IEEE Transactions on Microwave Theory and Techniques*, vol. 32, no. 9, pp. 1230-1242, Sep. 1984.
- [15] S. Ahson and M. Ilyas, *RFID Handbook: Applications, Technology, Security, and Privacy*. Boca Raton, FL: CRC Press, 2008.
- [16] Y. Jang and M. M. Jovanovic, "A Contactless Electrical Energy Transmission System for Portable-telephone Battery Chargers," *IEEE Trans. Ind. Electron.*, vol. 50, no. 3, pp. 520–527, Jun. 2003.
- [17] J. Shin, S. Shin, Y. Kim, S. Ahn, S. Lee, G. Jung, S. Jeon, and D. Cho, "Design and Implementation of Shaped Magnetic-resonance-based Wireless Power Transfer System for Roadway-powered Moving Electric Vehicles," *IEEE Trans. Ind. Electron.*, vol. 61, no. 3, pp. 1179-1192, Mar. 2014.
- [18] W. X. Zhong, X. Liu, and S. Y. Hui, "A Novel Single-layer Winding Array and Receiver Coil Structure for Contactless Battery Charging Systems with Free-Positioning and Localized Charging Features," *IEEE Trans. Ind. Electron.*, vol. 58, no. 9, pp. 4136–4144, Sep. 2011
- [19] P. E. Glaser, "Power From the Sun: Its Future," *Science Magazine*, vol. 162, no. 3856, pp. 857–861, Nov. 22, 1968.
- [20] P. E. Glaser, United States Patent 3781647, "Method and Apparatus For Converting Solar Radiation To Electrical Power," Dec. 25, 1973.
- [21] W. C. Brown and E. E. Eves, "Beamed Microwave Power Transmission and Its Application to Space," *IEEE Transactions on Microwave Theory and Techniques*, vol. 40, no. 6, pp. 1239-1250, Jun. 1992.
- [22] J. O. McSpadden and J. C. Mankins, "Space Solar Power Programs and Microwave Wireless Power Transmission Technology," in *IEEE Microwave Magazine*, vol. 3, no. 4, pp. 46-57, Dec. 2002.
- [23] J. Benford, "Space Applications of High-Power Microwaves," in *IEEE Transactions on Plasma Science*, vol. 36, no. 3, pp. 569-581, Jun. 2008.
- [24] M. Catrysse, B. Hermans, and R. Puers, "An Inductive Power System with Integrated Bi-directional Data-transmission," *Sensors and Actuators A:Physical*, vol. 115, iss. 2-3, pp. 221–229, Sep. 21, 2004.
- [25] J. C. Schuder, "Powering an Artificial Heart: Birth of the Inductively Coupled-Radio Frequency System in1960," *Artificial Organs*, vol. 26, iss. 11, pp. 909-915, Nov.1, 2002.

- [26] A. Sample and J. R. Smith, "Experimental Results with Two Wireless Power Transfer Systems," *IEEE Radio and Wireless Symposium*, pp. 16-18, San Diego, CA, 2009.
- [27] U. K. Madawala and D. J. Thrimawithana, "A Bidirectional Inductive Power Interface for Electric Vehicles in V2G systems," *IEEE Transactions on Industrial Electronics*, vol. 58, iss. 10, pp. 4789-4796, 2011.
- [28] Z. Wei, W. Siu-Chong, C. K. Tse, C. Qianhong, "Analysis and Comparison of Secondary Series- and Parallel-compensated Inductive Power Transfer Systems Operating for Optimal Efficiency and Load-independent Voltage-transfer Ratio," *IEEE Transactions on Power Electronics*, vol. 29, iss. 6, pp. 2979-90, 2014.
- [29] H. Hu, S. Yao, K. Bao, and S. V. Georgakopoulos, "Misalignment insensitive WPT with conformal SCMR systems," *IEEE Antennas Propagat. Society Internat. Symp.*, Vancouver, BC, Canada, Jul. 19-24, 2015.
- [30] W. Ng, C. Zhang, D. Lin, and S. Y. R. Hui, "Two- and Three-Dimensional Omnidirectional Wireless Power Transfer," *IEEE Trans. Power Electron.*, vol. 29, no.9, pp. 4470-4474, Sep. 2014.
- [31] H. Shibuya, T. Tsukuda, H. Suzuki and T. Shimizu, "A wireless charging and near-field communication combination module for mobile applications," *2014 IEEE 64th Electronic Components and Technology Conference (ECTC)*, Orlando, FL, May 27-30, 2014.
- [32] Y. Sun, P. X. Yan, Z. H. Wang and Y.Y. Luan, "The Parallel Transmission of Power and Data With the Shared Channel for an Inductive Power Transfer System," *IEEE Trans. Power Electron.*, vol. 31, no.8, pp. 5495-5502, 2016.
- [33] S. G. Lee, H. Hoang, Y. H. Choi, and F. Bien, "Efficiency improvement for magnetic resonance based wireless power transfer with axial-misalignment," *Electronics Letters*, vol. 48, no. 6, pp. 339-340, Mar. 15, 2012.
- [34] W. Zhong and S. Y. R. Hui, "Auxiliary circuits for power flow control in multifrequency wireless power transfer systems with multiple receivers," *IEEE Trans. Power Electron.*, vol. 30, no.10, pp. 5902-5910, Oct. 2015.
- [35] D. Ahn and S. Hong, "Effect of coupling between multiple transmitters or multiple receivers on wireless power transfer," *IEEE Trans. Ind. Electron.*, vol. 60, no. 7, pp. 2602-2613, Jul. 2013.
- [36] K. Fotopoulou and B. W. Flynn, "Wireless power transfer in loosely coupled links: coil misalignment model," *IEEE Transactions on Magnetics*, vol. 47, no. 2, pp. 416-430, Feb. 2011.

- [37] O. Jonah, S. V. Georgakopoulos, M. M. Tentzeris, "Orientation insensitive power transfer by magnetic resonance for mobile devices," *IEEE Wireless Power Transfer (WPT)*, pp. 5-8, May 15-16, 2013.
- [38] W. Junhua, S. L Ho, W. N. Fu, and Sun Mingui, "Analytical design study of a novel witrlicity charger with lateral and angular misalignments for efficient wireless energy transmission," *IEEE Transactions on Magnetics*, vol. 47, no. 10, pp. 2616-2619, Oct. 2011.
- [39] F. Zhang, S. A. Hackwoth, X. Liu, L. Chengliu, and S. Mingui, "Wireless power delivery for wearable sensors and implants in body sensor networks," *2010 IEEE Annual International Conference of Engineering in Medicine and Biology Society (EMBC)*, pp. 692-695, Aug. 31-Sep. 4, 2010.
- [40] A. Sample, D. Meyer, and J. Smith, "Analysis, experimental results and range adaptation of magnetically coupled resonators for wireless power transfer," *IEEE Trans. Ind. Electron.*, vol. 58, no. 2, pp. 544–554, Feb. 2011.
- [41] W. Ng, C. Zhang, D. Lin, and S. Y. R. Hui, "Two- and three-dimensional omnidirectional wireless power transfer," *IEEE Trans. Power Electron.*, vol. 29, no.9, pp. 4470-4474, Sep. 2014.
- [42] C. Zhang, D. Lin and S. Y. Hui, "Basic control principles of omnidirectional wireless power transfer," *IEEE Trans. Power Electron.*, vol. 31, no. 7, pp. 5215-5227, Jul. 2016.
- [43] Z. Dang, Y. Cao and J. A. A. Qahouq, "Reconfigurable magnetic resonance-coupled wireless power transfer system," *IEEE Trans. Power Electron.*, vol. 30, no. 11, pp. 6057-6069, Nov. 2015.
- [44] D. Liu, H. Hu and S. V. Georgakopoulos, "Misalignment sensitivity of strongly coupled wireless power transfer systems," *IEEE Trans. Power Electron.*, vol. 32, no. 7, pp. 5509 – 5519, Jul. 2017.
- [45] O. Jonah and S.V. Georgakopoulos, "Wireless power transmission to sensors embedded in concrete via magnetic resonance", *Wireless and Microwave Technology Conference (WAMICON)*, pp.1-6, 18-19 April 2011.
- [46] O. Jonah, S. V. Georgakopoulos, and M. M. Tentzeris, "Optimal design parameters for wireless power transfer by resonance magnetic," *IEEE Antennas and Wireless Propagation Letters*, vol. 11, pp. 1390-1393, 2012.
- [47] D. Daerhan, O. Jonah, H. Hu, S. V. Georgakopoulos and M. M. Tentzeris. "Novel highly-efficient and misalignment insensitive wireless power transfer systems utilizing strongly coupled magnetic resonance principles," *IEEE Electronic Components and Technology Conference (ECTC)*, pp 759-762, May 27-30. 2014.

- [48] H. Hu, S. Yao, K. Bao and S. V. Georgakopoulos, "Misalignment insensitive WPT with conformal SCMR systems," *IEEE International Symposium on Antennas and Propagation (APS)*, pp. 117-118, Jul. 19-24, 2015.
- [49] Z. Yan, Y. Li, C. Zhang and Q. Yang "Influence Factors Analysis and Improvement Method on Efficiency of Wireless Power Transfer Via Coupled Magnetic Resonance," *IEEE Trans. magnetics*, vol. 60, no. 4, Apr. 2014.
- [50] H. Hu and S. V. Georgakopoulos, "Multiband and broadband wireless power transfer systems using the conformal strongly coupled magnetic resonance method," *IEEE Trans. Ind. Electron.*, vol. 64, no. 5, pp. 3595-3607, May 2017.
- [51] C. A. Balanis, *Antenna Theory*, 3rd ed, Wiley 2005.
- [52] <http://www.ansys.com/Products/Electronics/ANSYS-HFSS>.
- [53] <http://resource.ansys.com/Products/Simulation+Technology/Electronics/RF+&+Microwave/ANSYS+DesignerRF/Features/ANSYS+Nexxim+Circuit+Solver+Technology+ANSYS+DesignerRF>.
- [54] David M. Pozar, *Microwave Engineering*, 4th ed. John Wiley & Sons, 2011.
- [55] Awai and T. Ishizaki, "Transferred power and efficiency of a coupled resonator WPT system," in *Proc. IEEE IMWSIWPT*, May 2012, pp. 105–108.
- [56] D. Ahn and S. Hong, "A transmitter or a receiver consisting of two strongly coupled resonators for enhanced resonant coupling in wireless power transfer," *IEEE Trans. Ind. Electron.*, vol. 61, no. 3, pp. 1193–1203, Mar. 2014.
- [57] T. Imura and Y. Hori, "Maximizing Air Gap and Efficiency of Magnetic Resonant Coupling for Wireless Power Transfer using Equivalent Circuit and Neumann Formula," *IEEE Trans. Ind. Electron.*, vol. 58, no. 10, pp. 4746– 4752, Oct. 2011.
- [58] W. Lee, W. Son, K. Oh, and J. Yu, "Contactless Energy Transfer Systems using Antiparallel Resonant Loops," *IEEE Trans. Ind. Electron.*, vol. 60, no. 1, pp. 350–359, Jan. 2013.
- [59] D. Ahn and S. Hong, "A Study on Magnetic Field Repeater in Wireless Power Transfer," *IEEE Trans. Ind. Electron.*, vol. 60, no. 1, pp. 360–371, Jan. 2013.
- [60] W. Zhong, C. K. Lee, and S.Y.R. Hui, "General Analysis on the Use of Tesla's Resonators in Domino Forms for Wireless Power Transfer," *IEEE Trans. Ind. Electron.*, vol. 60, no. 1, pp. 261-270, Jan. 2013.
- [61] R. Johari, J. V. Krogmeier, and D. J. Love, "Analysis and Practical Considerations in Implementing Multiple Transmitters for Wireless Power

- Transfer via Coupled Magnetic Resonance," *IEEE Trans. Ind. Electron.*, vol. 61, no. 4, pp. 1774-1783, Apr. 2014
- [62] J. Kim, A. Banks, Z. Xie, S. Y. Heo, P. Gutruf, J. W. Lee, S. Xu, K.-I. Jang, F. Liu, G. Brown, J. Choi, J. H. Kim, X. Feng, Y. Huang, U. Paik, and J. A. Rogers, "Miniaturized Flexible Electronic Systems with Wireless Power and Near-Field Communication Capabilities," *Advanced Functional Materials*, vol. 25, iss. 30, pp: 4761–4767, Aug. 12, 2015.
- [63] K. Bao, H. Hu, and S. V. Georgakopoulos, "Design Considerations of Conformal SCMR System," *IEEE Wireless Power Transfer Conference 2015*, Boulder, Colorado, May 13-15, 2015.
- [64] H. Hu and S. V. Georgakopoulos, "Wireless Powering based on Strongly Coupled Magnetic Resonance with SRR Elements," *IEEE Antennas Propagat. Society Internat. Symp.*, Chicago, IL, Jul. 8-13, 2012.
- [65] F. E. Terman, *Radio Engineers' Handbook*. New York and London: McGraw-Hill Book Company, 1st edition, 1943.
- [66] O. Jonah, and S.V. Georgakopoulos, "Wireless Power Transmission to Sensors Embedded in Concrete via Magnetic Resonance," *IEEE 12th Annual Wireless and Microwave Technology Conference (WAMICON)*, pp.1-6, 18-19 Apr. 2011.
- [67] J. D. Baena, J. Bonache, F. Martin, R. M. Sillero, F. Falcone, T. Lopetegi, M. A. G. Laso, J. Garcia-Garcia, I. Gil, M. F. Portillo, and M. Sorolla, "Equivalent-circuit Models for Split-ring Resonators and Complementary Split-ring Resonators Coupled to Planar Transmission Lines," *IEEE Trans. Microwave Theory & Tech.*, vol. 53, no4, pp. 1451-1461, Apr. 2005.
- [68] T. Akin, K. Najafi, and R. Bradley, "A Wireless Implantable Multichannel Digital Neural Recording System for a Micromachined Sieve Electrode," *IEEE J. Solid-State Circuits*, vol. 33, pp. 109–118, 1998.
- [69] A. Yakovlev, K. Sanghoek, and A. Poon, "Implantable Biomedical Devices: Wireless Powering and Communication," *Communications Magazine, IEEE*, vol.50, no.4, pp.152,159, Apr. 2012.
- [70] B. Lenaerts and R. Puers, "An Inductive Power Link for a Wireless Endoscope," *Biosens. Bioelectron.*, vol. 22, pp. 1390–1395, 2007.
- [71] S. Gabriel, R. Lau, and C. Gabriel, "The Dielectric Properties of Biological Tissues: III. Parametric Models for the Dielectric Spectrum of Tissues," *Phys. Med. Biol.*, vol. 41, pp. 2271–2293, 1996.
- [72] A. N. Laskovski, T. Dissanayake, and M. R. Yuce, *Wireless Power Technology for Biomedical Implants, Biomedical Engineering*, InTech, 2009.

- [73] R. Bashirullah, "Wireless Implants," in *IEEE Microw. Mag.s*, pp. 14–23, Dec. 2010.
- [74] A. K. RamRakhyani and G. Lazzi, "On the Design of Efficient Multi-Coil Telemetry System for Biomedical Implants," *Biomedical circuits and systems, IEEE Transactions on*, vol. 7, no. 1, pp. 11-23, Feb. 2013.
- [75] M. V. Sarma, V. Iankumaran, and N. S. Rao. "Trends in Cardiac Pacemaker Batteries," *Indian pacing and electrophysiology Journal.*, Oct. 2004.
- [76] A. Yakovlev, K. Sanghoek and A. Poon, "Implantable Biomedical Devices: Wireless Powering and Communication," *IEEE Communications Magazine*, vol.50, no.4, pp.152-159, Apr. 2012.
- [77] H. Kim, J. Park, K. Oh, J. Choi, J. Jang and J. Choi, "Near-Field Magnetic Induction MIMO Communication Using Heterogeneous Multipole Loop Antenna Array for Higher Data Rate Transmission," *IEEE Trans. Antennas Propag.*, vol. 64, no. 5, pp. 1952–1962, May 2016.
- [78] R. Xue, K. Cheng, and M. Je, "High-Efficiency Wireless Power Transfer for Biomedical Implants by Optimal Resonant Load Transformation," *Circuits and Systems I: Regular Papers, IEEE Transactions on* , vol.60, no.4, pp.867,874, Apr. 2013.
- [79] K. Van Schuylenbergh and R. Puers, *Inductive Powering: Basic Theory and Application to Biomedical Systems*. New York: Springer Science.
- [80] Z. Yang, W. Liu, and E. Basham, "Inductor Modeling in Wireless Links for Implantable Electronics," *IEEE Trans. Magn.*, vol. 43, no. 10, pp. 3851–3860, Oct. 2007.
- [81] D. Ahn and S. Hong, "Effect of Coupling between Multiple Transmitters or Multiple Receivers on Wireless Power Transfer," *IEEE Trans. Ind. Electron.*, vol. 60, no. 7, pp. 2602–2613, Jul. 2013.
- [82] M. Kiani and M. Ghovanloo, "The Circuit Theory Behind Coupled-Mode Magnetic Resonance-Based Wireless Power Transmission," *IEEE Trans. Circuits Syst. I, Reg. Papers*, vol. 59, no. 9, pp. 2065-2074, Sept. 2012.
- [83] O. Jonah, S. V. Georgakopoulos, and M. M. Tentzeris, "Strongly Coupled Wireless Power Transfer with Conformal Structures," *29th Annual Review of Progress in Applied Comput. Electromagnetics*, Monterey, CA, Mar. 24-28, 2013
- [84] O. Jonah, S. V. Georgakopoulos, and M. M. Tentzeris, "Optimal Design Parameters for Wireless Power Transfer by Resonance Magnetic," *IEEE Antennas Wireless Propag. Lett.*, vol.11, pp. 1390-1393, 2012.

- [85] S. Ramo, J. R. Whinnery, and T. V. Duzer, *Fields and Waves in Communication Electronics*, 3rd. New York: John Wiley & Sons, 1994.
- [86] F. W. Grover, *Inductance Calculations*. New York: Dover, 1962.
- [87] C. T.-C. Nguyen, "Communications Applications of Micromechanical Systems," *Proceedings, 1998 Sensors Expo*, pp.447-455, San Jose, CA, May 19-21,1998.
- [88] M. A. G. Darrin, B. G. Carkhuff, and T. S. Mehoke, "Future Trends in Miniaturization for Wireless Applications," *Johns Hopkins APL Technical Digest*, vol. 25, no. 4, 2004.

VITA

DAERHAN LIU

- 2011 B. S., Electrical & Information Engineering
University of Science and Technology Beijing
Beijing, China
- 2013 M. S., Electrical Engineering
Florida International University
Miami, Florida
- 2018 Ph. D., Electrical Engineering
Florida International University
Miami, Florida

PUBLICATIONS AND PRESENTATIONS

- [1] D. Liu and S. V. Georgakopoulos, "Cylindrical Misalignment Insensitive Wireless Power Transfer Systems," in *IEEE Transactions on power Electronics*, DOI: 10.1109/TPEL.2018.2791350, 2018.
- [2] D. Liu, H. Hu, and S. V. Georgakopoulos, "Misalignment Sensitivity of Strongly Coupled Wireless Power Transfer Systems," in *IEEE Transactions on Power Electronics*, vol. 32, no. 7, pp. 5509-5519, July 2017.
- [3] D. Liu and S. V. Georgakopoulos, "Cylindrical Topology of SCMR Wireless Power Transfer System," *IEEE Antennas Propagat. Society Internat. Symp.*, San Diego, CA, Jul. 9-14, 2017.
- [4] H. Hu, K. Bao, D. Liu and S. V. Georgakopoulos, "Multi-Device Wireless Charging based on Misalignment Insensitive of Conformal Strongly Coupled Magnetic Resonant System," *IEEE Antennas Propagat. Society Internat. Symp.*, San Diego, California, USA, Jul. 9-14, 2017.
- [5] H. Hu, K. Bao, D. Liu and S. V. Georgakopoulos, "Multi-Device Wireless Charging based on Misalignment Insensitive of Conformal Strongly Coupled Magnetic Resonant System," *IEEE Antennas Propagat. Society Internat. Symp.*, San Diego, California, USA, Jul. 9-14, 2017.
- [6] H. Hu, D. Liu, and S. V. Georgakopoulos, "Miniaturized Strongly Coupled Magnetic Resonant Systems for Wireless Power Transfer," *IEEE Antennas Propagat. Society Internat. Symp.*, Fajardo, Puerto Rico, Jun. 26- Jul. 1, 2016.
- [7] D. Daerhan, H. Hu, and S. V. Georgakopoulos, "Misalignment Study of Two Strongly Coupled Magnetic Resonance Systems," 2015 IEEE 16th Annual IEEE

Wireless and Microwave Technology Conference (WAMICON), Cocoa Beach, FL, April 13-15, 2015.

- [8] O. Jonah, S. V. Georgakopoulos, D. Daerhan, and S. Yao, "Misalignment-Insensitive Wireless Power Transfer Via Strongly Coupled Magnetic Resonance Principles," *IEEE Antennas Propagat. Society Internat. Symp.*, Memphis, TN, Jul. 6-12, 2014.
- [9] D. Daerhan, H. Hu, and S. V. Georgakopoulos, "Novel Topologies of Misalignment Insensitive SCMR Wireless Power Transfer Systems", *IEEE Antennas Propagat. Society Internat. Symp.*, Memphis, TN, Jul. 6-12, 2014.
- [10] D. Daerhan, H. Hu, O. Jonah, S. V. Georgakopoulos, and M. M. Tentzeris, "Novel Highly-Efficient and Misalignment Insensitive Wireless Power Transfer Systems Utilizing Strongly Coupled Magnetic Resonance Principles", *IEEE 64th Electronic Components and Technology Conference (ECTC)*, Orlando, FL, May 27-30, 2014.